UNIVERSITY OF OKLAHOMA

GRADUATE COLLEGE

SEISMIC SOLUTIONS FOR UNCONVENTIONAL RESOURCE PLAYS

A DISSERTATION

SUBMITTED TO THE GRADUATE FACULTY

in partial fulfillment of the requirements for the

Degree of

DOCTOR OF PHILOSOPHY

By

SHIGUANG GUO
Norman, Oklahoma
2014

SEISMIC SOLUTIONS FOR UNCONVENTIONAL RESOURCE PLAYS

A DISSERTATION APPROVED FOR THE
CONOCOPHILLIPS SCHOOL OF GEOLOGY AND GEOPHYSICS

BY

_____
Dr. Kurt Marfurt, Chair

_____
Dr. Roger M. Slatt

_____
Dr. Jamie P. Rich

_____
Dr. Xingru Wu

_____
Dr. Isaac Hall

I would like to dedicate this dissertation to my family and friends whose support, patience, and persistent encouragement was instrumental in allowing me to complete this degree program.

Acknowledgements

First I would like to express my gratitude to my family, my father and mother. It's them brought me to this world and have supported me all the time for my goal. Studying abroad means I can't stay beside them, but they always support me with complete understanding.

Next, I would like to give my sincere thanks to my advisor Dr. Kurt J. Marfurt, for his guidance during my graduate study. It's him that gave me so much encouragement to stretch my potential. His insight of geophysics enabled me to develop innovative problem solving ideas. Moreover, I am inspired by his hard work, optimism and responsibility, which will surely impact my future work and life.

I particularly thank Dr. J. Tim Kwiatkowski's guidance in extending my programming ability. I still remember the last few months I worked with him. He finished the Python library for the students even when he got really sick. I was touched by his hard work and responsibility. I not only learned programming knowledge from him but I learned to be how to become a more responsible person.

I want to extend my gratitude to my committee members Dr. Roger M. Slatt and Dr. Jamie Rich. As a geophysical student, I was not expert in geology and rock physics. It's them that taught me how to integrate geology and rock physics into solutions for unconventional reservoirs. In addition I would like to thank Dr. Xingru Wu, as a Chinese professor, I had many opportunities to talk with him. I learned a lot the engineering of horizontal drilling but also he gave me insight and guidance in my career plan. Finally I want to thank Dr. Isaac Hall. He provided me good suggestions about mathematical

algorithm and seismic processing. I appreciate his comments and suggestions for my graduate research.

I also would like to thank my friends on our AASPI team I appreciate the help from Dr. Kui Zhang, Bo Zhang. Dr. Kui Zhang not only helped me with studies, but also with adapting to life in America along with our fellow student and his wife Yanxia Guo. Whenever I have problems, Bo Zhang is the one who is there and helps me find the solution. I want to thank my good friends Sumit Verma and Alejandro Cabrales, they gave me a lot of support and technical guidance. At last, I want to extend my thanks to Brad, Tengfei, and many others friends, who just make my life here more colorful.

Table of Contents

List of Figures

Abstract

Unconventional reservoir plays an increasingly important role for hydrocarbon exploration. Every reservoir has its unique properties, but it is mostly characterized by low permeability, such that hydraulic fracturing is required to provide pathways for fluid flow. Natural fractures can also provide important permeability. Unfortunately, seismic noise, aliasing, and footprint all contaminate fracture images. My dissertation is divided into four parts, which has been submitted for peer review publication: (1) image of Mississippian Limestone using preconditioned least-squares migration, (2) increasing image quality by developing migration driven 5D interpolation, (3) prediction of natural and induced fractures by correlation between curvature and AVAz vector, (4) evaluation of AVAz anisotropy and curvature in a post hydraulically fracturing Barnett Shale survey.

Conventional Kirchhoff migration often presents artifacts such as aliasing and acquisition footprint noise. I use least-squares migration to minimize the difference between the original data and the modeled demigrated data using an iterative conjugate gradient scheme. I apply this algorithm to image two Mississippian Limestone surveys. I apply the new preconditioned least-squares migration to a survey acquired over a new resource play in the Mid-Continent, USA. Acquisition footprint in shallow targets is attenuated and the signal-to-noise ratio is enhanced. To demonstrate the impact on interpretation, I generate a suite of seismic attributes to image the Mississippian limestone, and show that karst-enhanced fractures in the Mississippian limestone can be better illuminated.

Prestack Kirchhoff time migration is still the most popular migration algorithm due to its high efficiency and flexibility. Unfortunately suboptimal surface seismic acquisition

often gives rise to both data and migration operator aliasing, both of which hinder subsequent interpretation. Current 5D interpolation techniques are applied in the surface data domain, typically on NMO-corrected CMP gathers. Such corrections properly flatten specular reflections for subsequent lateral interpolation but will not flatten unfocussed diffractions whose moveout is non-hyperblic on CMP gathers. I believe this shortcoming leads to the decrease in lateral resolution on (now largely artifact free) 5D interpolated seismic volumes. I have implemented an alternative migration driven 5D interpolation as my interpolation operator. I show that this approach will interpolate not only specular but nonspecular events.

The Barnett Shale is a major hydrocarbon resource play in the Fort Worth basin, it has been produced by drilling and completing horizontal wells perpendicular to the direction of maximum stress. I migrate the surface seismic data into a suite of azimuthal and offset bins, then calculate the AVO gradient from azimuthally-limited prestack gathers for each azimuth bin. By comparing the azimuthal AVO gradient variation, I generate an AVAz volume that can then be used to predict the orientation of horizontal stress. While natural fractures in the Barnett shale are almost all cemented, in other basins AVAz can be used to predict the orientation and intensity of natural fractures. Strike-slip faults are known to modify the subsurface stress regime. I map faults using both the strike and magnitude of the most-positive and most-negative principal curvatures and visually correlate them to AVAz. To be quantitative, I generate a vector correlation between AVAz and the two curvatures and find correlation between the "stress field" and the strike and intensity of structural deformation. By comparing two adjacent Barnett Shale seismic surveys—the first acquired before hydraulic fracturing and the second acquired after

hydraulic fracturing find that in the survey acquired prior to hydraulic fracturing that AVAz anomalies are both stronger and highly correlated to major structural lineaments measured by curvature. In contrast, AVAz anomalies in the acquired after hydraulic fracturing are weaker and compartmentalized by rather than correlated to most-positive curvature lineaments.

Chapter 1: Introduction

Unconventional plays has become most popular in North America over the past decade, as development of hydraulic fractures can provide pathway for fluid flow and increase the permeability. It can also assist in the release of gas adsorbed on mineral and organic matter in the shale. Unfortunately, seismic imaging of unconventional reservoir has been suffered from noise, aliasing, and footprint, which can hinder subsequent interpretation, prediction of natural fractures, and anisotropy analysis, etc. To address these artifacts, I develop preconditioned least-squares migration and migration driven 5D interpolation methods for seismic precondition, which consists the first two topics for my dissertation. In addition, imaging fractures, faults, and diagenetic alteration in unconventional reservoirs are extremely important. Prediction of natural fractures and evaluation of post-hydraulic fracturing are essential for horizontal well placement and further reservoir exploration, I develop vector correlation between AVAz and curvature to predict natural fractures on a survey prior hydraulic fracturing and evaluate induced fracturing caused anisotropy analysis on a survey after hydraulic fracturing performed.

This dissertation combines 3 published SEG expanded abstracts, one paper is submitted GEOPHYSICS journal, two papers to be submitted to GEOPHYSICS journal and one paper to be submitted to Interpretation. In addition, I have co-authored one paper already published in Geophysical Prospecting journal and one paper published in GEOPHYSICS journal. I have developed Preconditioned Least-squares Migration, 5D Interpolation, and Vector Correlation etc. algorithms of OU's Attribute-Assisted Seismic

Processing and Interpretation (AASPI) research team, and I am in charge of prestack software utility maintenance in AASPI.

In Chapter 2, I introduce Preconditioned Least-squares Migration (PLSM) and I apply PLSM to a Mississippian Limestone survey for imaging of karst features. I investigate how PLSM suppresses noise and improves seismic attribute illumination for karst interpretation.

In Chapter 3, I develop 5D interpolation through PLSM and apply this method to two Mississippian Limestone surveys, one from Kansas and another one from north Texas. The second survey is suffered by groundroll noise, I evaluate how 5D interpolation through PLSM can help to suppress footprint noise, increase resolution, balance seismic amplitude and improve seismic interpretation.

In Chapter 4, I predict natural fractures by correlation between curvature and AVAz vector on Barnett Shale in the Fort Worth basin, and study the relationship between fracturing caused anisotropy and normalized EUR.

In Chapter 5, I evaluate the anisotropy of Barnett Shale formation after hydraulic fracturing using the vector correlation between AVAz and curvature, then evaluate the hydraulic fracturing caused anisotropy by comparing two adjacent Barnett Shale seismic surveys—the first acquired before hydraulic fracturing and the second acquired after hydraulic fracturing by over 400 wells.

Chapter 2: Preconditioned Least-Squares Migration-Application to the Mississippian Limestone

Shiguang Guo[1], Bo Zhang[1], Alejandro Cabrales-Vargas[2], and Kurt J. Marfurt[1],

[1]The University of Oklahoma, ConocoPhillips School of Geology and Geophysics,

[2]Pemex Exploración Producción,

ABSTRACT

Conventional Kirchhoff migration often suffers from artifacts such as aliasing and acquisition footprint, which come from sub-optimal seismic acquisition. The footprint can mask faults and fractures, while aliased noise can focus as false coherent events which affect interpretation and contaminate AVO, AVAz and elastic inversion. Preconditioned least-squares migration minimizes these artifacts.

We implement least-squares migration by minimizing the difference between the original data and the modeled demigrated data using an iterative conjugate gradient scheme. Unpreconditioned least-squares migration better estimates the subsurface amplitude, but does not suppress aliasing. In this work, we precondition the results by applying a 3D prestack structure-oriented LUM filter to each common offset and common azimuth gather at each iteration. The preconditioning algorithm suppresses aliasing of both signal and noise, and improves the convergence rate.

INTRODUCTION

Prestack Kirchhoff time migration is still the most popular migration algorithm due to its high efficiency and flexibility, especially in imaging relatively flat-lying faulted and fractured plays in the Mid-Continent of the USA. Unfortunately, suboptimal surface seismic acquisition patterns usually give rise to both data and migration operator aliasing and footprint, both of which hinder subsequent interpretation. The most common means of suppressing aliasing is to apply an antialias filter within the migration algorithm (Figure 2.1). While such a filter removes the aliasing overprint, it also reduces the high-frequency content of more steeply dipping events, including lateral discontinuities. One of the goals of PLSM is to suppress aliasing yet retain the full frequency bandwidth in the resulting image.

Conventional Kirchhoff migration can be regarded as the adjoint of the seismic forward modeling operator (Claerbout, 1992). Chavent and Plessix (1996) used standard migration as the zeroth iteration, and then used a conjugate gradient scheme to compute the Hessian matrix. They then used a least-squares formulation to obtain an optimized image. Schuster (1993) added constraints to the objective function. Following Nemeth (1996), he used least-squares migration to overcome uncompensated migration artifacts due to incomplete data, which can give rise to acquisition footprint.

Least-squares migration may require many iterations to reach convergence, consuming significant computer resources. For this reason, significant effort has focused on preconditioning the input data to decrease the number of iterations. Wei and Schuster (2009) and Aoki and Schuster (2009) preconditioned the data by using a deblurring filter, thereby reducing the number of iterations needed. Wang and Sacchi (2009) evaluated

running average and prediction filter constraints to improve the convergence rate of a 2D least-squares migration algorithm. Cabrales Vargas (2011) used mean and median filters as constraints in 3D constrained least-squares migration in his master's thesis.

Post-stack structure-oriented filtering is commonly used in conditioning stacked volumes after migration to facilitate interpretation (Fehmers and Höcker, 2003). Luo et al. (2002) extended the Kuwahara et al. (1976) algorithm to 3D seismic data as an alternative edge-preserving smoothing algorithm. Marfurt (2006) proposed a modification of Luo et al.'s (2002) technique. First, he used coherence rather than the standard deviation to choose the most homogeneous window. Then, instead of using the mean, median or the α-trimmed mean, he used a principal component (or Karhunen-Loeve) filter that more fully uses trends in the analysis window to replace the amplitude at the analysis point. Corrao et al. (2011) showed how an LUM-based structure-oriented filter can reject outliers, yet better retain the original character of the seismic data. Kwiatkowski and Marfurt (2011) showed how such filters can be applied to prestack time-migrated common-offset-azimuth gathers. To suppress aliasing within the conjugate gradient PLSM algorithm, I apply structure-oriented filters to the common-offset-azimuth gathers, which reduces the number of iterations needed by PLSM.

In this paper, we begin my discussion by a review of Kirchhoff migration and demigration. Specifically, we examine the role of Kirchhoff migration as the adjoint of the seismic modeling operator and demigration as the seismic modeling operator in a PLSM algorithm. Next, we will introduce the mathematics of the PLSM algorithm, and its solution using the conjugate gradient method. Then, we show how Kwiatkowski and Marfurt's (2011) prestack structure-oriented filter serves as precondition term that

increases PLSM convergence. We demonstrate the value of my PLSM algorithm and workflow to two prestack Mississippian Lime data volume from Ness Co., KS and Osage Co., OK and illustrate the effectiveness by analyzing seismic attributes computed along the Gilmore City and Mississippian Chert horizons. We conclude with a summary of computational advantages and disadvantages of PLSM.

METHODOLOGY

The preconditioned conjugate gradient method

The conjugate gradient method is perhaps the most popular iterative algorithm for solving sparse systems of linear equations. Preconditioning is an important technique used to develop an efficient conjugate gradient method solver for challenging problems in scientific computing, the larger the condition number of a SPD (positive-definite matrix), the slower the conjugate gradient method will converge (Caraba, 2008), the idea behind of preconditioning is using the CG on an equivalent system, it's like

First, we initialize the model $\mathbf{m}$ to be 0:

$$\mathbf{m_0} = 0, \tag{2-1}$$

Next, we compute the residual vector $\mathbf{r_0}$ associated with the model $\mathbf{m_0}$:

$$\mathbf{r_0} = \mathbf{d_0} - \mathbf{L}\mathbf{m_0}, \tag{2-2}$$

where $\mathbf{d_0}$ represent the original data. Since $\mathbf{m}_0 = 0$, we obtain:

$$\mathbf{r_0} = \mathbf{d_0}, \tag{2-3}$$

The residual vector $\mathbf{r_0}$ constitutes the initial search direction, allowing me to compute the zeroth iteration gradient vector:

$$\mathbf{g_0} = \mathbf{L^T}\mathbf{r_0}, \tag{2-4}$$

where $\mathbf{g_0}$ can be regarded as the conventional (unconstrained, non-least-squares) migration result, and defines the search direction of the first $n = 1$ iteration in the conjugate gradient scheme. Following Jovanovic (2004), I create a set of orthogonal conjugate direction vectors $\mathbf{h_n}$,

$$\mathbf{h_n} = \mathbf{g_n} + \sum_{k=0}^{n-1} \beta_k \mathbf{h_k}, \tag{2-5}$$

where β_k is the k^{th} weighting coefficient. For the $n = 0$ iteration, $\mathbf{h_0}$ is identical to $\mathbf{g_0}$, resulting in an updated model vector $\mathbf{m_{n+1}}$:

$$\mathbf{m_{n+1}} = \mathbf{m_n} + \alpha_n \mathbf{h_n}, \tag{2-6}$$

Where α_n is the weighting coefficient at the n^{th} iteration. Next, we update the residual (direction) vector $\mathbf{r_{n+1}}$ and gradient $\mathbf{g_{n+1}}$:

$$\mathbf{r_{n+1}} = \mathbf{r_n} - \alpha_n \mathbf{L h_n}, \text{ and} \tag{2-7}$$

$$\mathbf{g_{n+1}} = \mathbf{L^T r_{n+1}}. \tag{2-8}$$

Since $\mathbf{L^T}$ denotes migration, the gradient vector $\mathbf{g_{n+1}}$ is the migration of the residual $\mathbf{r_{n+1}}$.

We define the optimum values of the weighting coefficients α_n and β_n to be:

$$\alpha_n = \frac{\langle \mathbf{g_n}, \mathbf{g_n} \rangle}{\langle \mathbf{L h_n}, \mathbf{L h_n} \rangle}, \text{ and} \tag{2-9}$$

$$\beta_n = \frac{\langle \mathbf{g_{n+1}}, \mathbf{g_{n+1}} \rangle}{\langle \mathbf{g_n}, \mathbf{g_n} \rangle}, \tag{2-10}$$

where the notation <,> indicates the inner product. To enhance the specular reflection energy and attenuate the aliased noise, we will apply a structural-oriented filter $\mathbf{F}$ as precondition term along reflection dip to $\mathbf{m}$:

$$\widetilde{\boldsymbol{m}}_{\mathbf{n+1}} = \mathbf{F}(\mathbf{m}_{\mathbf{n+1}}), \tag{2-11}$$

prior to updating $\mathbf{h}$

$$\tilde{\mathbf{h}}_{\mathbf{n}} = \frac{\widetilde{\boldsymbol{m}}_{\mathbf{n+1}} - \mathbf{m}_{\mathbf{n}}}{\boldsymbol{\alpha}_{\mathbf{n}}}. \tag{2-12}$$

Where $\widetilde{\boldsymbol{m}}_{\mathbf{n+1}}$ is the filtered model, $\mathbf{m}_{\mathbf{n}}$ is the predicted model for previous iteration. This equation can improve the searching direction by addition preconditioned term.

Substituting the updated $\tilde{\mathbf{h}}_{\mathbf{n}}$ for $\mathbf{h}_{\mathbf{n}}$ in equation 2-12 results in preconditioned least-squares migration, the whole workflow is shown from Figure 2.2. To obtain an accurate representation of the Earth's reflectivity model, the conjugate gradient scheme needs to run a number of times, with the number of iterations depending on the convergence rate and the desired level of accuracy. In our applications, we will limit myself to no more than three iterations, which will provide the bulk of the image improvement. Thus this algorithm will run approximately six times longer than the corresponding conventional migration algorithm.

Structure-oriented filtering

Structure-oriented filtering utilizes filters along local estimates of seismic dip and azimuth. To remove random noise and enhance lateral continuity, popular filters include mean, median, α-trim mean, LUM, and principle component filters. Given the need to suppress strong, non-Gaussian aliased noise in least-squares migration, I will use the LUM filter to each common-offset gathers.

Figures 2.3a and b illustrate the steps for pre-stack structure-oriented filtering along local structure using a centered analysis window. We sort the prestack gathers into different common offset volume and smoothing the data along local structure. In this example there are 3 crosslines by 3 inlines and 3 offsets resulting in a length 27 "sample vector" $\mathbf{s}_i$ $(i = 1, 2, \ldots, 27)$ for each interpolated horizon slice at time index *k*. These sample vectors are cross-correlated and averaged from *k*=-*K to k*=+*K* (*K*=2) time samples using equation 1 resulting in a 27 by 27 covariance matrix. Similarly we only preserve the value of analysis point (the blue point in Figure 2.3b) after the "eigenmap". Figure 2.4 summarizes the proposed workflow of prestack oriented filtering by considering the geology discontinuities. The workflow begins by stacking the original seismic gathers. We next estimate the reflectors orientation in a running window on all traces of the stacked volume (Marfurt, 2006). We then calculate the correlation coefficients for the stack volume along the local reflection dip and azimuth (Gersztenkorn and Marfurt, 1999). To archive the edge preserving filtering, we only perform PCA filtering to those gathers whose correlation coefficients are greater than a user defined threshold through the first eigenvalue and eigenvector of seismic covariance matrix. The gathers whose correlation coefficients are less than the threshold are not undergoing any processing. In this manner we improve the SNR and avoid smearing amplitude information across the geology discontinuities such as faults and channels.

The α-trim mean filter

The first step in the α-trim mean filter is to first sort a suite of seismic samples in ascending order. Then, the lowest and highest α fraction of the data are trimmed away, or rejected. Finally, I compute the mean of the remaining 1-2α fraction of the data. Thus, a

value of α =0.0 results in the conventional median filter. Ideally, rejection of α fraction of the largest and smallest data will reject strong positive and negative spikes, while the mean filter improves the statistics of the "better behaved" data that remain.

The lower-upper-middle (LUM) filter

The lower-upper-middle (LUM) filter is a nonlinear filter that is simple to define and yet effective for noise attenuation in non-stationary signal processing (Boncelet et al. 1991). It has two parameters, one for smoothing and the other for sharpening.

The smoothing pattern of the LUM filter are controlled by one of two filter parameters. The level of smoothing is controlled by varying the parameter. Having such control allows one to best balance the tradeoffs between noise smoothing and signal-detail preservation.

LUM filters can also be designed to enhance edge gradients. The amount of enhancement done by the LUM filter is controlled by the second filter parameter. Edge enhancement and sharpening have traditionally been accomplished using linear techniques.

APPLICATION

Dickman field, located in Northern County, Kansas (Figure 2.5), is a typical super mature Mississippian reservoir, and has produced approximately 1.7 million barrels of oil. In the field, Pennsylvanian strata unconformably overlie the Mississippian reservoir rocks of the Meramecian Spergen and Warsaw limestone. The Mississippian reservoir in Dickman field is composed of shallow-shelf carbonates. Karst-enhanced fractures have been documented to extend several meters below the regional unconformity surface. The Western Interior Plains aquifer system acts as a very strong bottom water drive for the reservoir, which in turn is underlain by the low porosity and low permeability Gilmore City limestone, which acts as a flow barrier. Figure 2.6 shows a time structure map of the Gilmore City limestone. Red arrows denote karst features.

Figure 2.7a shows vertical slices through the conventionally migrated seismic amplitude volume along profiles AA' (Figure 2.6) of conventional migration, the low signal-to-noise ratio causes poor resolution of the reflectors,while random noise masks subtle geological features. After two and three iterations of PLSM in Figures 2.7b and c, the signal-to-noise ratio is enhanced and there is a reduction in noise compared to conventional migration.

Figure 2.8a shows a time slice at t=0.87 s as the Mississippian Limestone level through the stacked volume after conventional migration. The red block arrow indicates footprint, which interferes with interpretation of subtle geological features. After two and three iterations of PLSM in Figure 2.8b and Figure 2.8c, the footprint is almost eliminated while the structural features are retained.

Figure 2.9a shows coherence horizon slices through coherence volumes along the Gilmore City after conventional migration. The red block arrow denotes the contamination of random noise on the coherence attribute. After two iterations of PLSM in Figure 2.9b, contaminating noise is suppressed. After three iterations of PLSM in Figure 2.9c, most random noise is gone. The red block arrows highlight the karst features in form of collapse character.

Figure 2.10a shows co-rendered horizon slices along the Gilmore city through the inline coherent energy gradient (the derivative of the energy along local dip and azimuth) co-rendered with coherent energy volumes after conventional migration. While this image highlights the karst collapse features, the presence of footprint and other noise contaminates the image. Figures 2.10b and c show the same two attributes after two and three iterations of PLSM. The resulting co-rendered attribute illumination of the karst collapse features is significantly improved.

Figure 2.11a shows representative demigrated traces from the middle of the survey, and Figure 2.11b shows demigrated modeled traces after 3 iterations of PLSM. PLSM better approximates the coherent reflection data, random noise in the demigrated image is attenuated. The demigrated reflectors become increasingly coherent with the number of iterations in PLSM.

CONCLUSIONS

PLSM worked effectively for removing aliasing artifacts arise from decimated Dickman survey from west Kansas. By comparing with the residual convergence rate of LSM, the structure-oriented median filter served as constraint in PLSM.

Application of PLSM to the undecimated Dickman dataset from west Kansas showed rapid improvement of signal-to-noise ratio for CRP gathers and significant attenuation of footprint and random noise, which impeded interpretation from conventional migration. Moreover, PLSM brought significant improvement for seismic attributes illumination. PLSM made multiple attributes better illuminate karst collapse features on Gilmore City horizon. In addition, PLSM worked well for eliminating the random noise in prestack gathers, and the outcome of constrained least-squares migration better represents the seismic amplitudes of earth reflectivity. At last, PLSM allowed better prediction of the original gathers while enhance coherent events.

Appendix A: Least-squares migration

Kirchhoff migration

Kirchhoff migration is the adjoint operator of Kirchhoff modeling (Nemeth et al., 1999). Biondi (2006) represents prestack 3D Kirchhoff migration using Green's function

$$\mathbf{m}(\xi) = \int_{\Omega_\xi} W(\xi, \mathbf{q}, \mathbf{h}) \frac{\partial}{\mathrm{d}t} d[t = t_D(\xi, \mathbf{q}, \mathbf{o}), \mathbf{q}, \mathbf{o}] \mathrm{d}\mathbf{q}\mathrm{d}\mathbf{o}, \tag{A-1}$$

where $\mathbf{m}(\xi)$ are the migrated CRP gathers,

$\mathbf{d}(t, \mathbf{q}, \mathbf{o})$ are the surface seismic data,

$\mathbf{W}(\xi, \mathbf{q}, \mathbf{o})$ is the weighing function,

$\frac{\partial}{dt}$ represents the first time derivative,

Ω_ξ is the migration aperture,

q is the midpoint vector, and

o is the offset position vector.

Equation 2-1 migrates $d(t, \mathbf{q}, \mathbf{o})$ when the midpoint, $\mathbf{q}$, falls in the migration aperture Ω_ξ. $t_D(\xi, \mathbf{q}, \mathbf{o})$ is the time that the reflection travels from the source position to image position,t_s, plus the time from the image point back to the receiver, t_g:

$$t_D = t_s + t_g = \sqrt{\frac{Z_\xi^2 + |\mathbf{XY}_\xi - \mathbf{q} + \mathbf{o}|^2}{V}} + \sqrt{\frac{Z_\xi^2 + |\mathbf{XY}_\xi - \mathbf{q} - \mathbf{o}|^2}{V}}. \tag{A-2}$$

where $\mathbf{XY}_\xi$ represents the horizontal projection of the image-coordinate vector, and *v* is the migration velocity.

Perez and Marfurt (2008) proposed a new azimuthal binning approach to Kirchhoff prestack migration that sorts the output by the azimuth of the average travel path from surface midpoint to subsurface image point, rather than the azimuth between source and

receiver (Figure 2.1). This new binning allows us to identify the image contribution from out-of-the-plane steeply dipping reflectors, fractures, and faults. I will use this algorithm as my migration operator. For 'conventional migration', I will leave the antialias operator 'on'. For PLSM, I will remove the antialias operator and instead use the constraints to reduce aliasing after the first iteration.

Kirchhoff demigration

Demigration is the adjoint of migration, and constitutes the modeling operator during least-squares migration (Zhang, et al, 2002; Biondi, 2006)

$$\mathbf{D}(t,\mathbf{q},\mathbf{o}) = \int_Q W(\xi,\mathbf{q},\mathbf{o})\frac{\partial}{\mathrm{d}t}\mathbf{m}(t_\xi,\mathbf{x}_\xi,\mathbf{y}_\xi)\mathrm{d}\mathbf{x}\mathrm{d}\mathbf{y}, \tag{A-3}$$

where

$\mathbf{D}(\mathbf{t},\mathbf{q},\mathbf{o})$ denotes the 3D modeled common-shot gathers,

$\mathbf{m}(x_\xi, y_\xi, z_\xi)$ are the 3D migrated common-reflection point gathers in time domain,

$(\mathrm{x}_\xi, \mathrm{y}_\xi)$ represents the horizontal projection of the image point,

$\mathbf{W}(\xi,\mathbf{q},\mathbf{o})$ are the demigration weights,

$\frac{\partial}{dt}$ is the time derivative applied to the migrated common-reflection point gathers, and

Q denotes the demigration aperture.

t_ξ is the total time the reflection travels from the source position to image position, plus the time from the image point back to the receiver:

$$t_\xi = t_s + t_g = \sqrt{\frac{Z_\xi^2+|\mathbf{XY}_\xi-\mathbf{q}+\mathbf{o}|^2}{V}}+\sqrt{\frac{Z_\xi^2+|\mathbf{XY}_\xi-\mathbf{q}-\mathbf{o}|^2}{V}}. \tag{A-4}$$

The demigration program we developed in this work is based on the Kirchhoff

prestack time migration, and it constitutes the forward modeling operator used in the least-squares migration workflow described below.

Least-squares migration

We can express modeling (demigration) in matrix notation as:

$$\mathbf{d} = \mathbf{L}\mathbf{m}, \tag{A-5}$$

where **L** constitutes the forward modeling operator (in this paper prestack time demigration),

m is the reflectivity model, and

d is the modeled data.

We define migration as

$$\mathbf{m}' = \mathbf{L}^{\mathrm{T}}\mathbf{d}, \tag{A-6}$$

where

$\mathbf{L}^{\mathrm{T}}$ is the adjoint operator of **L**, (in this work prestack time migration), and

$\mathbf{m}'$ is the migration approximation to the Earth's reflectivity.

Standard migration $\mathbf{L}^{\mathrm{T}}$ is the adjoint of the forward modeling operator **L**.

Substituting equation A-5 into equation A-6, I obtain

$$\mathbf{m}' = \mathbf{L}^{\mathrm{T}}\mathbf{L}\mathbf{m}. \tag{A-7}$$

We can regard the matrix $\mathbf{L}^{\mathbf{T}}\mathbf{L}$ as a linear filter applied to **m**. If $\mathbf{L}^{\mathbf{T}}\mathbf{L}$ approximates the identity matrix, the migration $\mathbf{m}'$ will be a scaled version of the reflectivity **m**.

Unfortunately, due to sparse surface acquisition, $\mathbf{L^T L}$ is almost never diagonal such that $\mathbf{m}'$ exhibits migration artifacts (Nemeth, 1996).

Schuster (1997) attenuated these artifacts by making $\mathbf{L^T L}$ closer to the identity matrix. In this paper, I add precondition term to obtain:

$$\varepsilon = \left|\left|\mathbf{Lm} - \mathbf{d}\right|\right|^2 + ||\mathbf{Pm}||^2, \tag{A-8}$$

where ε is the objective function to be minimized, the first term on the right-hand side of the equation is the misfit function, and **P** is the precondition matrix. Multiplying both sides of equation A-8 by $\mathbf{L^T}$, we form the normal equations and minimize the function:

$$[\mathbf{L^T L} + \boldsymbol{P^T}\mathbf{P}]\mathbf{m} = \mathbf{m}' = \mathbf{L^T d}. \tag{A-9}$$

We will solve equation A-9 for **m** using a conjugate gradient scheme, giving rise to an iterative method constitutes preconditioned least-squares migration algorithm.

ACKONWLEDGEMENTS

Thanks to Schlumberger for their software, I also would like to thank sponsors of Attribute-Assisted Seismic Processing and Interpretation Consortium (AASPI) for their guidance and financial support.

LIST OF FIGURES

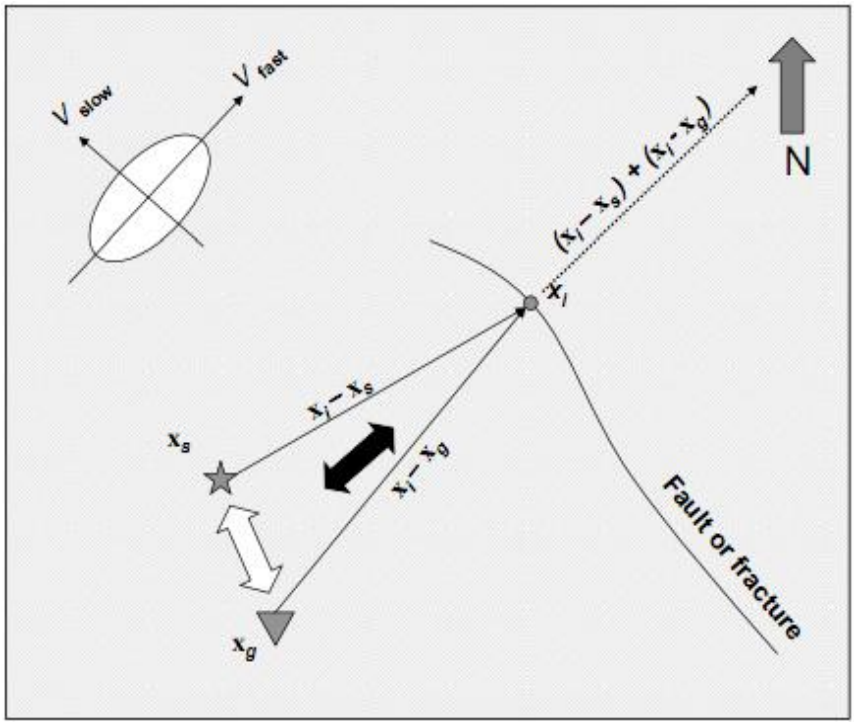

Figure 2.1. New azimuthal binning (After Perez and Marfurt, 2008).

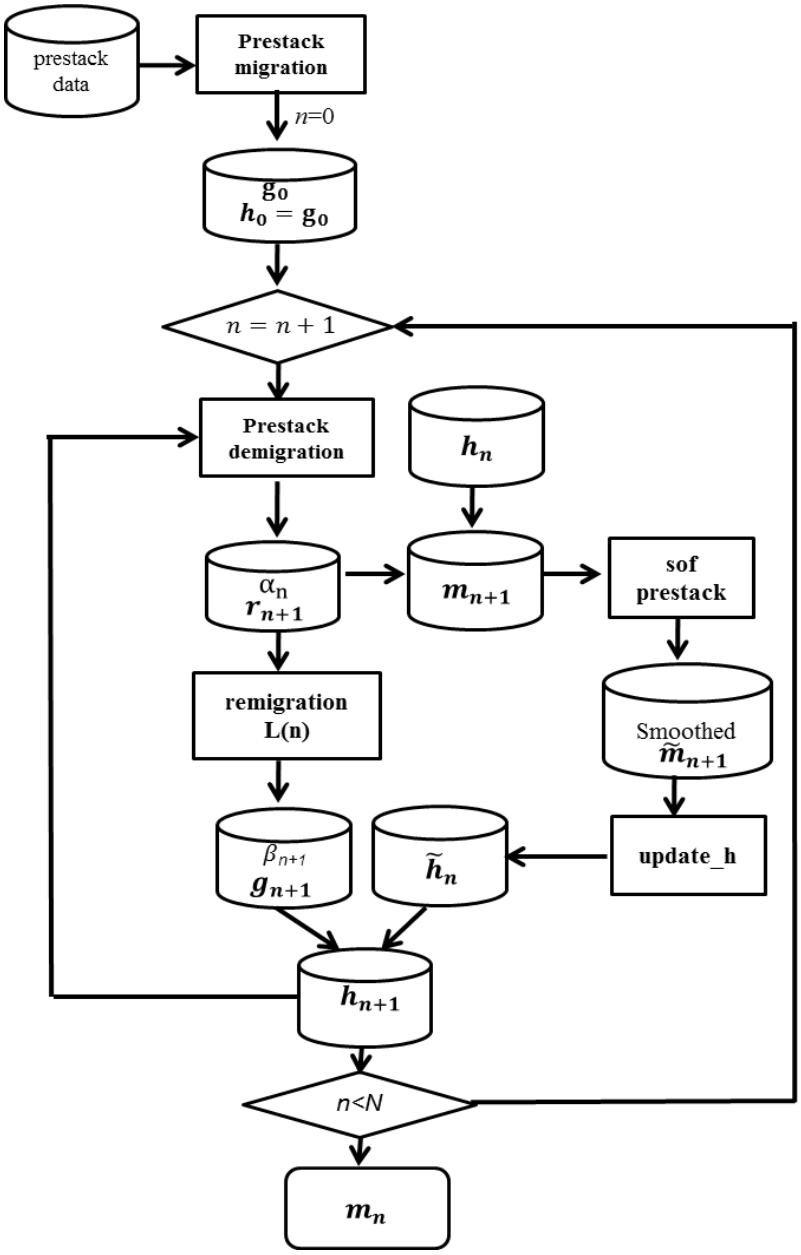

Figure 2.2. Workflow of Preconditioned least-squares migration.

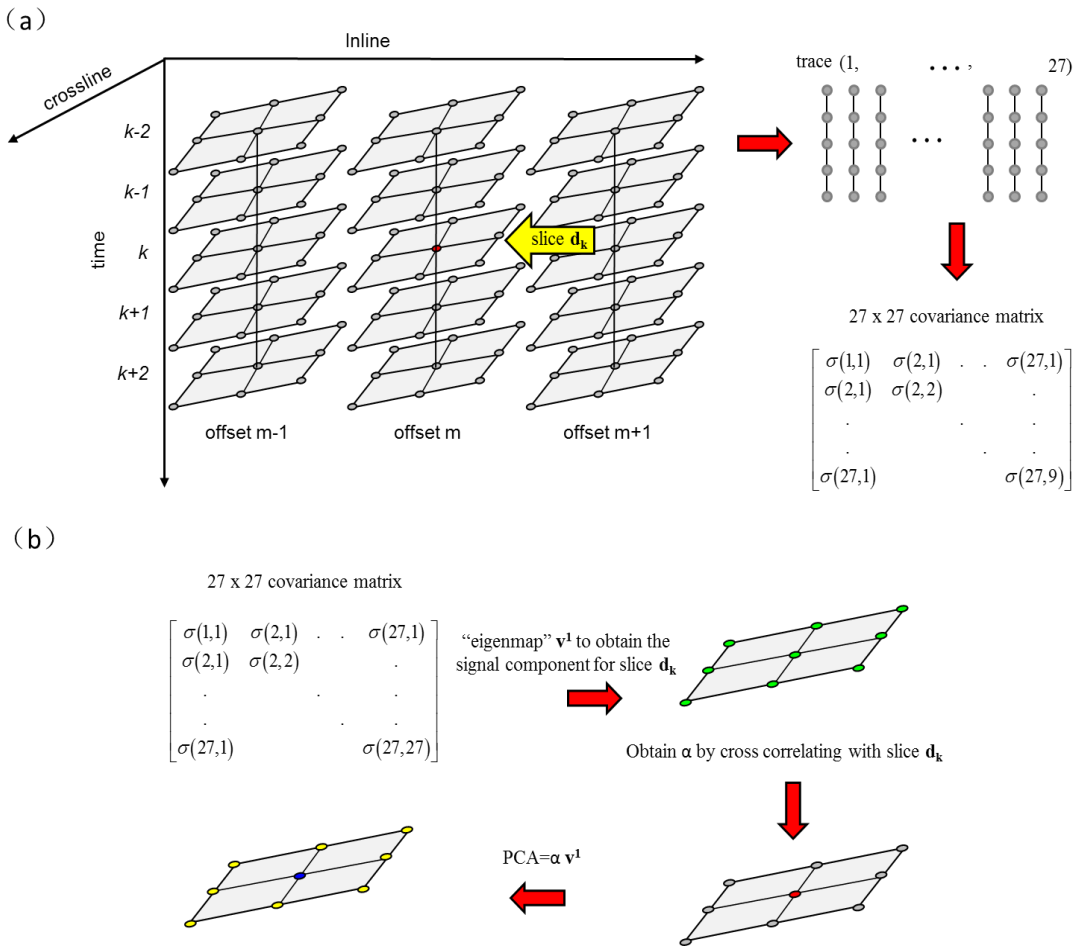

Figure 2.3a. Cartoon showing structure oriented filtering applied to prestack gathers in common offset domain along dip using a centered analysis window about the red analysis point. In this example there are 3 CDPs by 3 lines and 3 offsets resulting in a length 27 "sample vector" for each interpolated horizon slice at time k. These sample vectors are cross-correlated and averaged from *k*=-*K* to *k*=+*K* (*K*=2) time samples using equation 1 resulting in a 27 by 27 covariance matrix. We then obtain the signal pattern for the analysis point using "eigenmap".

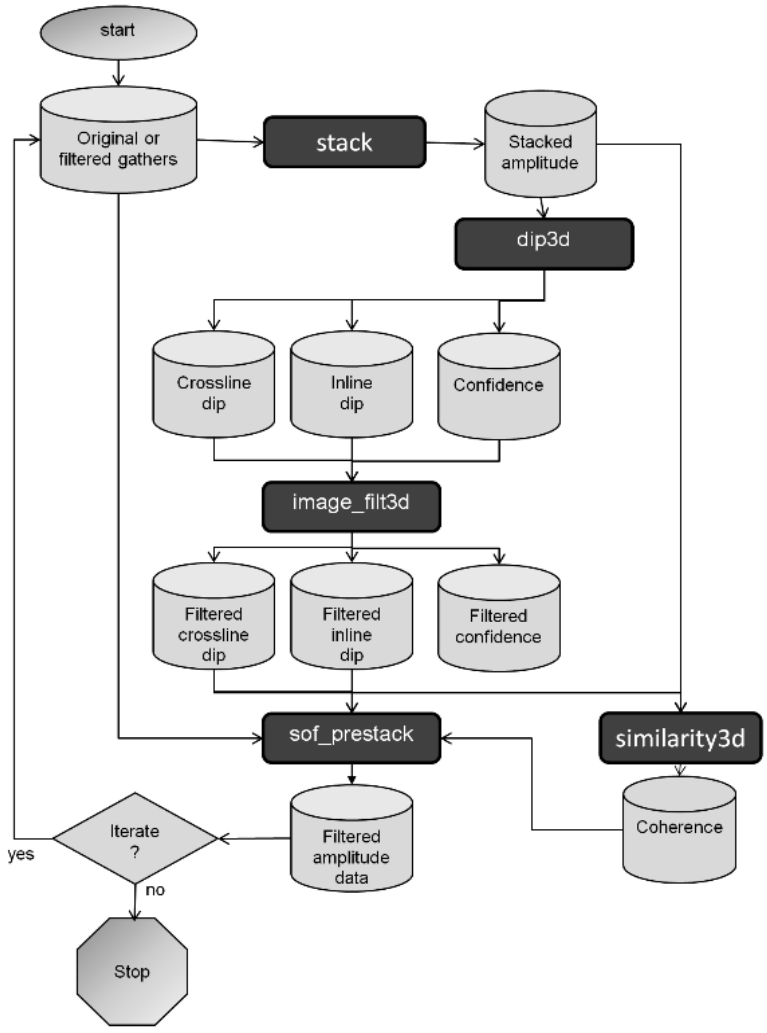

Figure 2.4. Prestack structure-oriented filtering workflow. (After Davogustto, 2011).

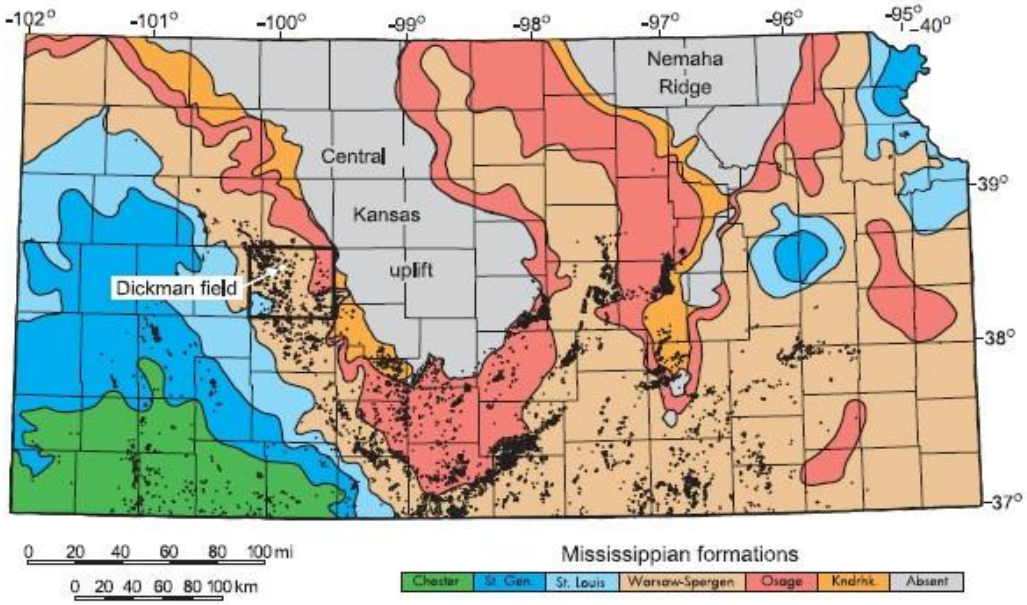

Figure 2.5. Map of the Mississippian subcrop in Kansas. Black box outlines Ness County, and the white block arrow indicates the location of Dickman Field. Black dots represent oil production. Colors represent different Mississipian-Age formations (After Nissen et al., 2009).

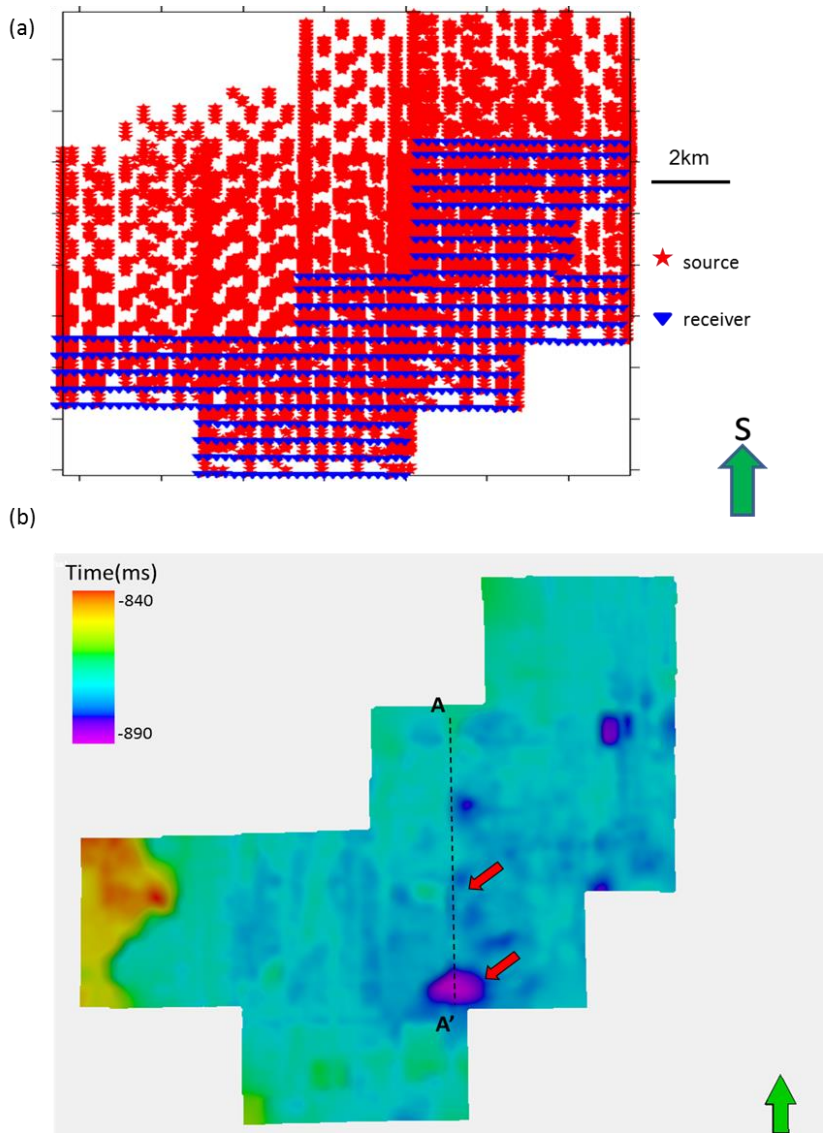

Figure 2.6. (a) Time-structure map of the top of the Gilmore City horizon, red arrows show collapse features.

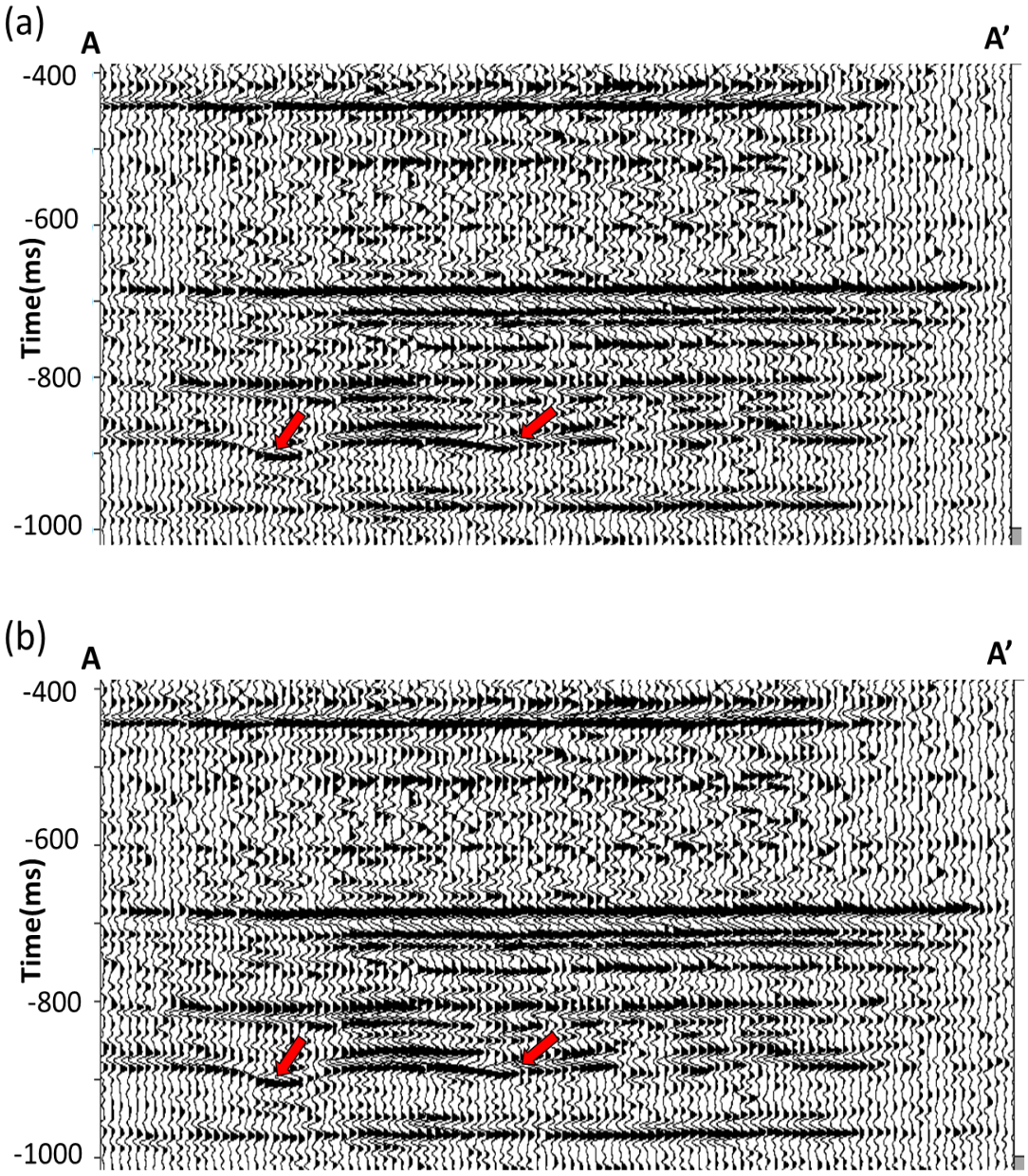
(a)
A
A'
-400
-600
-800
-1000
Time(ms)
(b)
A
A'
-400
-600
-800
-1000
Time(ms)

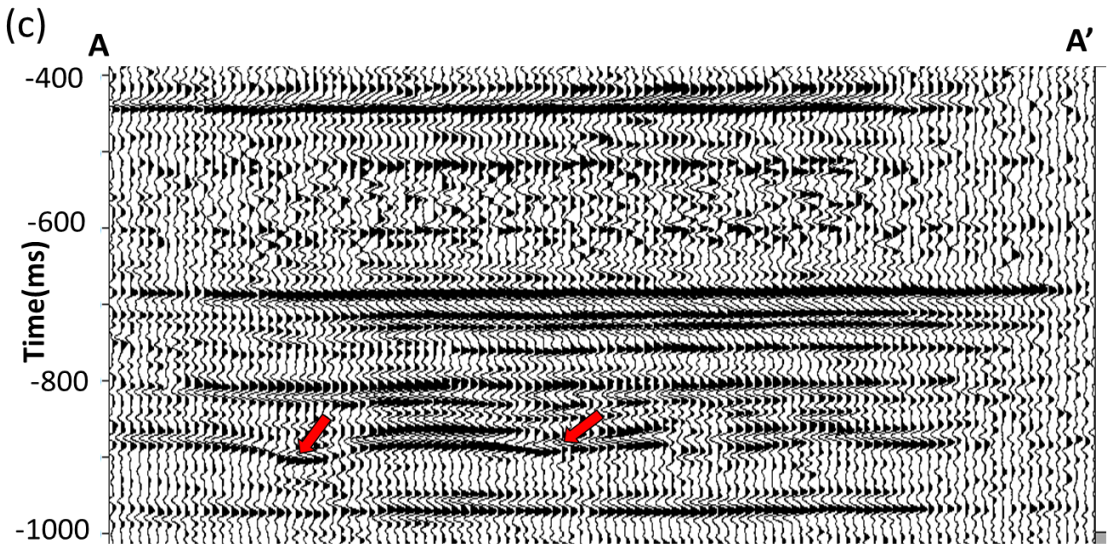

Figure 2.7. Vertical slice through seismic amplitude along profiles AA' as shown in Figure 2.5: (a) using conventional migration, and after (b) two, and (c) three iteration of PLSM. Red block arrows indicate Gilmore City horizon and the collapse features on it.

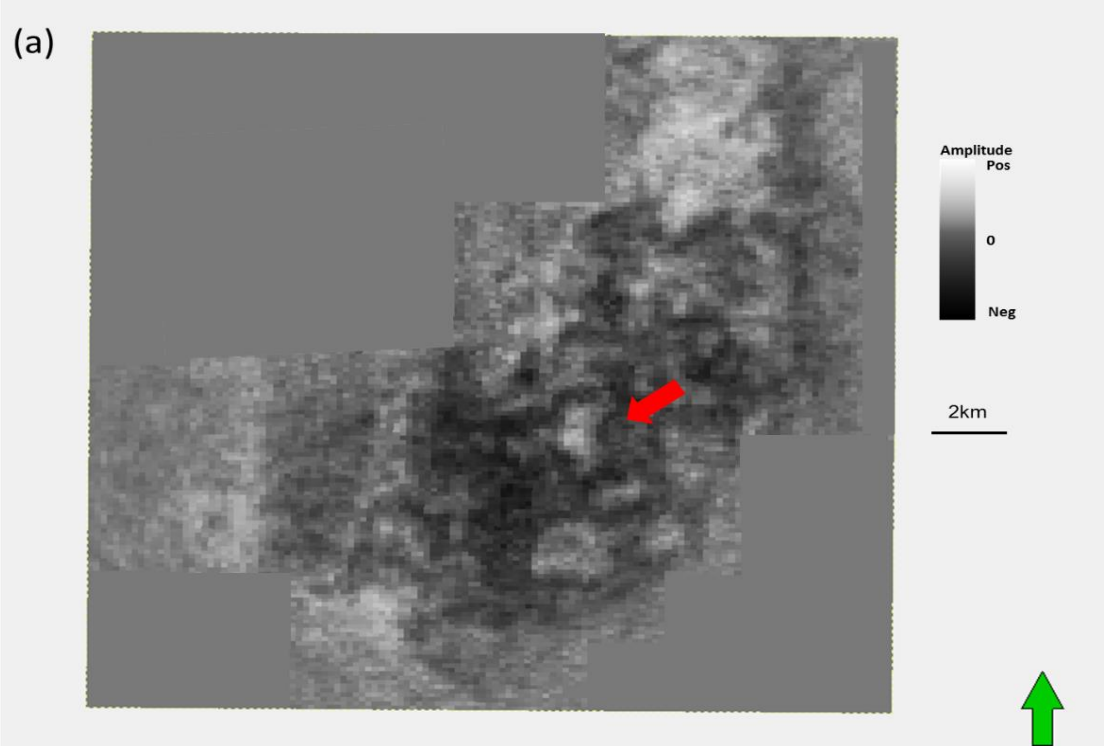
(a)
Amplitude
Pos
0
Neg
2km

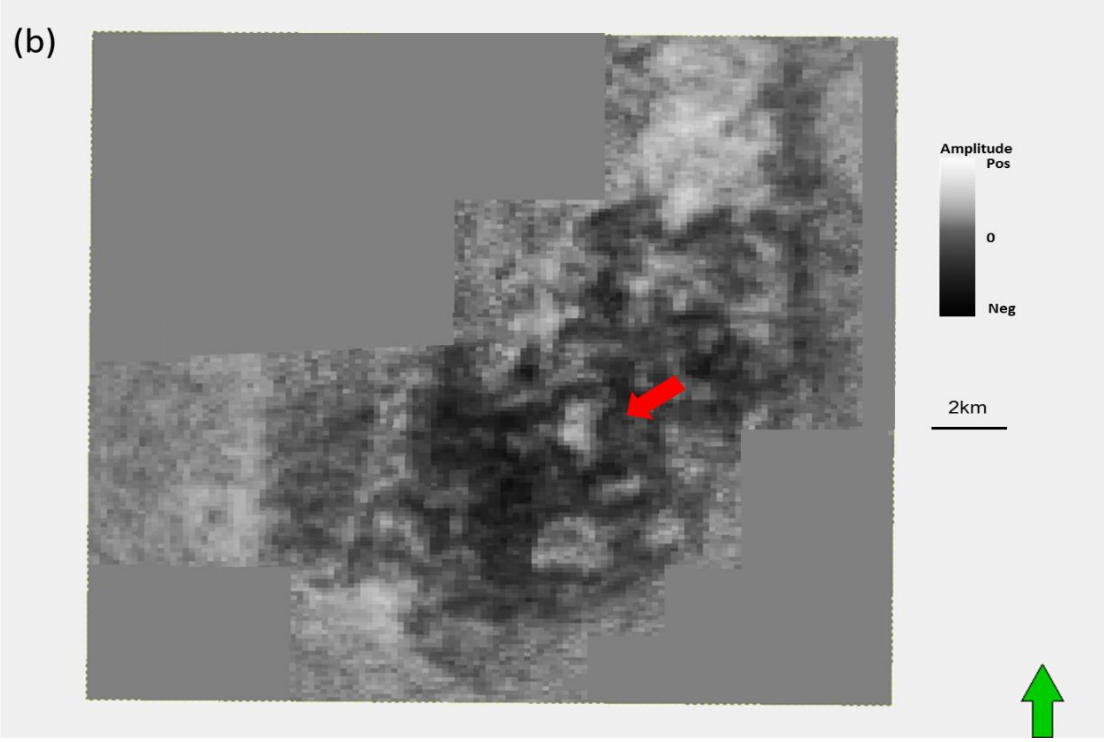
(b)
Amplitude
Pos
0
Neg
2km

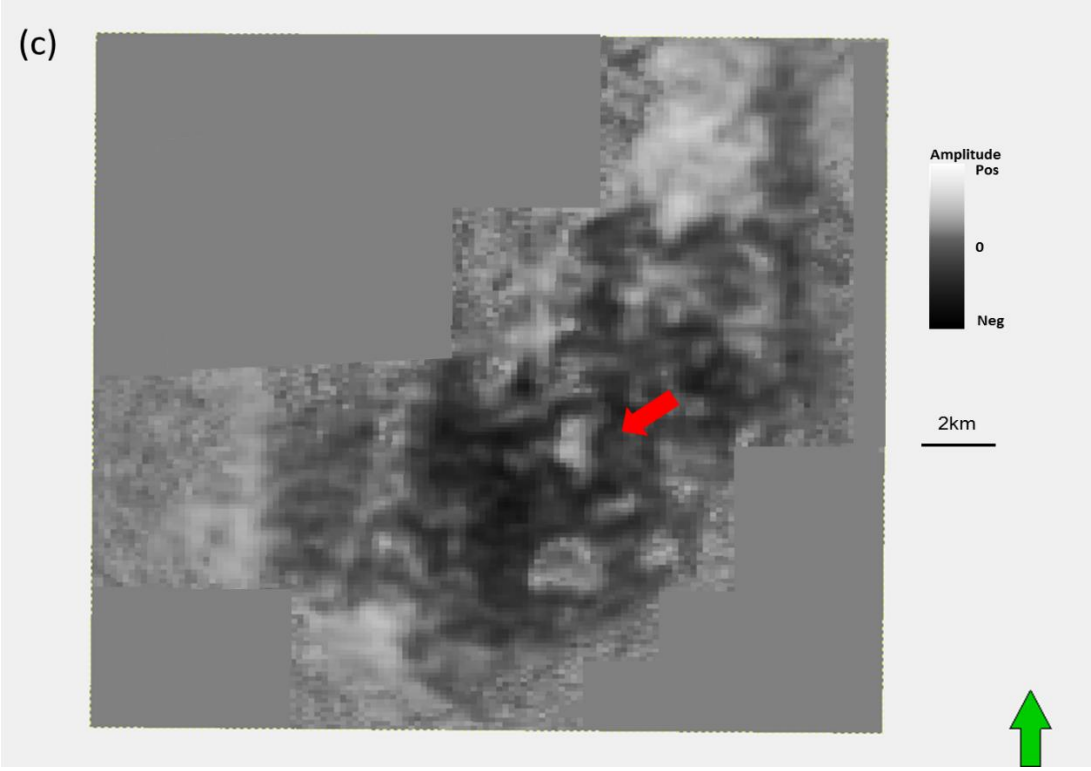

Figure 2.8. Time slice at t=0.88s through stacked amplitude volumes after (a) conventional migration and after (b) two, and (c) three iterations of PLSM. The red arrow in (a) indicates a collapse feature. PLSM attenuates these footprint artifacts after (b) two, and (c) three iterations and better image the collapse features.

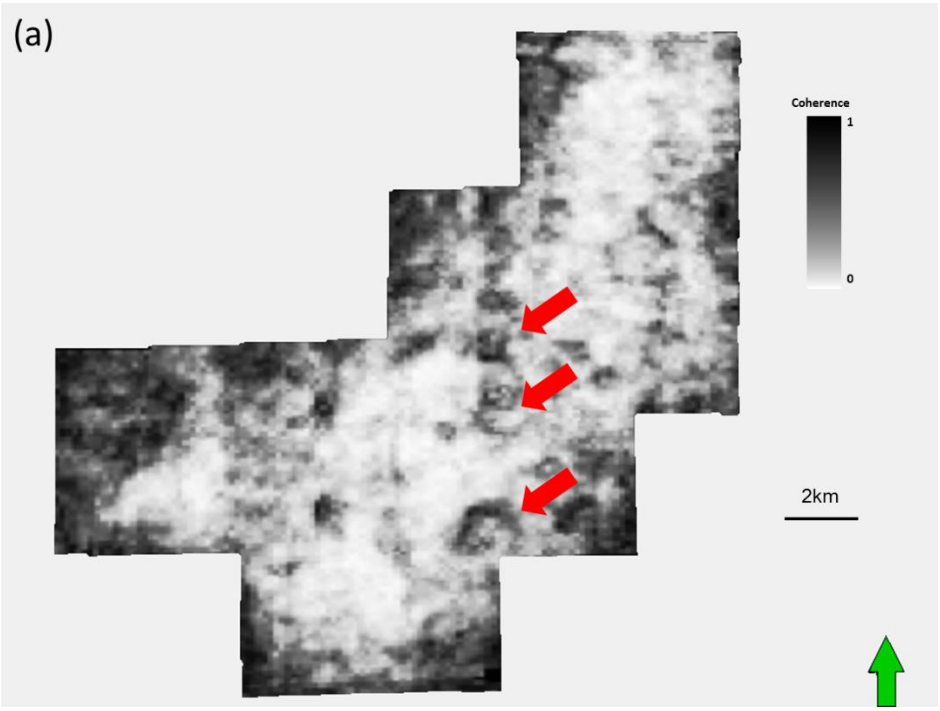
(a)
Coherence
1
0
2km

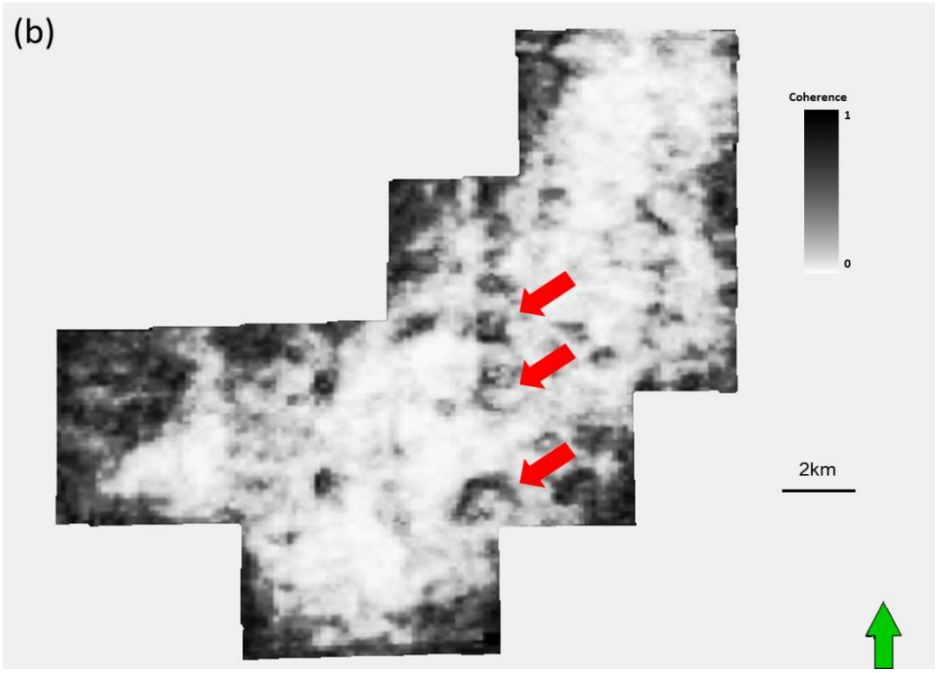
(b)
Coherence
1
0
2km

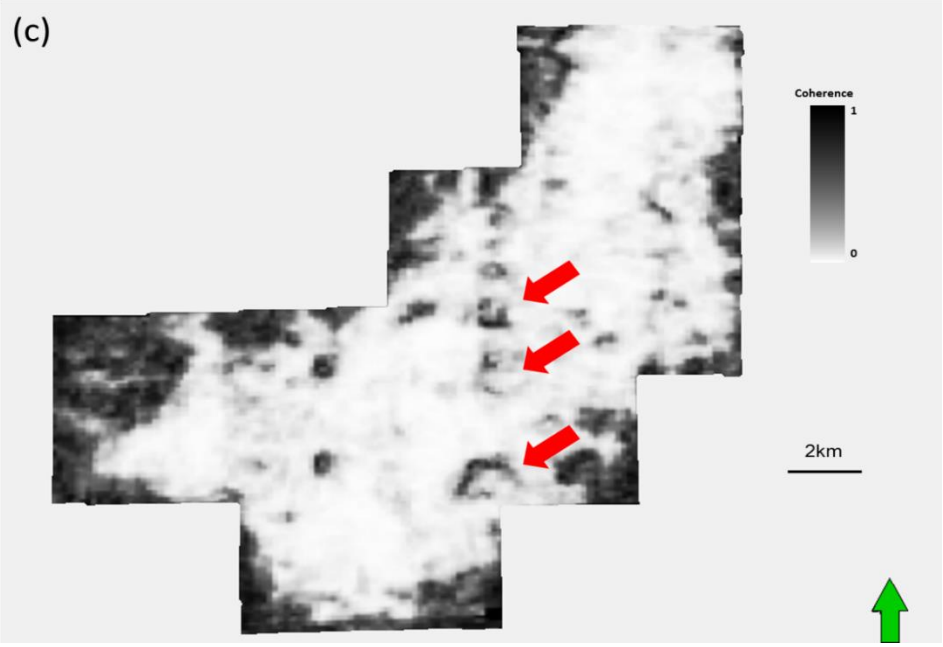

Figure 2.9. Horizon slices along the Gilmore City through coherence volumes computed from seismic amplitude: (a) using conventional migration, and (b) using two, and (c) three iterations of PLSM. Red block arrows indicate the karst collapse features.

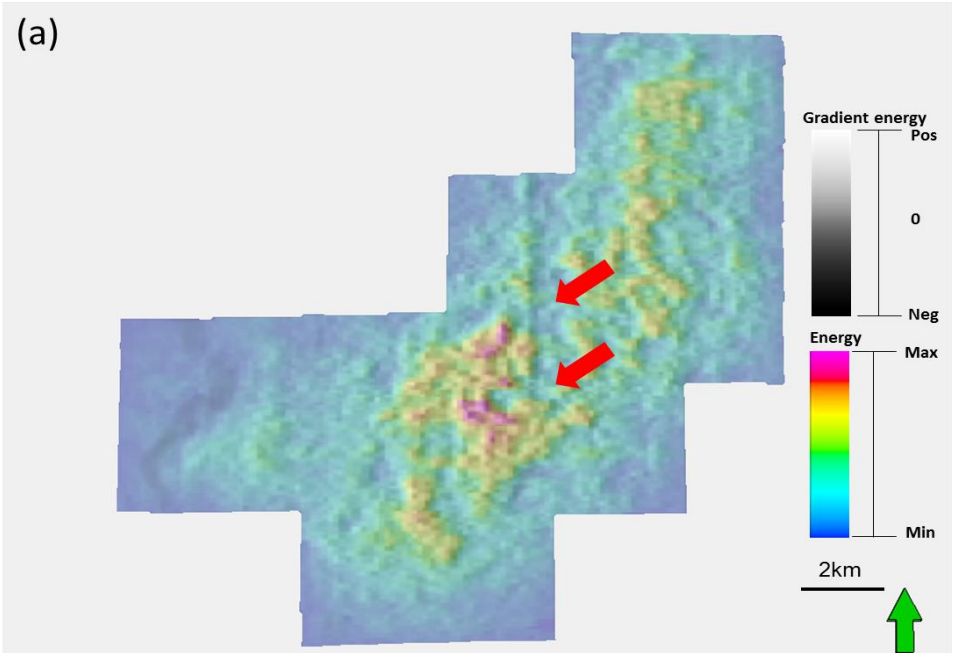
(a)
Gradient energy
Pos
0
Neg
Energy
Max
Min
2km

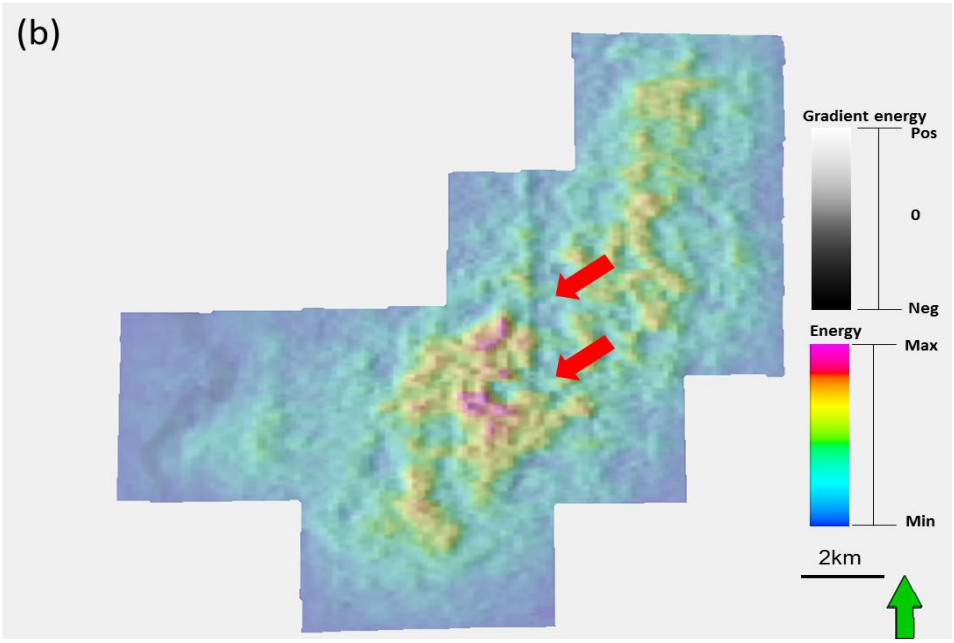
(b)
Gradient energy
Pos
0
Neg
Energy
Max
Min
2km

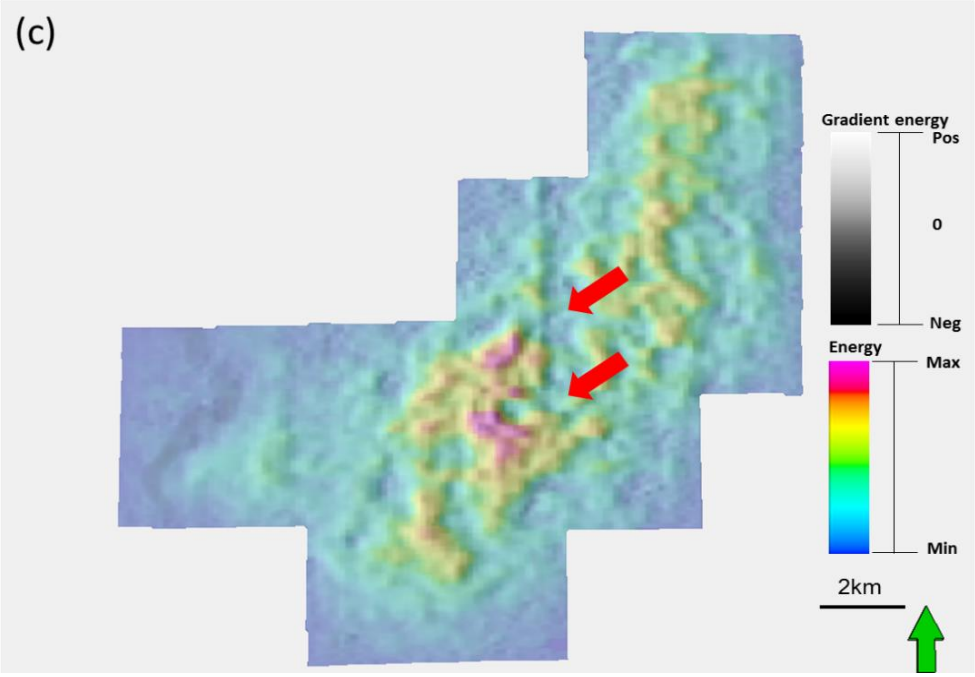

Figure 2.10. Horizon slices along the Gilmore City through inline gradient co-rendered with the coherent energy volumes computed from seismic amplitude (a) using conventional migration, and (b) using two, and (c) three iterations of PLSM. Red block arrows indicate the karst collapse features.

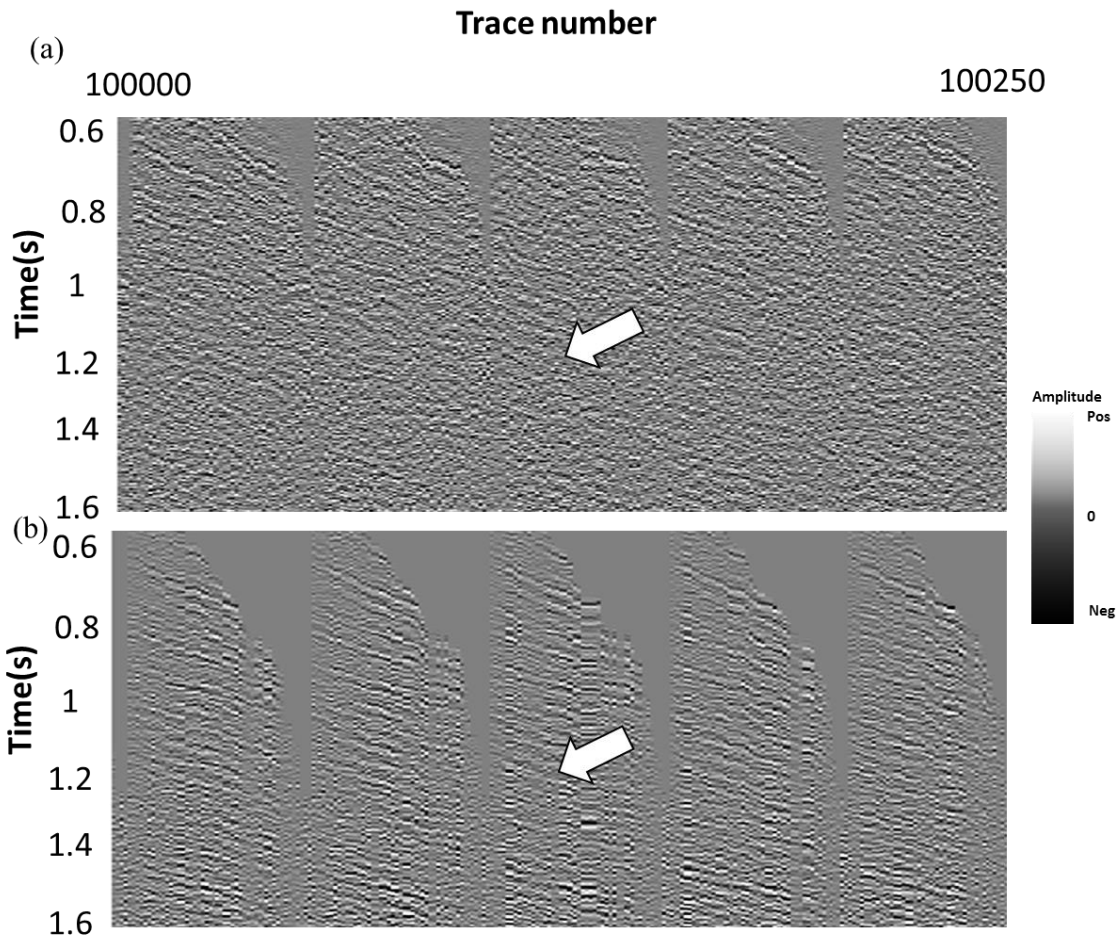

Figure 2. 11. Representative traces from (a) original seismic shot gathers data, (b) the third iteration of PLSM migration.

REFERENCES

Aoki, N., and G. Schuster, 2009, Fast least-squares migration with a deblurring filter: Geophysics, **74**, WCA83-WCA93.

Biondi, B., 2001, Kirchhoff imaging beyond aliasing: Geophysics, **66**, 654-666.

Biondi, B., 2006, 3D seismic imaging: Society of Exploration Geophysicists, 27-29.

Boncelet, C., R. Hardie, and G. Arce, 1991, LUM filters for smoothing and sharpening, in E. R. Dougherty, G. R. Arce, and C. G. Boncelet Jr, eds, Nonlinear image processing II: Proceedings of SPIE, **1451**, 70–73.

Cabrales Vargas, A., 2011, Suppression of aliasing artifacts on 3D land data via Constrained least-squares migration: M.Sc. thesis, Univ. of Oklahoma.

Chavent, G. and R.- E. Plessix, 1996, A time-domain derivation of optimal and suboptimal Kirchhoff quantitative migrations via a least-squares approach. National Institute for Research in Computer Science and Control, 3-38.

Caraba, E., 2008, Preconditioned conjugate gradient algorithm: BS Thesis, Louisiana State

University.

Claerbout, J. F., 1992, Earth soundings analysis: Processing versus inversion: Blackwell Scientific, 144-145.

Davogustto-Cataldo, O., 2011, Removing footprint from legacy seismic data volumes: M.Sc. Thesis, University of Oklahoma.

Fehmers, G., and F. W. Höcker, Fast structural interpretation with structure-oriented filtering: Geophysics, **68**, 1286-1293.

Falconer, S., and K. J. Marfurt, 2008, Attribute-driven footprint suppression: SEG

Expanded Abstracts, **27**, 2667-2671.

Gersztenkorn and Marfurt, 1999, Eigenstructure-based coherence computations as an aid to 3-D structural and stratigraphic mapping, **64**, 1468-1479.

Jovanovic, K., 2004, P and SV polarization filtering of a multicomponent vector VSP: M.S. thesis, Univ. of Houston. Processing II, SPIE, Vol. 1451, pp. 70-73

Kwiatkowski, J. T. and K. J. Marfurt, 2011, Data conditioning of Legacy pre-stack time migrated gathers from the Mid-Continent: 2011 AAPG ***Mid-Continent*** Section Meeting.

Kuwahara, M., K. Hachimura, S. Eiho, and M. Kinoshita, 1976, Digital processing of biomedical images: Plenum Press, 187–203.

Luo, Y., S. al-Dossary, and M. Marhoon, 2002, Edge-preserving smoothing and applications: The Leading Edge, **21**, 136–158.

Marfurt, K. J., 2006: Robust estimates of reflector dip and azimuth: Geophysics, **71**, P29-P40.

Nemeth, T., 1996, Imaging and filtering by least-squares migration: Ph. D. dissertation, Univ. of Utah.

Nemeth, T., C. Wu, and G. Schuster, 1999, Least-squares migration of incomplete reflection data: Geophysics, **64**, 208-221.

Nissen S.E., T.R. Carr, K.J. Marfurt, and E. C. Sullivan, 2009, Using 3-D seismic volumetric curvature attributes to identify fracture trends in a depleted Mississippian carbonate reservoir: Implications for assessing candidates for CO2 sequestration: AAPG Studies in Geology, **59**, 297–319.

Perez, G., and K. J. Marfurt, 2008, New azimuthal binning for improved delineation of faults and fractures: Geophysics, **73**, S7–S15.

Schuster, G. T., 1993, Least-squares crosswell migration: 64th International Exposition and Annual Meeting, Expanded Abstract, 110-113.

Schuster, G. T., 1997, Acquisition footprint removal by least-squares migration: 1997 Annual UTAM Report, 73-99.

Wang, J., and M. Sacchi, 2009, Structure constrained least-squares migration: SEG 2009 International Exposition and Annual Meeting, 2763-2767.

Wei, D., and Schuster, G. T., 2011, Least-squares migration of multisource data with a deblurring filter: Geophysics, **76**, 135-146.

Zhang, Y., M. Karazincir, C. Notfors, J. Sun, and B. Hung, 2002, Amplitude preserving v(z) prestack Kirchhoff migration, demigration and modeling: 64th EAGE Conference, 27-30.

Chapter 3: Migration driven 5D interpolation of low fold Dickman and Legacy survey

Shiguang Guo[1], Sumit Verma[1], and Kurt J. Marfurt[1],

[1]The University of Oklahoma, ConocoPhillips School of Geology and Geophysics

ABSTRACT

One of the major challenges in seismic data processing is inadequate sampling along the horizontal axes, which generate artifacts in subsequent image seismic processing. Inadequate sampling give rise to acquisition footprint in stacked images, missing azimuths which hinder AVAz analysis, and missing offsets which hinders AVO analysis.

In order to compensate for limited sampling and reconstruction of the missing data, I propose a new interpolation algorithm. This algorithm is based on pre-conditioned least-squares migration, and produces at least one trace in each offset azimuth bin.

I test my algorithm on two Mississippian Limestone surveys, one from Kansas and one from north Texas. The fold of these two surveys are highly unbalanced while the seismic data are contaminated by the groundroll, such that resulting attributes suffer from strong acquisition footprint. The 5D interpolation algorithm applied to the data before and after groundroll results in degraded subsurface images. However 5D interpolation after groundroll suppression reduces footprint and provide the missing offset and azimuths needed for more quantitative analysis.

INTRODUCTION

Inadequate sampling has always been a problem for seismic acquisition. Obstacles give rise to gaps during land seismic acquisition which can cause migration artifacts. Missing azimuths hinder AVAz analysis and prestack inversion, while missing offsets hinder AVO and prestack inversion analysis. To address these data sampling limitations, various methods of 5D interpolation have been applied to predict missing data in otherwise sparse seismic surveys. Ideally the result is a more uniform distribution, increasing the signal-to-noise ratio and suppressing acquisition footprint

To address these issue, Liu and Sacchi (2004) introduced a minimum weighted norm interpolation algorithm, Xu et al. (2005) introduced an anti-leakage Fourier transform algorithm, while Abma and Kabir (2006) introduced a convex projection algorithm. Most recent variations of these methods are reported by Stein et al. (2010) and Wojslaw et al. (2012). Chopra and Marfurt (2013) used volumetric attributes to show the reduction in artifacts but a decrease in lateral resolution provided by the minimum weighted norm. Most current 5D interpolation algorithms tries to interpolate missing source and receiver pairs neighboring moveout-corrected common midpoint gathers. In this dissertation, I will use demigration to construct missing data. I hypothesize that such a “wave equation” based algorithm will accurately interpolate not only specular reflections but also the nonspecular diffractions needed to improve lateral resolution.

I began with a brief overview of preconditioned least-squares migration, showing how one can add the missing traces in the demigration step, I then apply this workflow to two Mississippian Lime surveys, one from Kansas, Country, the other from Texas. On the second application, I examine the effectiveness of 5D interpolation on data

contaminated by land groundroll. I conclude by using coherence and curvature to show the ability of this workflow to minimize random noise, suppress footprint and retain sharp edges associated with karst and faults.

METHODOLOGY

The first step in interpolation is to define an interpolation template. Figure 3.1 shows such a template before and after interpolation. The goal is to have an equal amount of trace energy within each offset-azimuth bin (or alternatively, each vector tile). For conventional, "true amplitude" migration, if there are *n* recorded traces within a given bin, each trace will be divided by *n*. If there are no traces within a given bin, a single trace will be interpolated. Least-squares migration will compensate for the variable numbers of traces pre bin.

I construct a 5D interpolation workflow based on a least-squares migration engine. Normalizing the surface data by *n* (if there are *n* traces per bin) is useful for the first iteration of (conventional) migration. Subsequent "least-squares" migration and demigration will choose an appropriate weight to equalize the data. Aliased noise will be suppressed in the subsurface migrated domain at each iteration through the application of filters that preserve the geology and reject cross-cutting noise. Such filtering within a conjugate gradient solution preconditions each iteration of our least-squares migration-demigration loop, resulting in the preconditioned least-squares migraiton algorithm developed by Guo et al. (2012).

PLSM provides a subsurface reflectivity that when modeled (demigrated) best represents the data measured at the earth's surface. Because of data and operator aliasing, many alternative subsurface images can predict the sparse surface data. I address this

limitation by applying geologically reasonable structure-oriented filters to the migrated image at each iteration. To interpolate the data and minimize operator aliasing, at subsequent iterations I then predict the data not only at the measured surface locations, but also at surface locations that were not occupied. The end result is an image that will be geologically reasonable and provides intermediate azimuthal and offset gathers amenable to prestack inversion and anisotropy analysis that honor the measured surface data.

APPLICATION

Dickman survey

Within Dickman field, Ness Co., KS (Figure 2.1), karst-enhanced fractures have been documented to extend several meters below the regional Mississippian unconformity surface. The Pennsylvanian Cherokee shale unconformably overlie the Mississippian reservoir rocks of the Meramecian Spergen and Warsaw limestone (Figure 3.3). I interpolate missing traces for each CMP bin through demigration using the workflow thown in Figure 3.2. The resulting 5D interpolation data volume provide a more uniform fold coverage (Figures 3.4).

Note the footprint noise is suppressed after 5D interpolation in shallow part Figures 3.5a and 3.5b. Representative vertical slices through the seismic data volume in Figures 3.6b and 3.6d show the improvements in amplitude balancing provided by 5D interpolation. Diffractions are also accurately interpolated, such that I am able to better construct lateral discontinuities (karst) illuminated by coherence. Specifically the karst features (indicated by red arrows) are barely seen in Figure 3.6a and 3.6c. Figures 3.7b and 3.7d shows the suppression of footprint seen on time slices through coherence at the

target level. The karst features are highlighted from edge area of the survey after 5D interpolation when compared with Figure 3.7a and Figure 3.7c.

5D interpolation with PLSM improves seismic amplitude balancing. This allows for better imaging of geological features, less footprint, and improved edge detection, the karst collapse in the Mississippian limestone can be better illuminated with 5D interpolation.

Eastern shelf, TX

The Mississippi Lime of Kansas and Oklahoma is one of the newer resource plays. The target is relatively shallow, the surface infrastructure is in place, and many small operators already hold the acreage from shallower or deeper production. Advancements in horizontal drilling, acidation, hydraulic fracturing, and efficient disposal of large volumes of water make these reservoirs economic. The Mississippi Lime is laterally highly heterogeneous compared to the other resource plays. The major rock types are tripolitic chert, fractured tight chert, and tight limestone. The tripolitic and fractured chert have good porosity and good production in northern Oklahoma and southern Kansas. My survey was acquired on the eastern shelf between the Midland Basin (Permian Basin) and Fort worth Basin, Texas. In this area, there is no Woodford Shale, and the Mississippian tripolitic chert lies directly above the Ellenburger Limestone at a depth of 6000-8000 ft.

Groundroll suppression

Clear Fork Energy provided me with four surveys covering 80 mi^2. Dawson Geophysical had already done the merge, and provided me the data with elevation statics

and spiking deconvolution applied. While the maximum offset of the two larger surveys is 12000 ft, the two smaller surveys in the top middle of the merged area that contain most of the well control have a significantly smaller maximum offset of 8000 ft. The mixed offset ranges give rise to some challenges in prestack migration and inversion. Survey 4 in the middle (Figure 3.10) has an E-W source line direction while the other three surveys have N-S source line directions.

5D interpolation through PLSM

The average fold of the data shown in Figure 3.10b is 15 for a nominal bin size of 110 ft by 110 ft. Figure 3.11a shows a representative prestack gather after conventional migration. Note the noise as shown by red arrow that contaminates this image, to better understand the origin of this migrated noise, we demigrated the mutes as shown in Figure 3.11b, and demigrated the data. The corresponding results are shown from Figure 3.12a and b, Figure 3.12a displays reconstructed gathers after demigration from migration results in Figure 3.11a, note the seismic signal and groundroll noise after demigration, Figure 3.12b displays reconstructed groundroll noise from demigration on prestack gathers from Figure 3.11b with groundroll kept, the reconstructed groundroll demonstrates that groundroll noise from raw gathers can cause coherent noise in prestack volume from migration.

Figure 3.13 shows strong groundroll contaminates the target from 950 ms to 1100 ms. Groundroll is source generated coherent and dispersive noise. Since the velocity of the groundroll is low and travels horizontally, it is easily aliased by the coarse surface sampling. Normally, the power of stacking (or migration) further attenuates groundroll, but in this data set the fold is too low to do so. Verma (2014) applied a workflow suppressed the groundroll, firstly he applied low-pass filter (f<50 Hz) the data, 3D patch

by 3D patch. Then the linear moveout is used to flatten the groundroll phases, estimate the dip about this reference moveout, and compute coherence within a 3-channel by 3-shot by 20 ms window about each sample. Using a Kuwahara algorithm, we got the modeled groundroll from the original data by choosing the most coherent window within which we apply a structure-oriented KL filter. Figure 3.14a and b show a representative prestack migrated gathers after just groundroll suppression and after prestack structural oriented filter applied. Red arrows denotes the same reflection events, note less noise contamination after prestack SOF applied. Figure 3.15a shows a time structural map of Ellenburger Limestone, note the main faults system. Figure 3.15b and c shows fold map before and after 5D interpolation, there is low fold coverage on the boundary area of merging before 5D interpolation, the fold coverage get balanced after 5D interpolation applied.

Figure 3.16a shows vertical slices through the seismic amplitude volume along profiles AA' (shows in Figure 3.15a) of conventional migration, the absence of groundroll noise causes noise contamination as shown by the red arrow. In addition, low random noise masks subtle geological features denoted by the red block arrow. After groundroll suppression as shown in Figure 3.16b, the signal to noise ratio has been enhanced at target horizon shown. After we applied prestack structural oriented filer, there is a reduction in noise and geological features (e.g. faults) are more clearly illuminated. Figure 3.16d shows same vertical slice but after 5D interpolation through PSLM. Note the improvement in amplitude balancing as shown by black arrows, higher lateral resolution and less noise contamination as shown by red arrow, which provides

better illumination as it is easier to interpret (if we use the seismic attributes along with seismic amplitude volume) after 5D interpolation..

Figure 3.17a shown vertical slices through the seismic amplitude volume along profiles BB' (shows in Figure 3.15a) of conventional migration, red block arrows denote the Ellenburger Limestone, the low signal to noise ratio and noise make it difficult for identification of fault as dash line shown. After groundroll suppression as shown in Figure 3.17b, note less noise interference, and the fault denoted by dash line shows a little more illumination. After structural oriented filter applied from Figure 3.17c, there is big reduction in noise. Figure 3.17d shows same vertical slice after 5D interpolation through PSLM, note there is higher lateral resolution, the fault shows sharper discontinuity and is to be shown more clearly.

Figure 3.18a shows a time slice at t=0.62 s through the stacked volume after conventional migration. The area shown by red block arrow indicates aliased noise and footprint. After groundroll suppression as shown from Figure 3.18b, note there is less noise contamination and higher the signal to noise ratio indicated by red block arrow. Figure 3.18c displays the same time slice after prestack SOF, the SOF reduces the footprint noise at some extent, but there is still strong footprint pattern which interferes with interpretation of subtle geological features. Finally, I apply 5D interpolation through PSLM as displayed in Figure 3.18d. The footprint is suppressed while the structural features are retained.

Figure 3.19a show same time slice (in Figure 3.18a) in k_x-k_y domain through stacked seismic volume after SOF applied, note the footprint noise is characterized by energy focused

points donated by red arrow, after 5D interpolation applied, the footprint noise pattern from k_x-k_y domain is suppressed as shown by red arrow.

Figure 3.20a shows horizon slices through energy ratio similarity volumes along the Ellenburger Limestone after conventional migration. The red block arrow denotes the fault. Note contamination by groundroll noise on the coherence attribute masks the faults. After groundroll suppression (Figure 3.20b), some of the random coherent features are suppressed. I apply prestack SOF (Figure 3.20c). Crosscutting noise is further reduced resulting in a cleaner fault system, the faults system shows higher illumination as denoted by red block arrow. 5D interpolation through PSLM (Figure 3.20d) further reduce footprint yet retain the sharp fault discontinuity.

Figure 3.21a shows coherence horizon slices through most negative curvature volumes along the Ellenburger Limestone after conventional migration. The red block arrow denotes the fault, note poor fault illumination due to contamination of groundroll noise. After groundroll suppression in Figure 3.21b, contaminating noise from groundroll is suppressed. Then we applied SOF in Figure 3.21c, the faults system is characterized by most negative curvature with less noise interference. The same structural slice after 5D interpolation through PSLM is shown in Figure 3.21d, note improved fault illumination on most negative curvature as denoted by red block arrow and footprint noise is mostly removed.

Figure 3.22a shows horizon slice through most negative curvature co-rendered with coherence volume along the Ellenburger Limestone after conventional migration. The red block arrow denotes the fault, notice the difficult interpretability of fault in the presence of groundroll noise. In addition, note there is good correlation between high

coherence and most negative curvature. The same structural slice after 5D interpolation through PSLM is shown in Figure 3.22b, note big improvement for fault illumination, which is characterized by high coherence and most negative curvature.

Figure 3.23a and b show horizon slices through envelope along the Ellenburger Limestone after conventional migration and groundroll suppression. The red block arrow denotes the fault, notice the difficult interpretability of fault in the presence of groundroll noise. After I apply prestack structural oriented filter and 5D interpolation through PSLM as shown from Figure 3.23c and d, note the sharp fault discontinuity as denoted by black arrows.

Figure 3.24 shows the well synthetic to seismic correlation at well A. The synthetic to seismic correlation with seismic data after groundroll suppression and before 5D interpolation shows a decent correlation in the zone of interest. But, if we look closely the correlation is improved significantly after the 5D interpolation. The correlation number has also increased from 38% to 53%. Here, I am just showing one well, but improvements in well to seismic tie after 5D interpolation was observed on several other wells too.

CONCLUSIONS

5D interpolation through PLSM has been proved to be an effective tool for recovering the seismic reflection due to low fold coverage, balance the seismic amplitude, and suppress the footprint noise, while retain lateral resolution associated with diffractions caused by faults.

The success application of 5D interpolation through PSLM on Dickman survey shows that 5D interpolation can help to balance the fold coverage, interpolate reflections and improve amplitude balancing. In addition, it increases the lateral resolution for karst features imaging and attribute illumination.

The legacy survey is suffered by groundroll noise, the first attempt of merely 5D interpolation through demigration didn't improve seismic image quality and attribute interpretation. Afterward, the application of 5D interpolation through PLSM to groundroll noise suppression gathers allow us to eliminate the footprint noise, increase signal to noise ratio and further better interpretation.

ACKONWLEDGEMENTS

Thanks to Clear Fork Inc., especially Alex Eagle for providing us seismic volume, encouragement and the authorization to publish this work, and sponsors of Attribute-Assisted Seismic Processing and Interpretation Consortium (AASPI) for their guidance and financial support.

LIST OF FIGURES

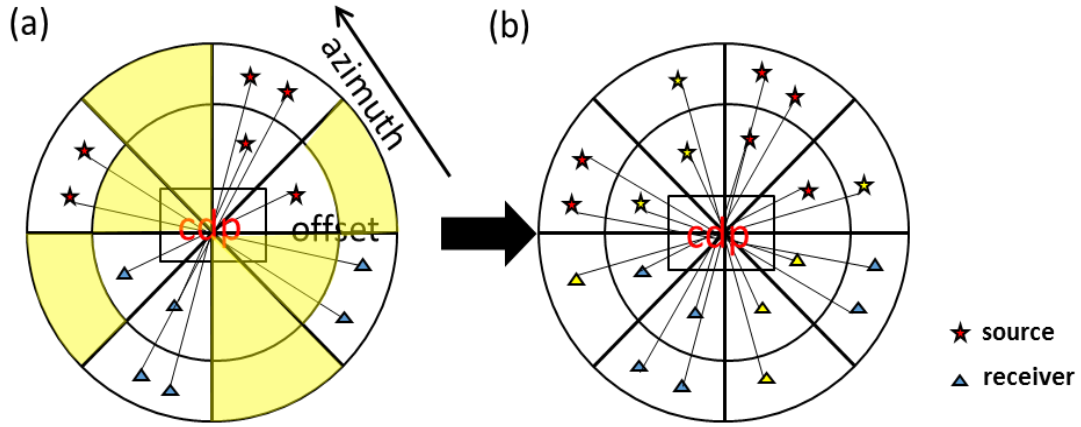

Figure 3.12. Cartoon showing a CMP with two offsets and four azimuthal sectors. (a) Measured data with four filled and four empty bins. (b) After interpolation each bin has at least one trace.

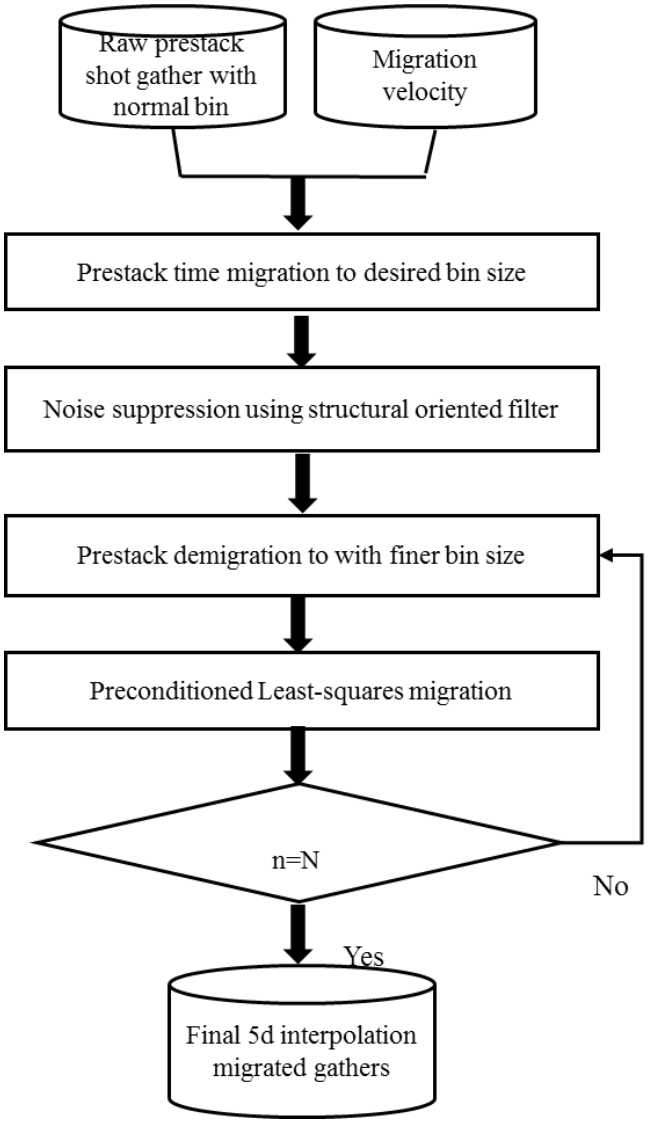

Figure 3.13. Workflow showing Migration driven 5D interpolation.

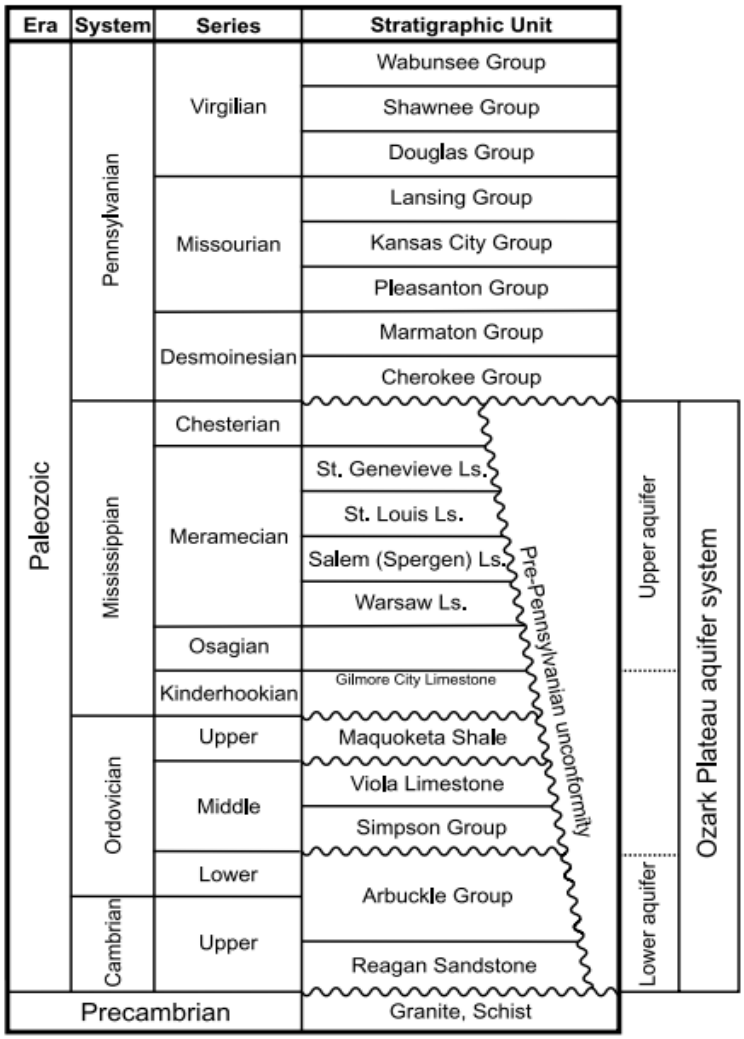

Figure 3.14. Generalized stratigraphic column for central Kansas. (Modified from Cansler, 2000), within Dickman Field, the St. Genevieve and St. Louis, Limestone are absent, such that the Spergen and Salem Limestone are sealed by the overlying Cherokee shale.

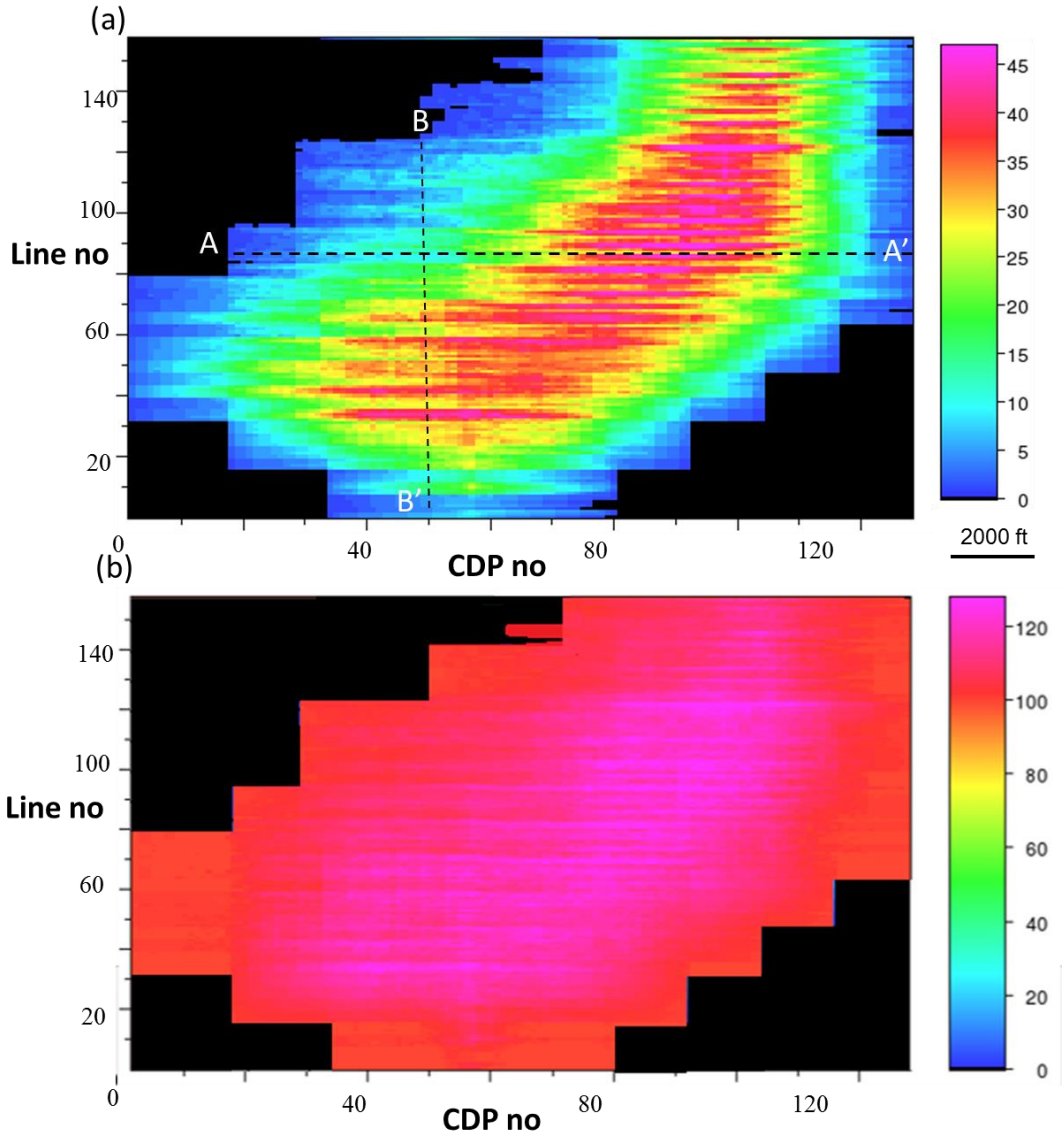

Figure 3.15. Fold map of the Dickman survey (a) before and (b) after interpolation. By construction the fold after interpolation is better balanced. The nominal bin size used was 82.5 ft by 82.5 ft.

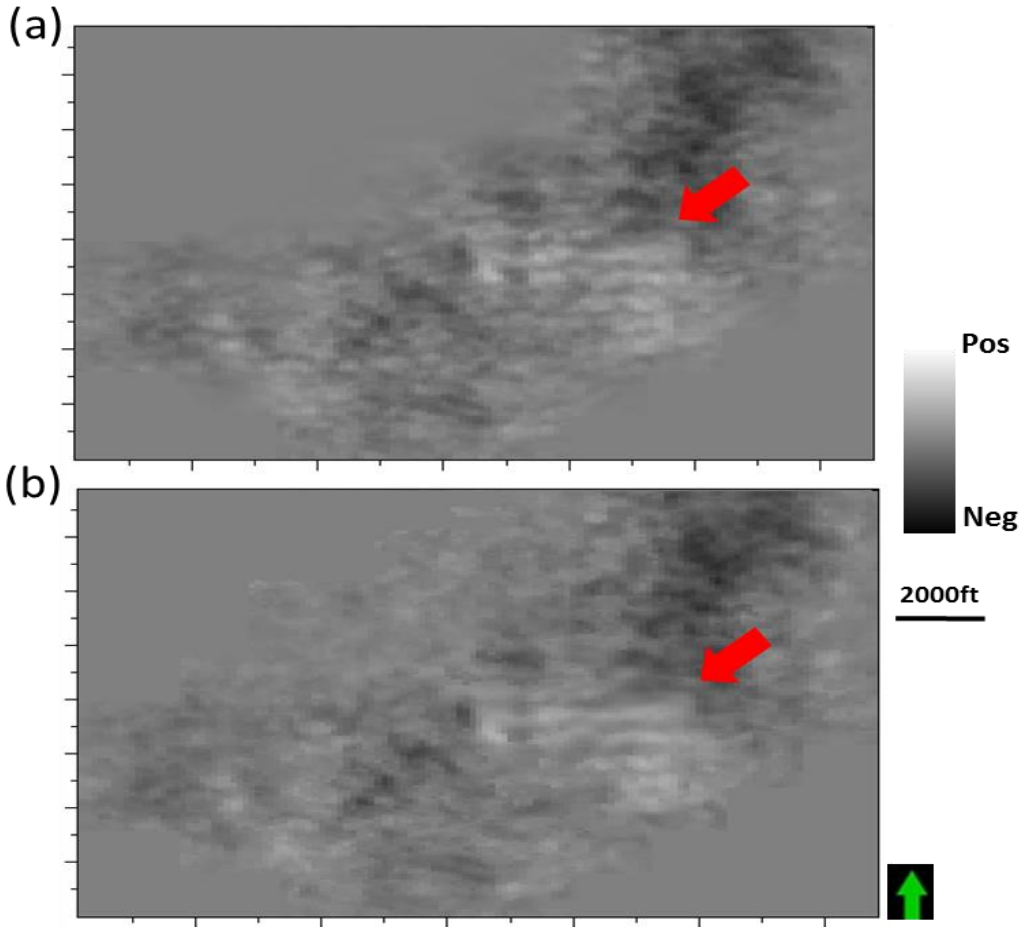

Figure 3.16. Time slice at t=0.38 s through stacked volume (a) after conventional migration, (b) after 5D interpolation. Red arrows denote footprint suppressed.

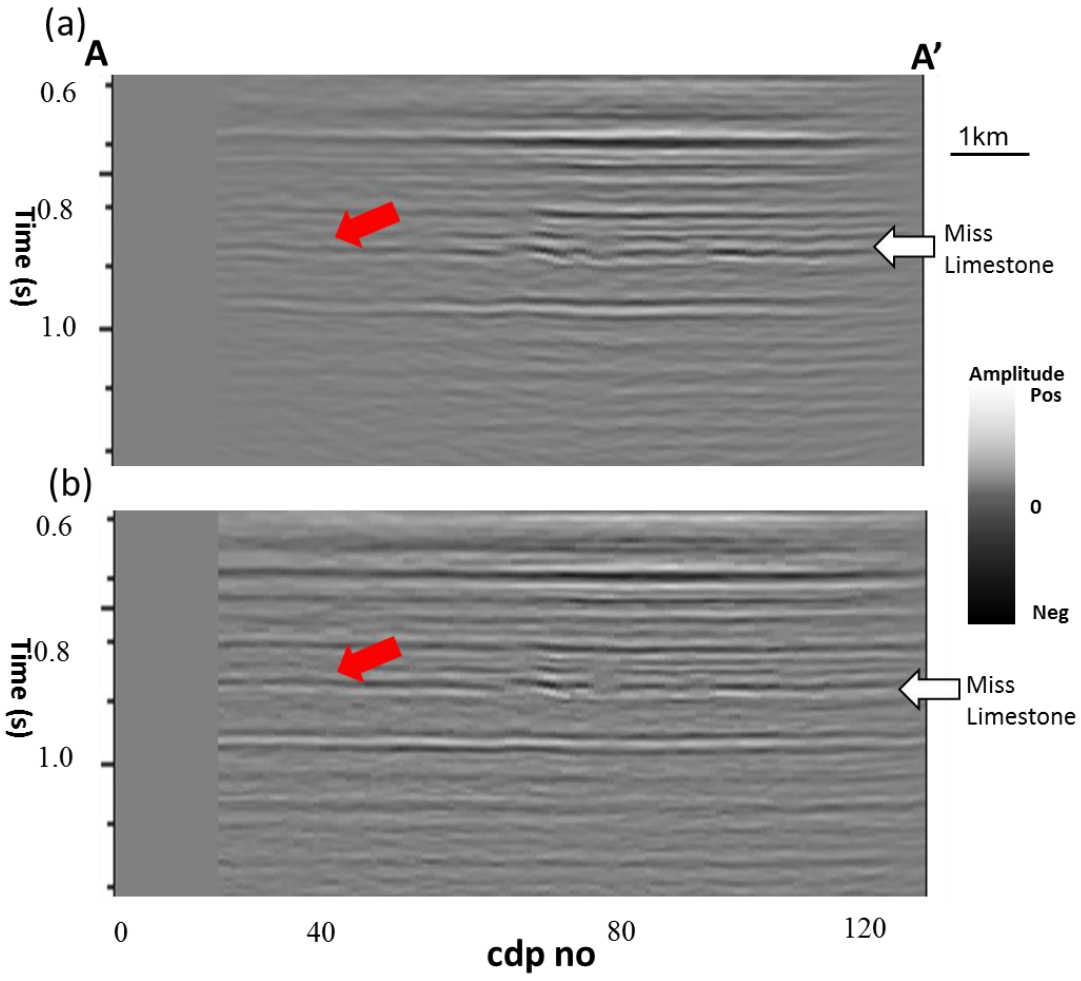
(a)
A
A'
0.6
0.8
1.0
Time (s)
1km
Miss
Limestone
Amplitude
Pos
0
Neg
(b)
0.6
0.8
1.0
Time (s)
Miss
Limestone
0
40
80
120
cdp no

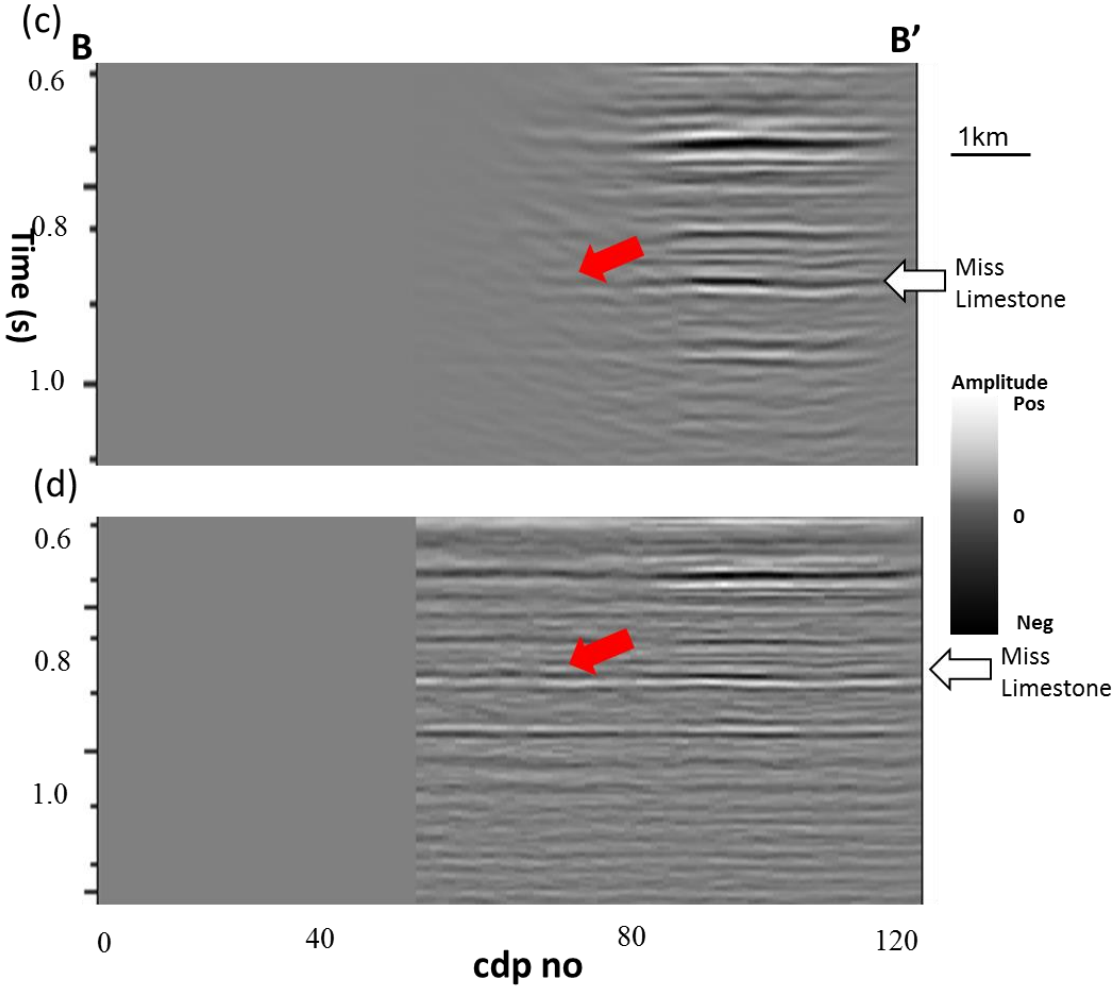

Figure 3.17. Vertical slices along line AA' and BB' through stacked volumes (a) before and (b) after 5D interpolation. Red arrows denote a seismic reflection at the intersection of the two lines (line location shown in Figure 2.4). Note the better balanced amplitude after interpolation on the left side of (b) and (d). The vertical resolution at the Gilmore City level below the target Mississippian is also significantly improved in (d) when compared to (c).

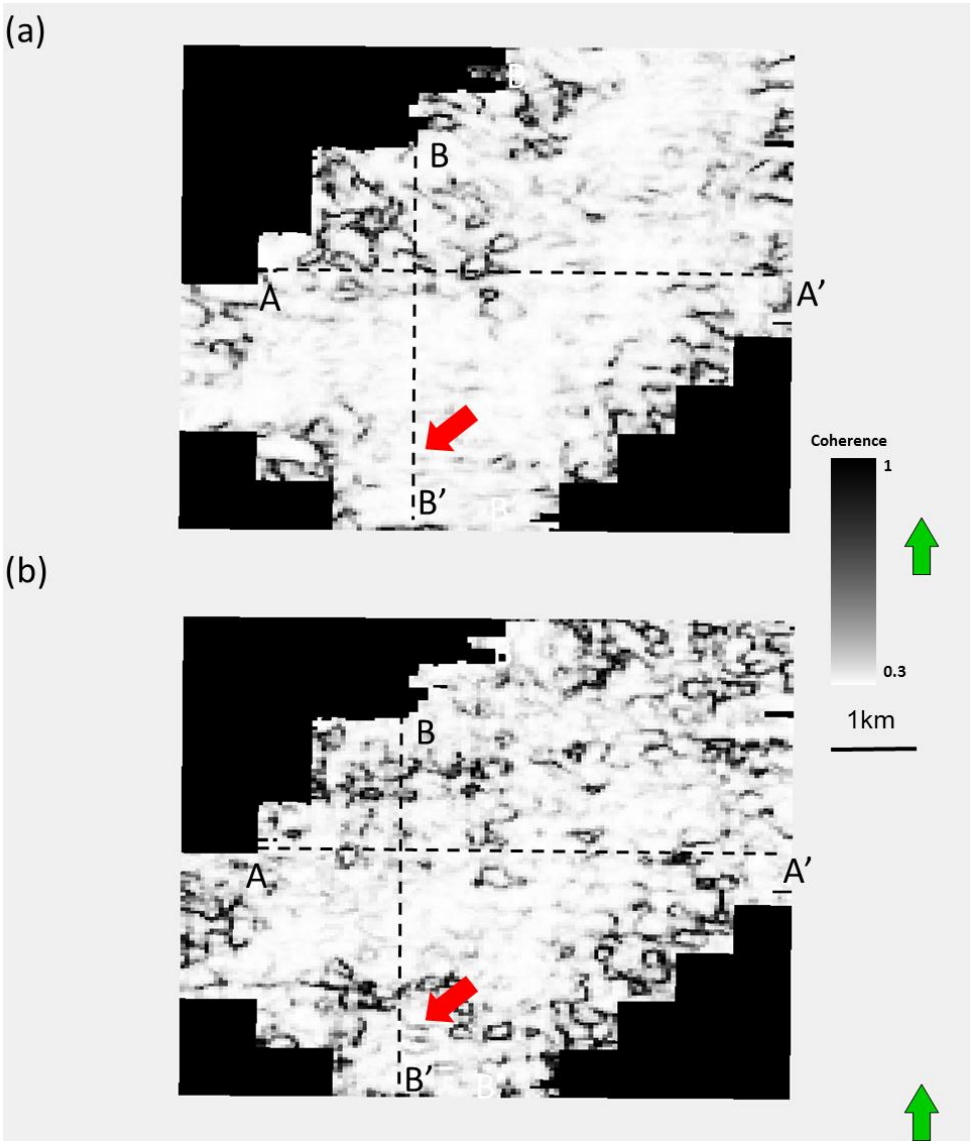
(a)
B
A
A'
B'
Coherence
1
0.3
(b)
B
A
A'
B'
1km

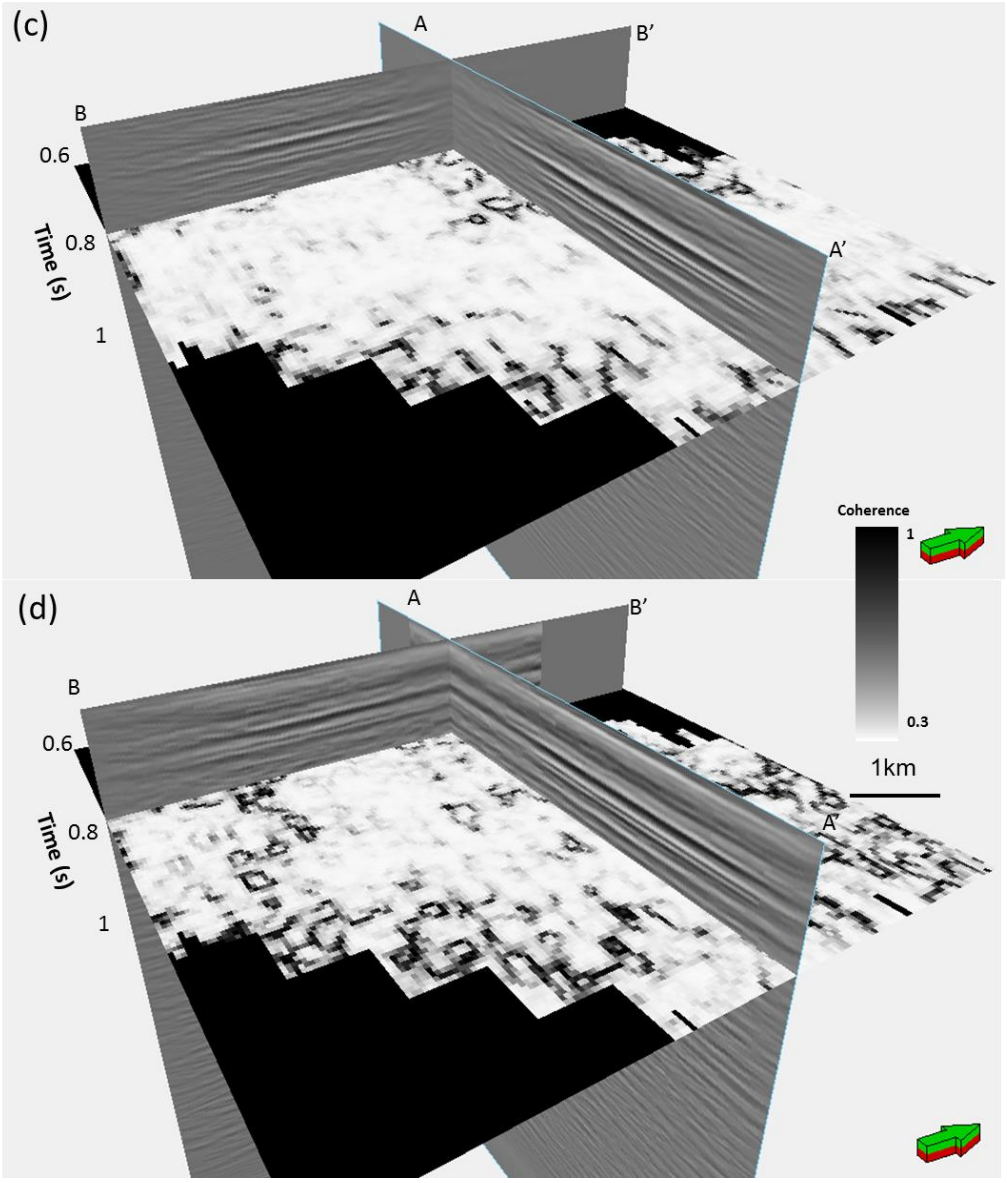

Figure 3.18. Time slices at t=0.8 s at the approximate Mississippian level through coherence volumes computed from migrated data (a) before and (b) after 5D interpolation, the same time slice (c) before and (d) after 5D interpolation showing the relation vertical time slice shown in the previous picture. The E-W acquisition footprint is reduced. Red arrows denote karst collapse features not seen prior to interpolating indicating diffraction and properly of the section.

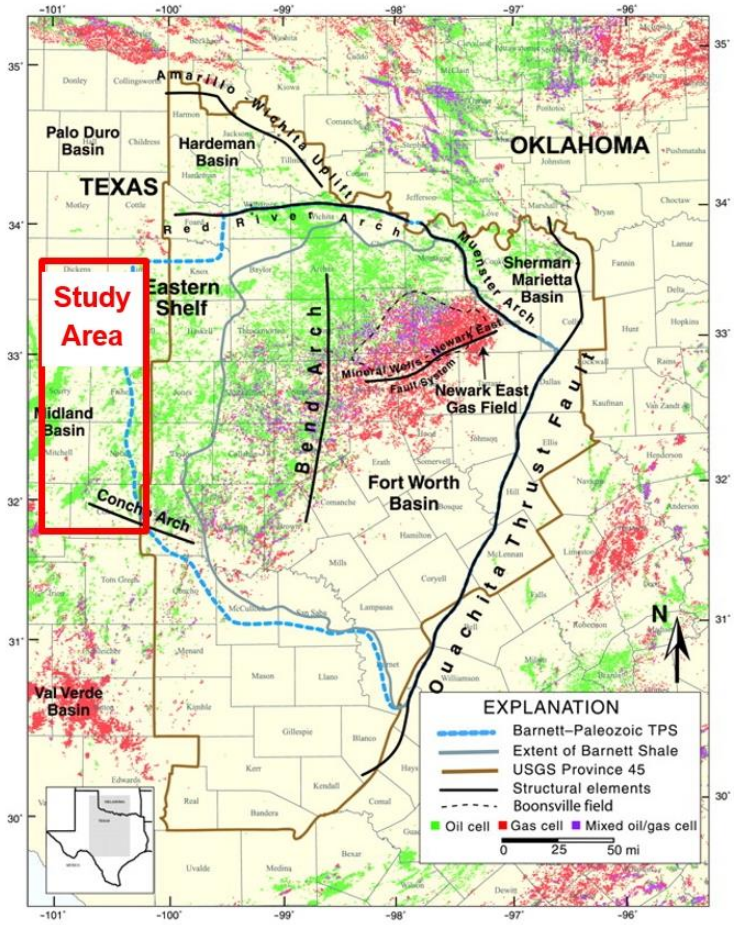

Figure 3.19. USGS map of Fort Worth Basin. The Mississippi lime study area is highlighted by the red box.

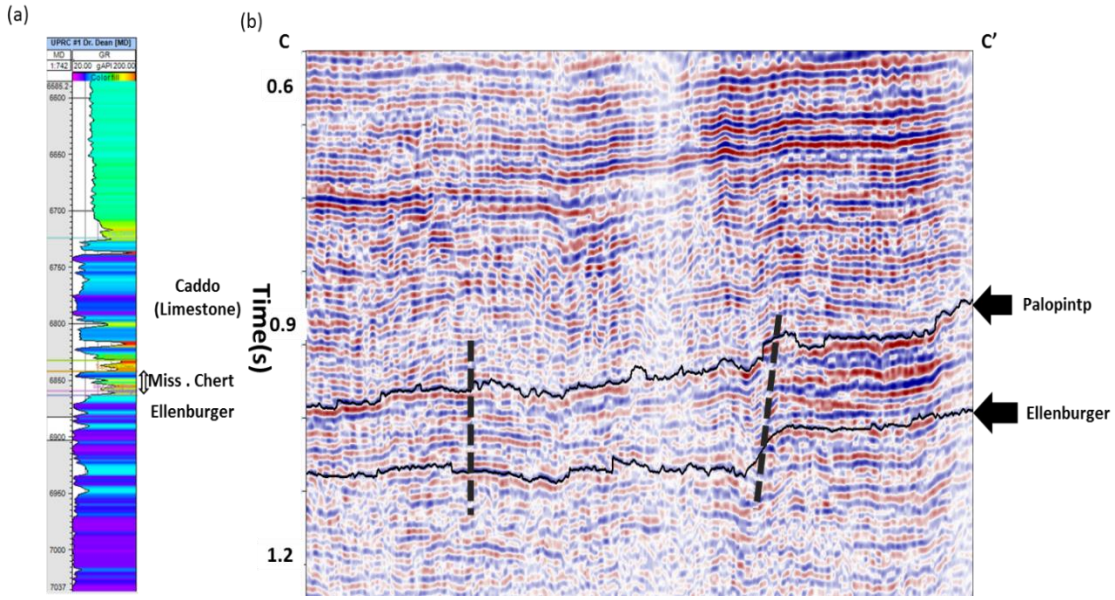

Figure 3.20. (a) A typical log from our survey. (b) A vertical slice through CC' (Figure 3.14), the dash black lines show faults system, black arrows show Palopintp and Ellenburger horizons.

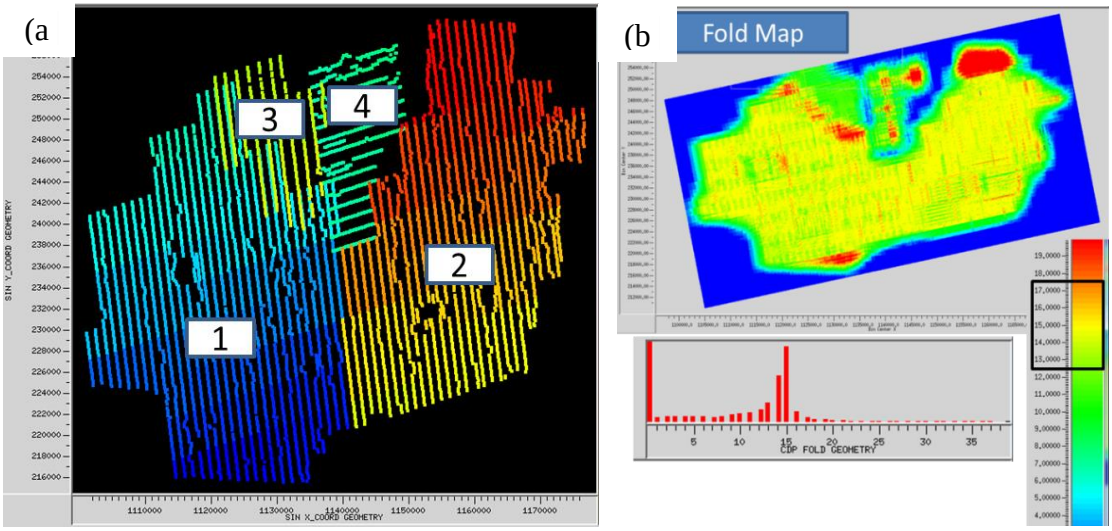

Figure 3.21. (a) Shot lines of the four merged surveys, indicated by number. (b) Corresponding fold map.

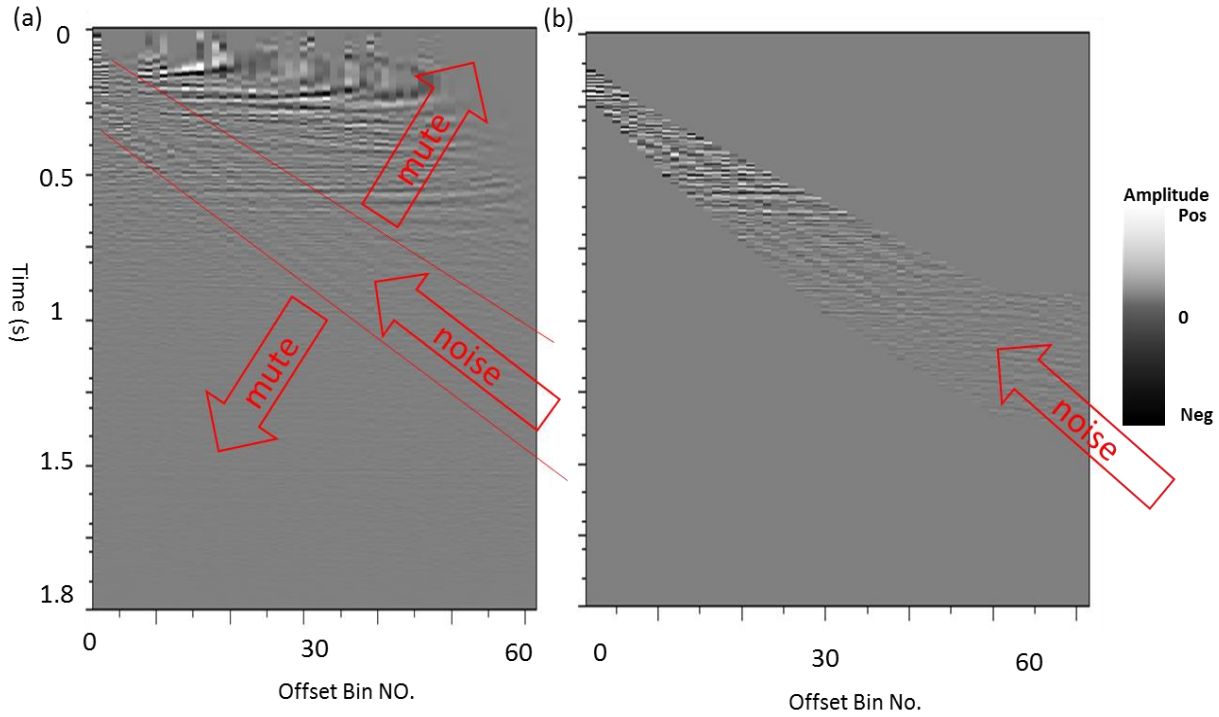

Figure 3.22. (a) A representative prestack migrated gathers contaminated by noise. (b) The same gather after muting to retain the noise. Note that migrated reflections within this noise cone are also retained and will be demigrated in the next figure.

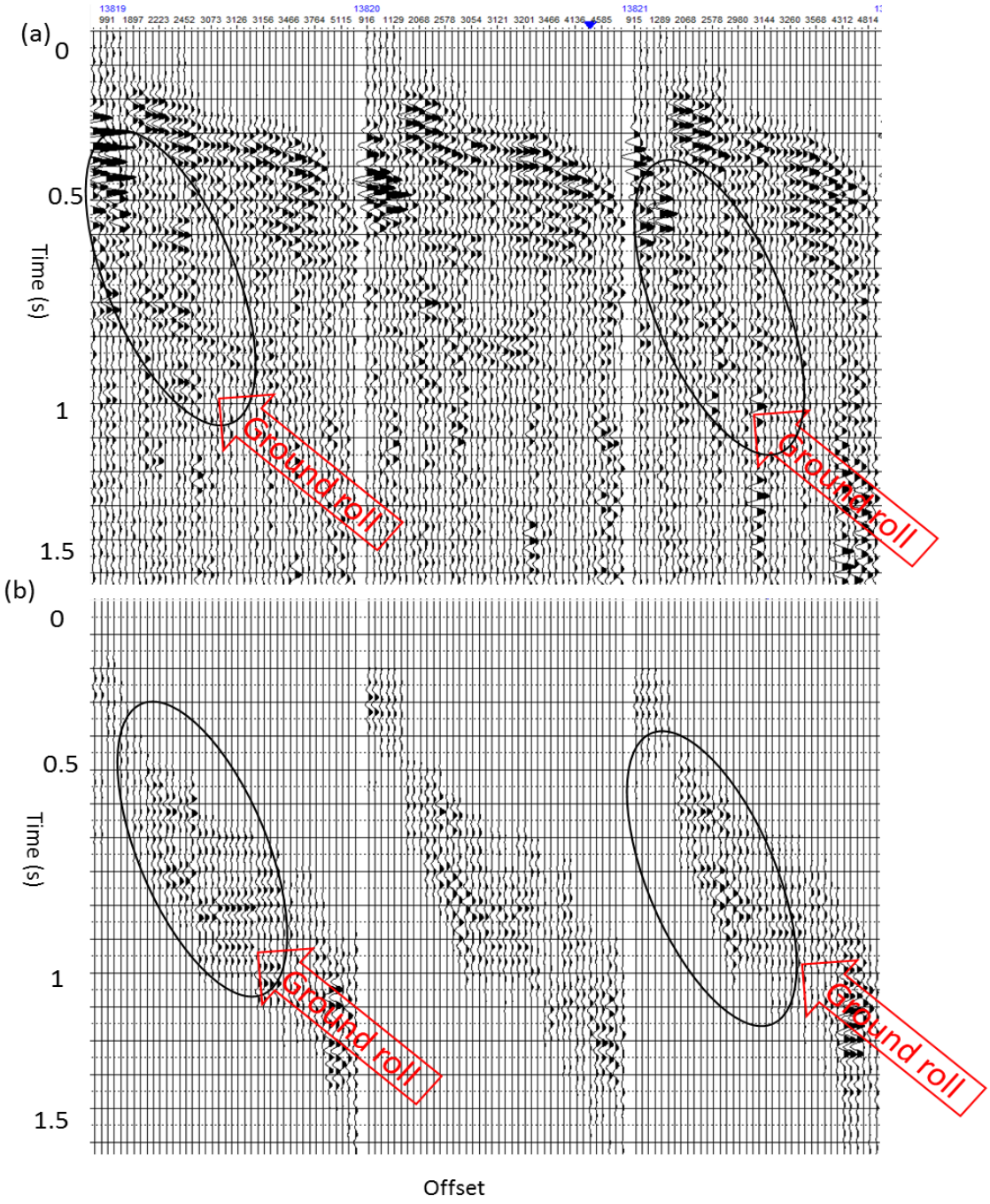

Figure 3.23. (a) Reconstructed gathers from demigration of the unmuted prestack data, and (b) the muted gathers targeting the noise events shown in Figure 2.11. indicate what we now interpret to the groundroll noise.

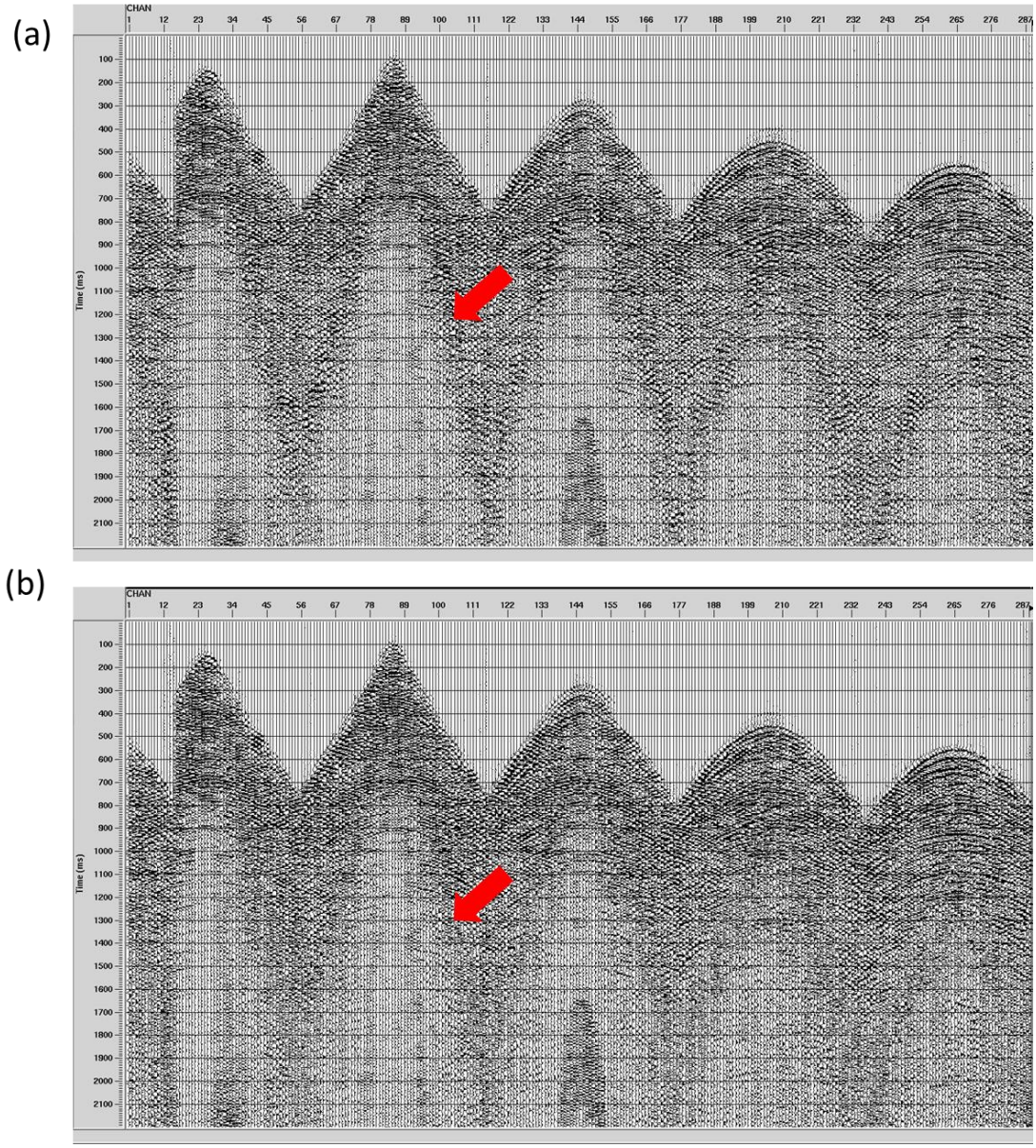

Figure 3.24. A representative shot gather measured on six receivers lines (a) showing strong aliased groundroll, (b) after groundroll suppression. (Verma 2014).

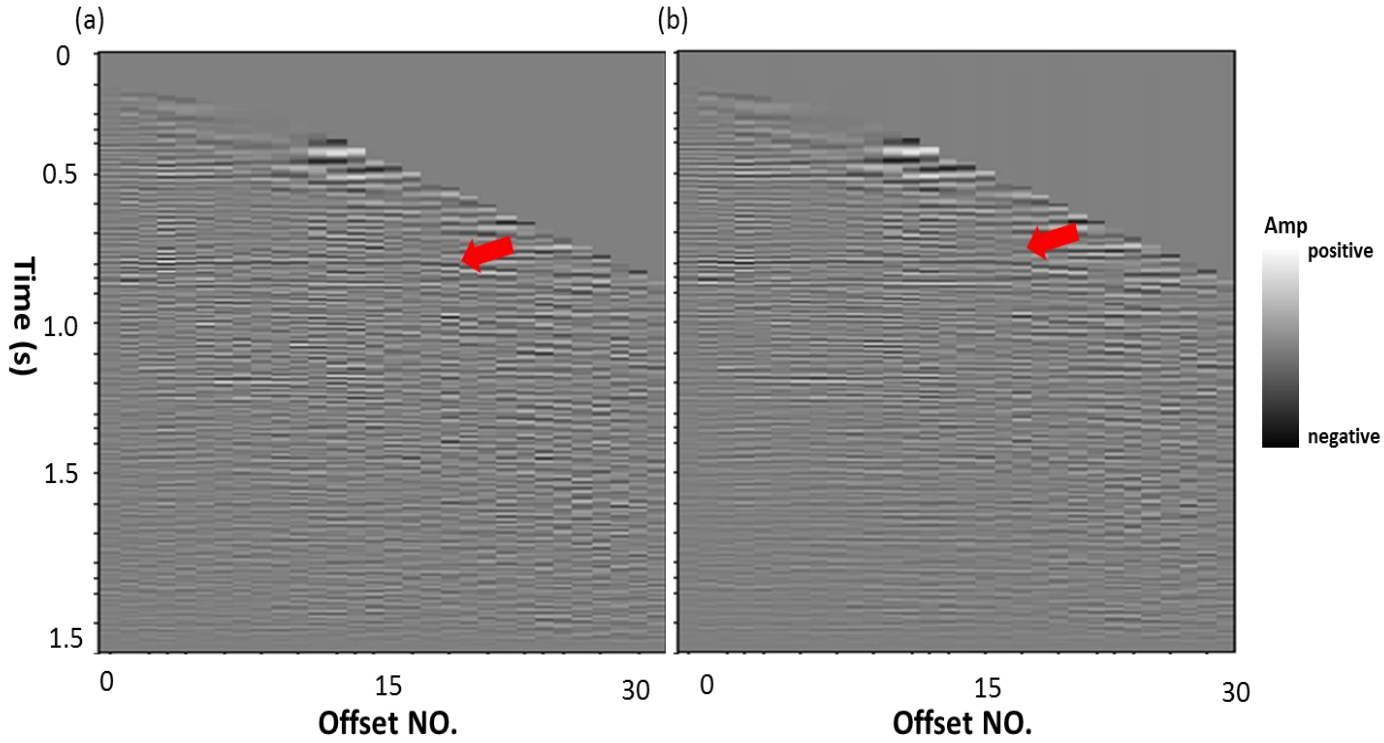

Figure 3.25. A representative prestack migrated gathers after (a) groundroll suppression, (b) after prestack structural oriented filter applied. Red arrows denotes the same reflection events, note less noise contamination after prestack SOF applied.

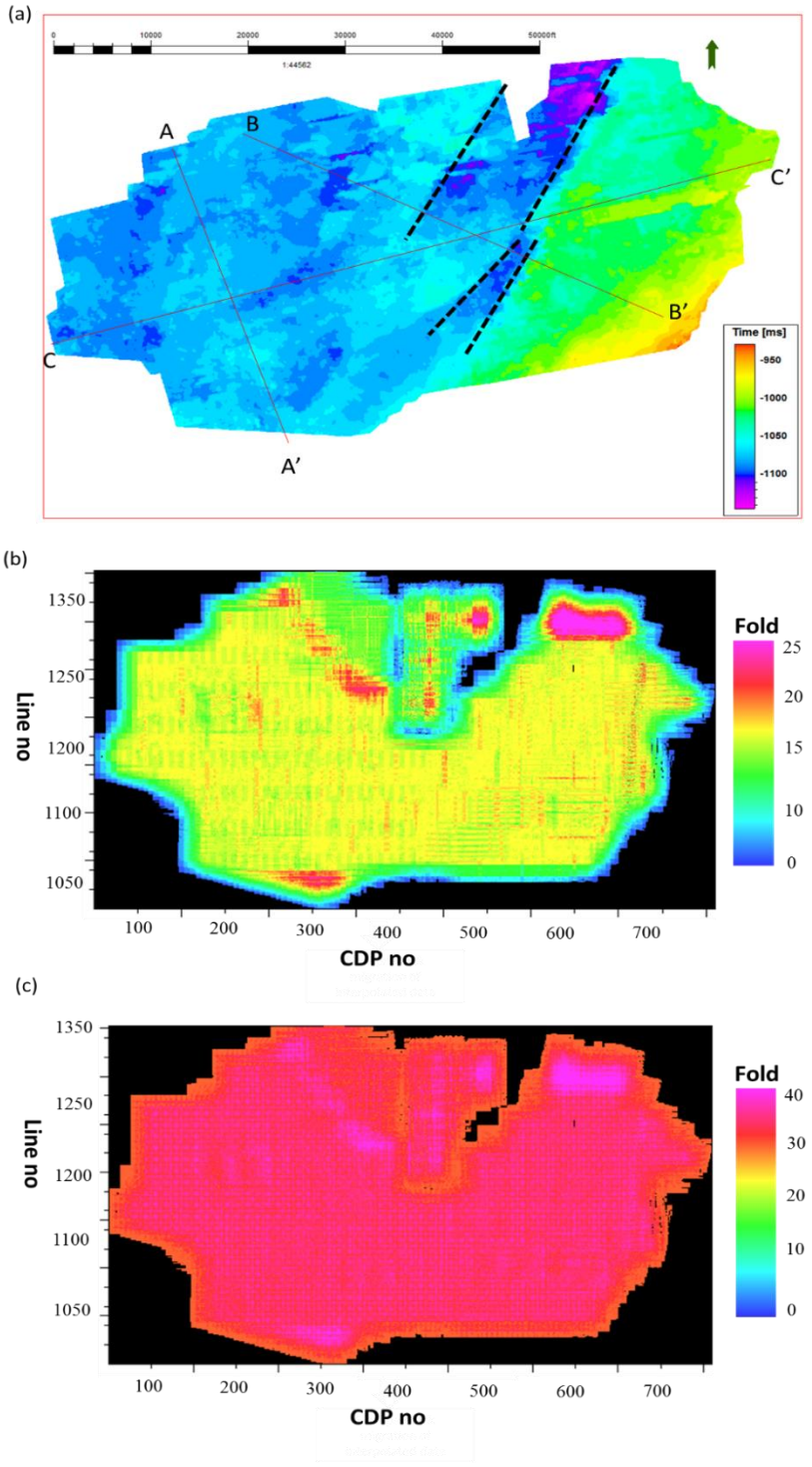

Figure 3.26. (a) Time structure map of the top Ellenburger Limestone, the dashed lines denote main faults system. (b) Fold map before 5D interpolation, (c) Fold map after 5D interpolation through PLSM.

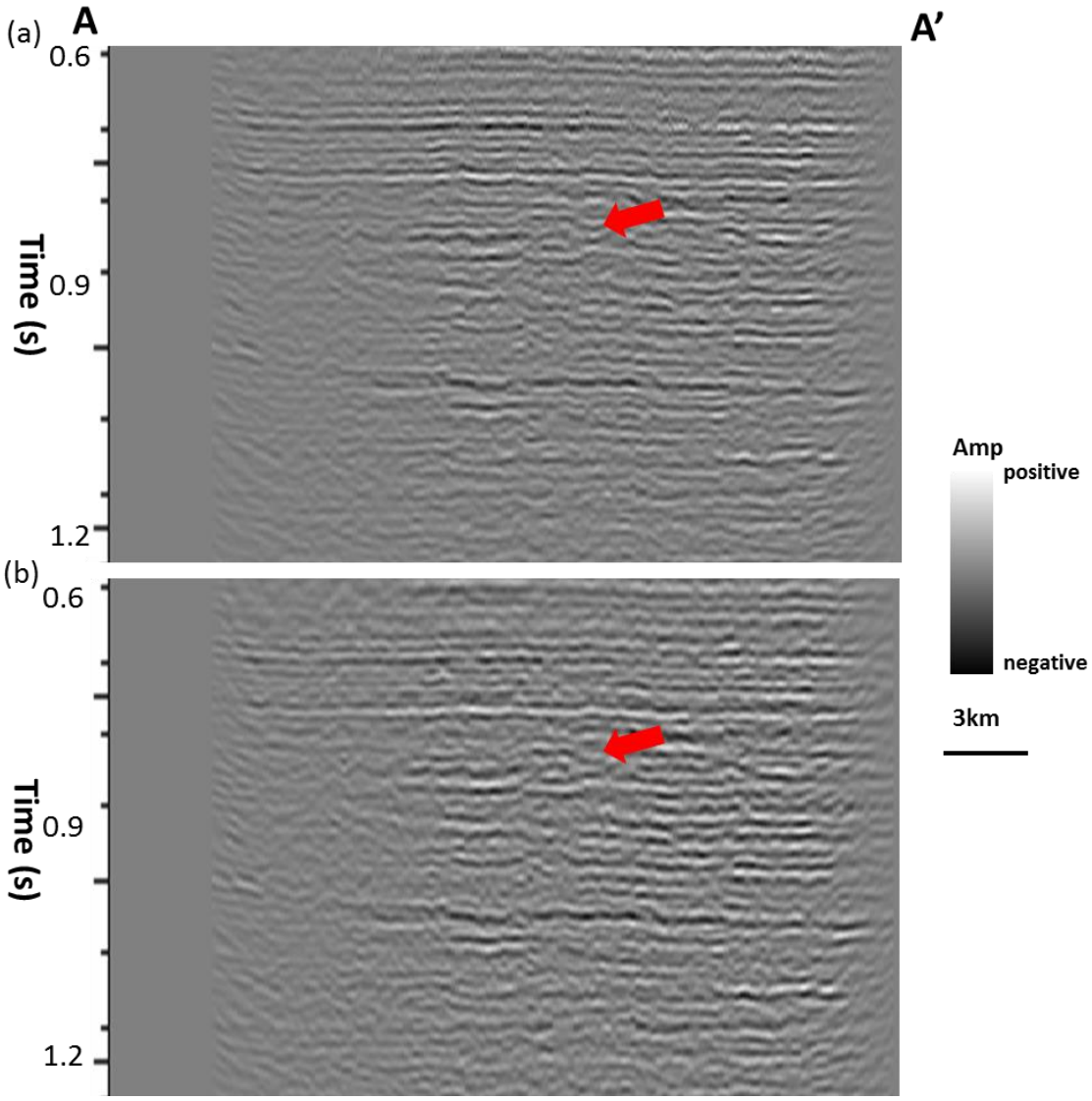
(a)
A
A'
0.6
Time (s)
0.9
1.2
(b)
0.6
Time (s)
0.9
1.2
Amp
positive
negative
3km

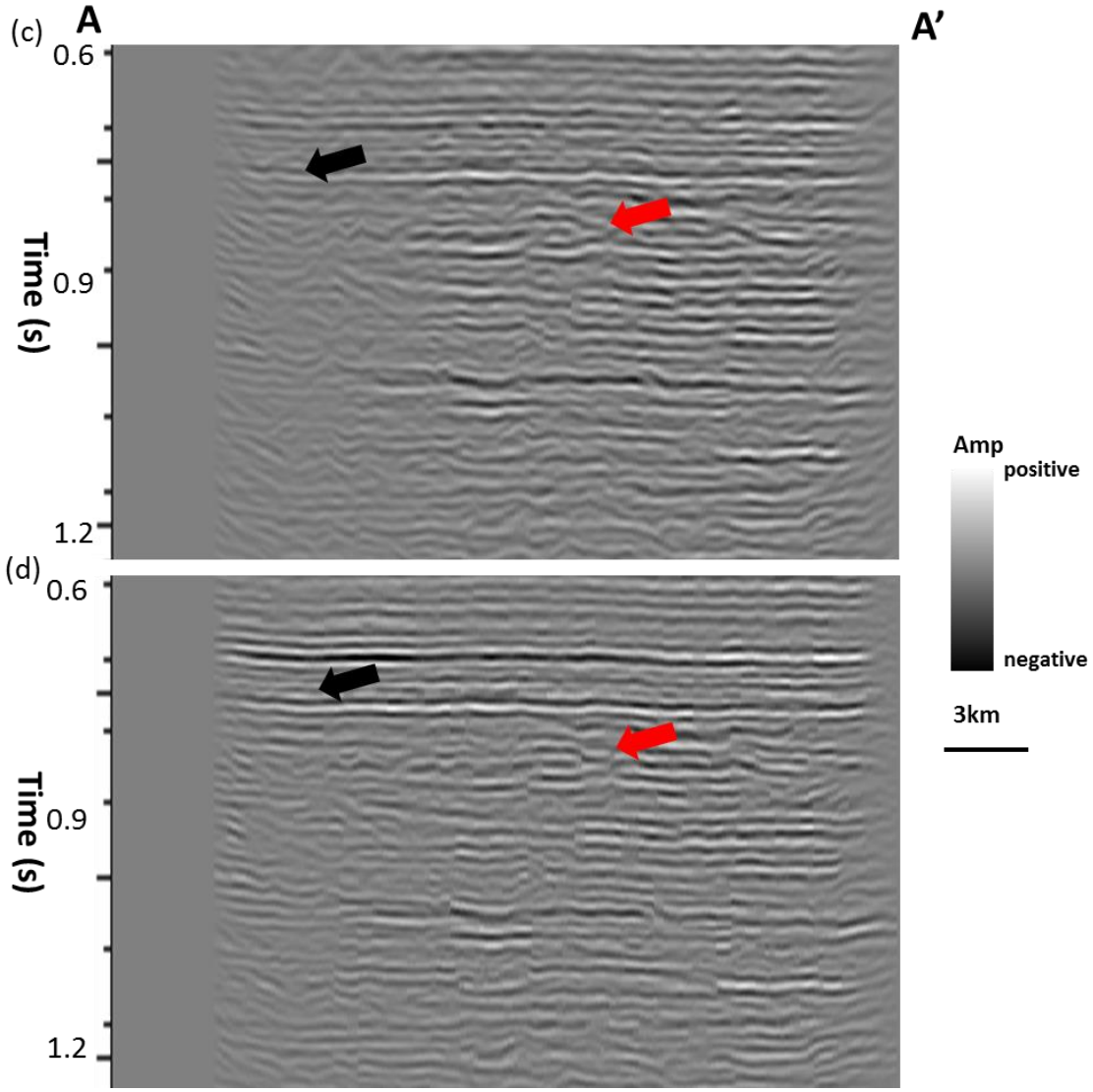

Figure 3.27. Vertical slice through seismic amplitude along profiles AA' as shown in Figure 3.15a: (a) using conventional migration, and after (b) groundroll suppression, and (c) after SOF applied, (d) 5D interpolation through PSLM. Red arrows show better continuity after 5D interpolation applied, and black arrows shows better amplitude balance.

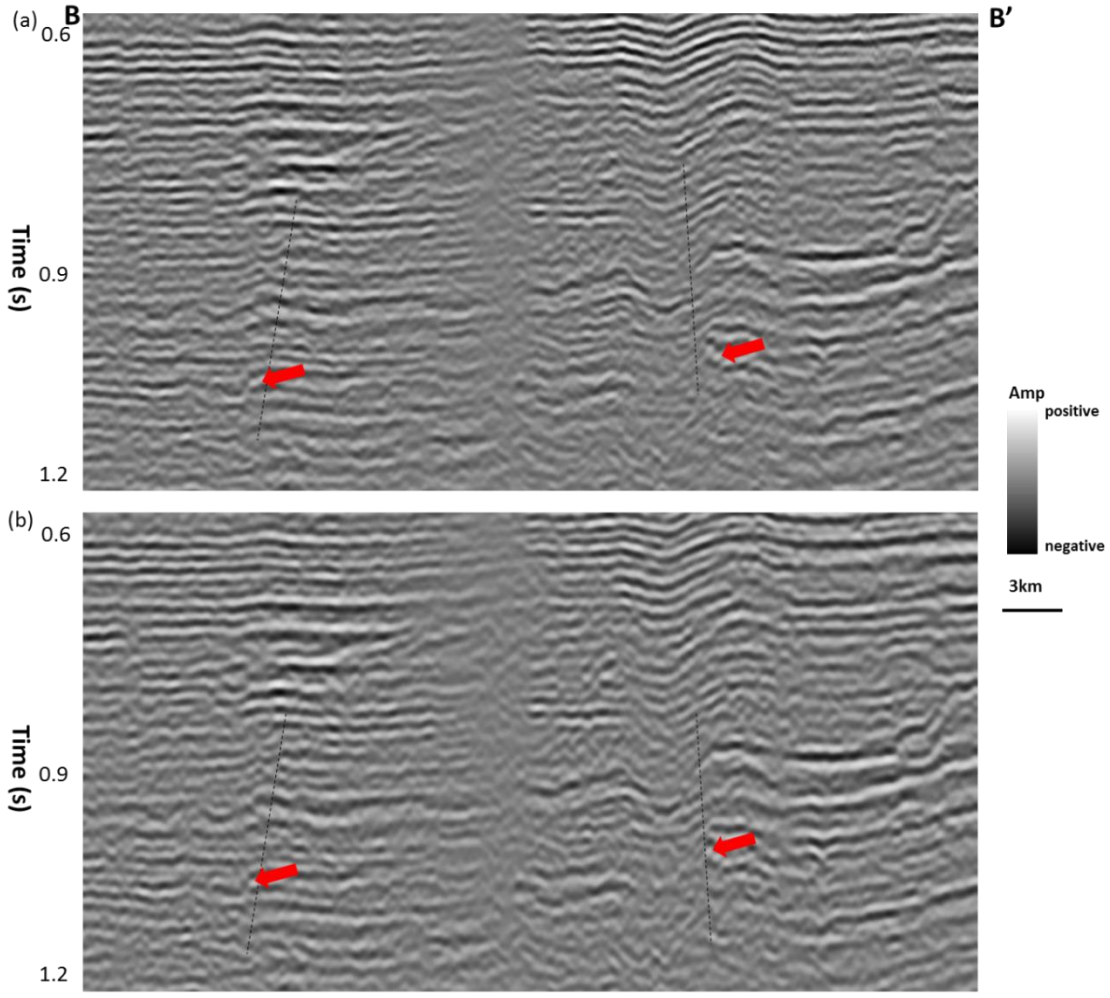
(a)
B
B'
0.6
Time (s)
0.9
1.2
(b)
0.6
Time (s)
0.9
1.2
Amp
positive
negative
3km

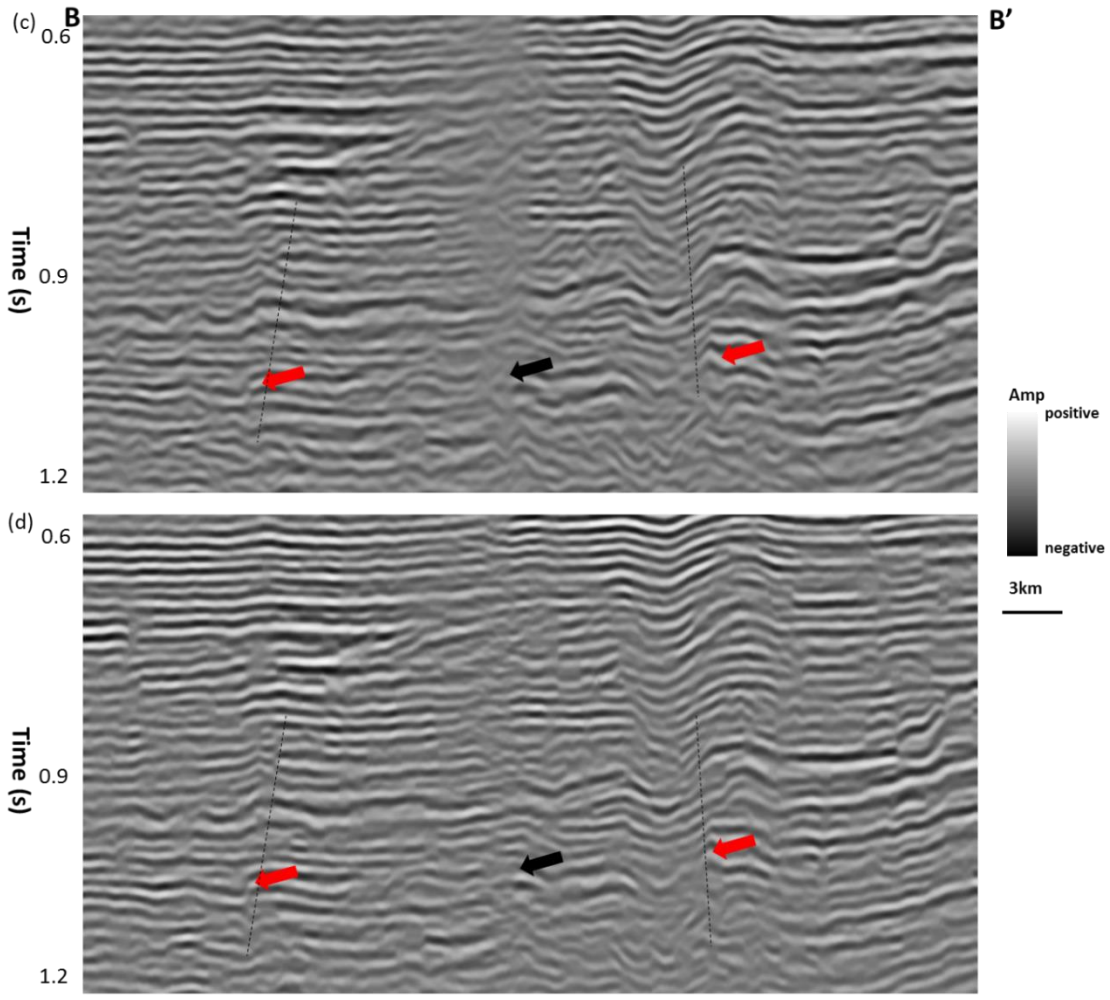

Figure 3.28. Vertical slice through seismic amplitude along profiles BB' as shown in Figure 3.15: (a) using conventional migration, and after (b) groundroll suppression, and (c) after SOF applied, (d) 5D interpolation through PSLM.

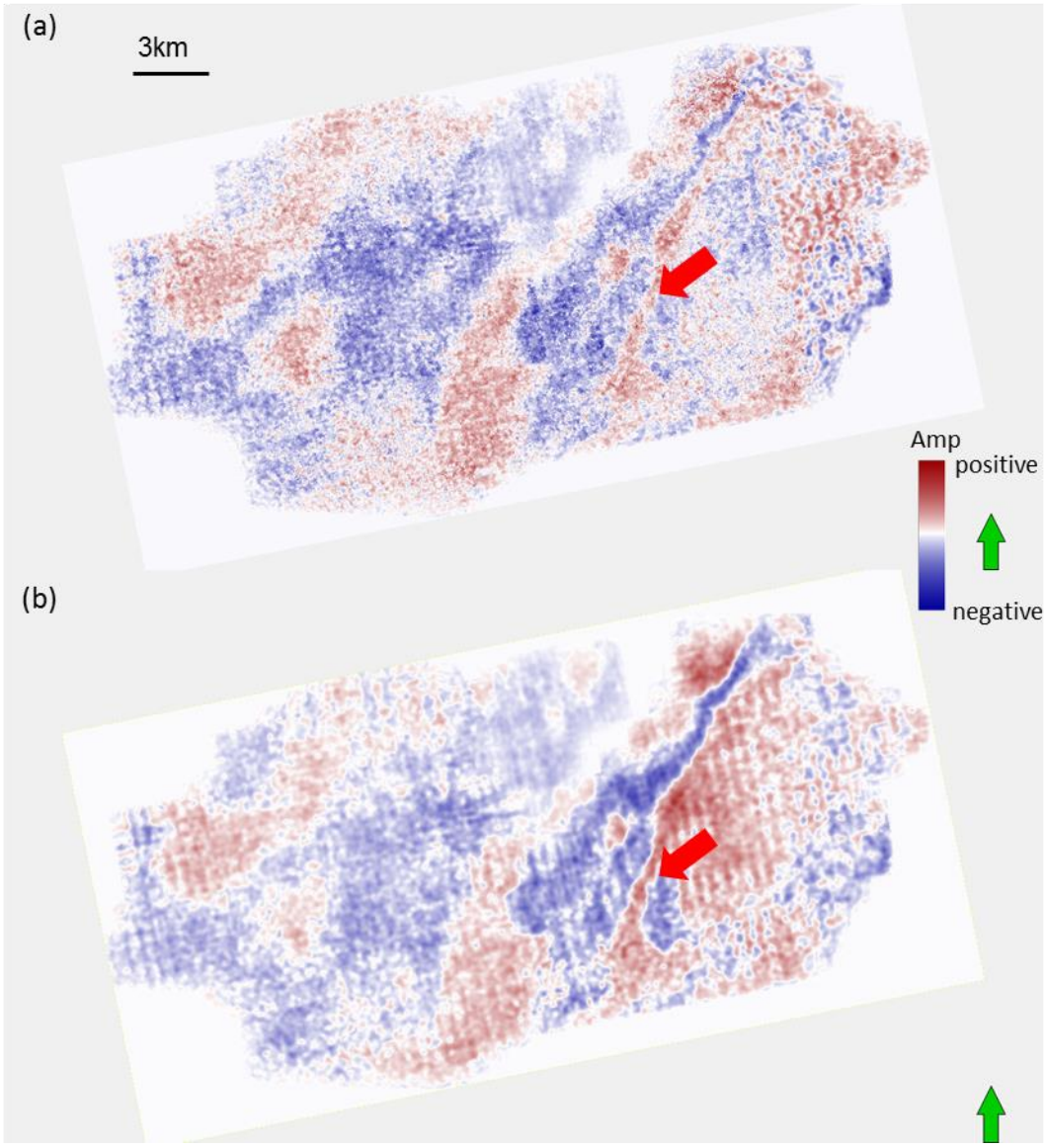
(a)
3km
Amp
positive
negative
(b)

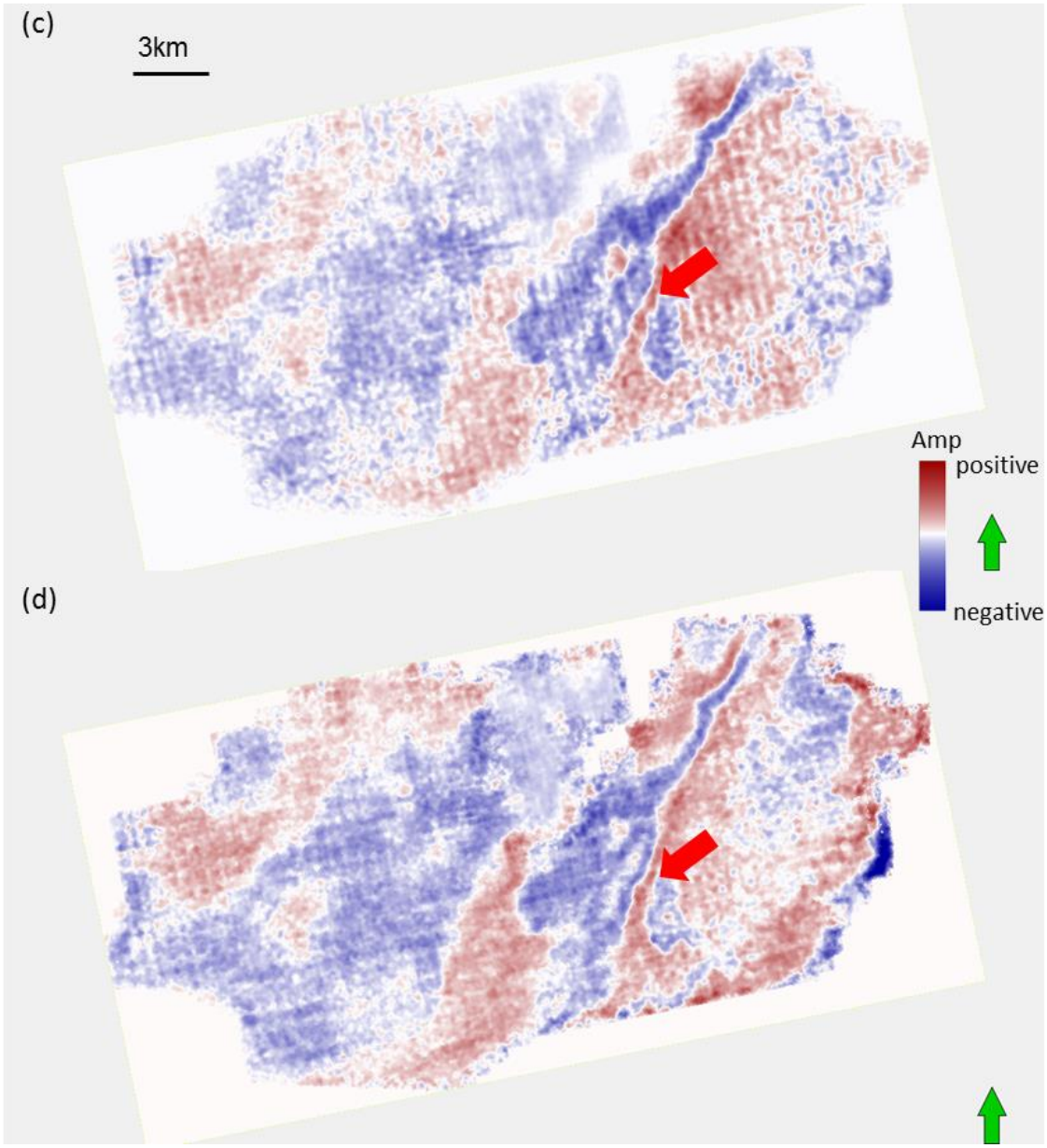

Figure 3.29. Time slice at 0.62 s through stacked seismic volume using (a) conventional migration, and after (b) groundroll suppression, and (c) after SOF applied, (d) 5D interpolation through PSLM. Red block arrows indicate faults system.

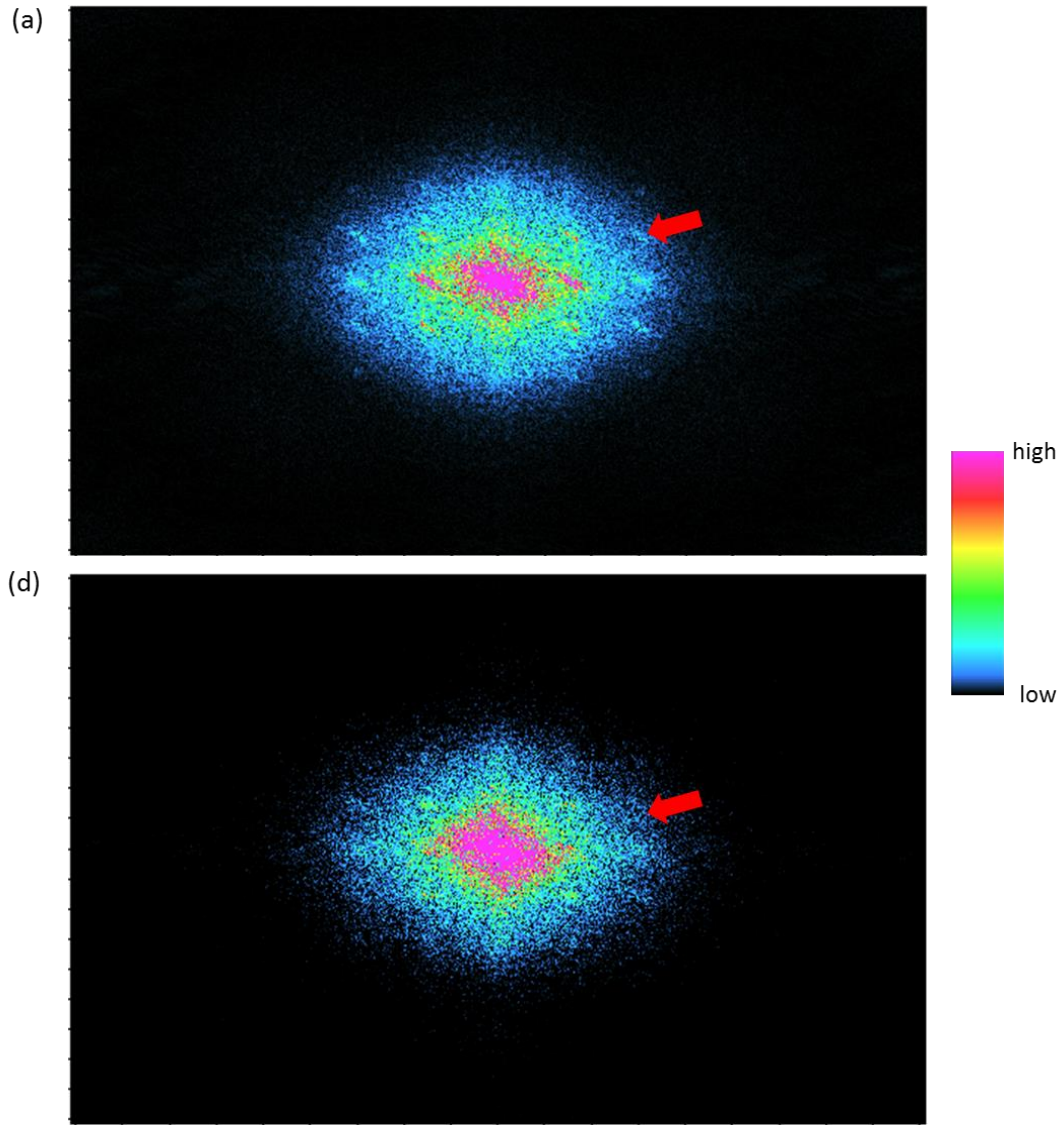

Figure 3.30. Time slice at 0.62 s in kx-ky domain through stacked seismic volume using (a) after SOF applied, (b) 5D interpolation through PSLM.

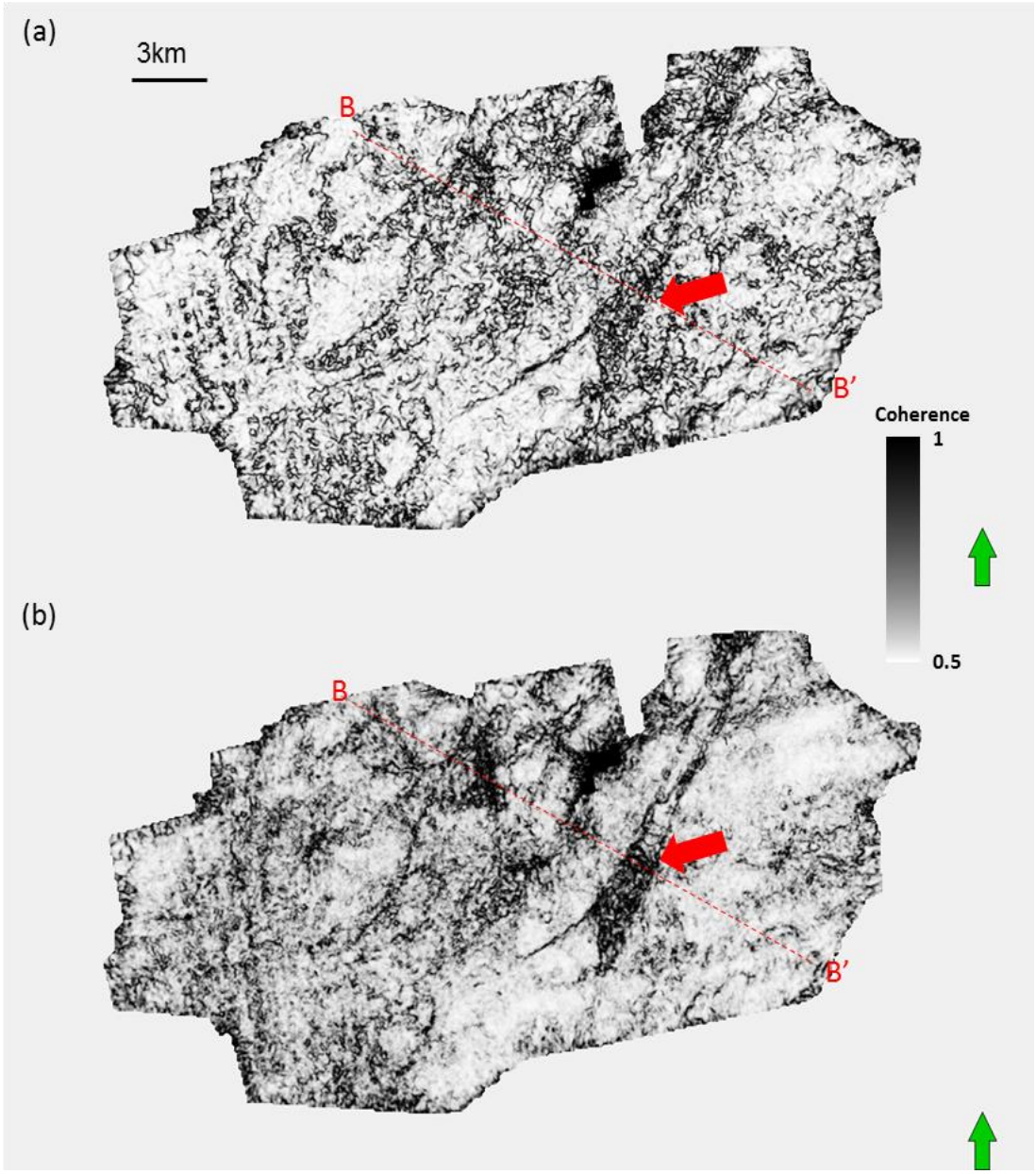
(a)
3km
B
B'
Coherence
1
0.5
(b)
B
B'

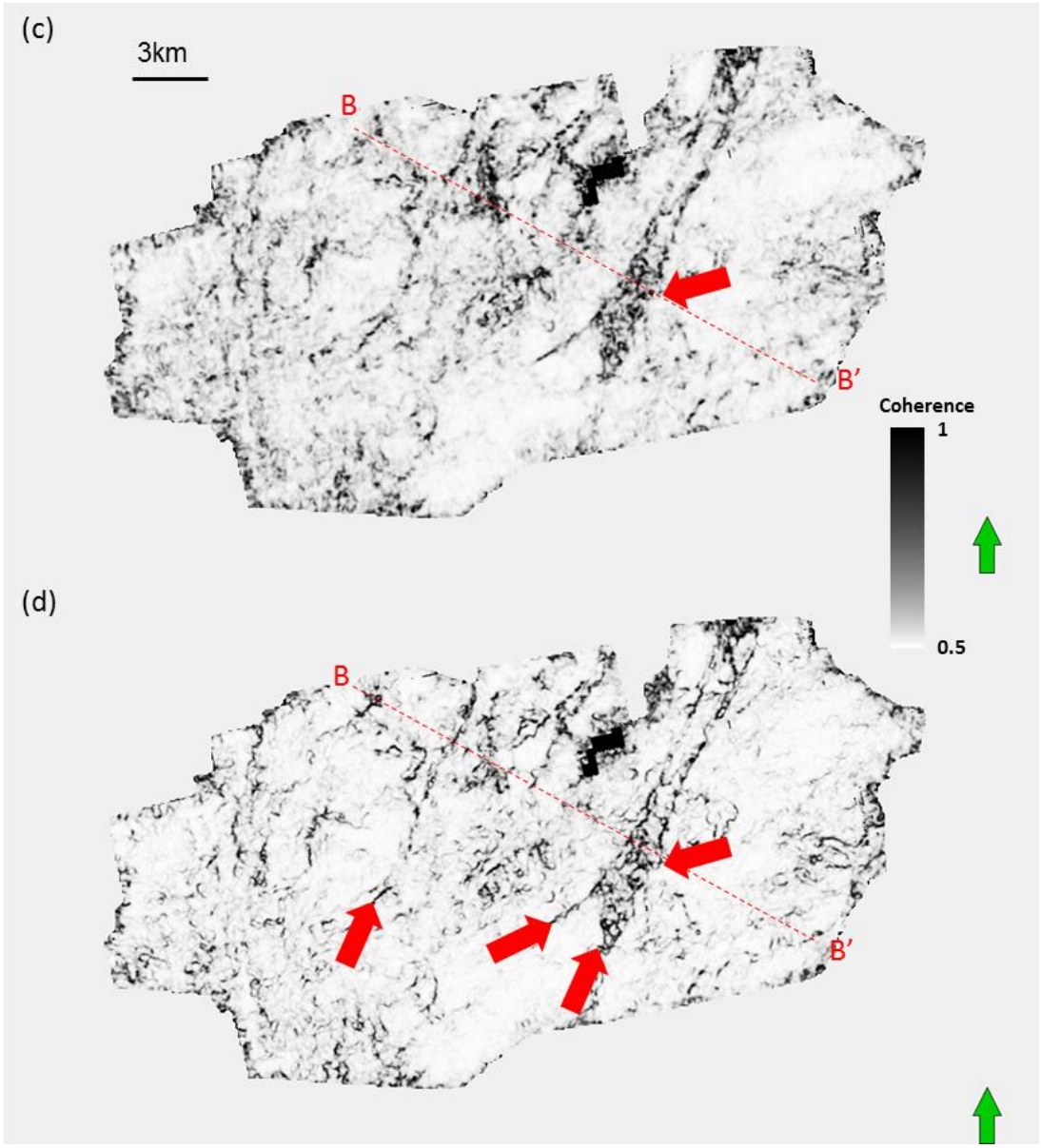

Figure 3.31. Horizon slices along the Ellenburger Limestone through energy ratio similarity volumes computed from seismic amplitude (a) conventional migration, and after (b) groundroll suppression, and (c) after SOF applied, (d) 5D interpolation. Red block arrows indicate faults system.

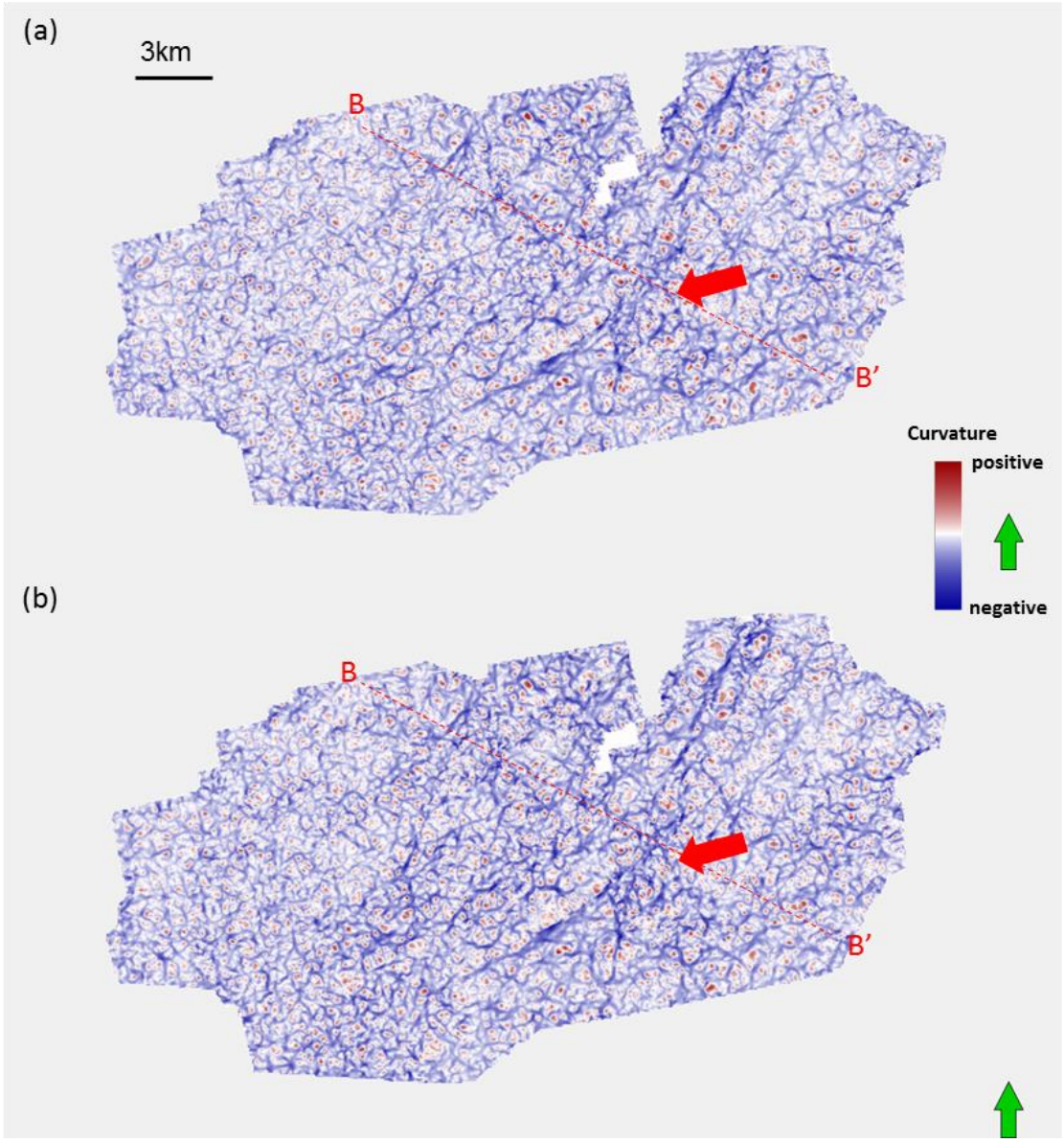
(a)
3km
B
B'
Curvature
positive
negative
(b)
B
B'

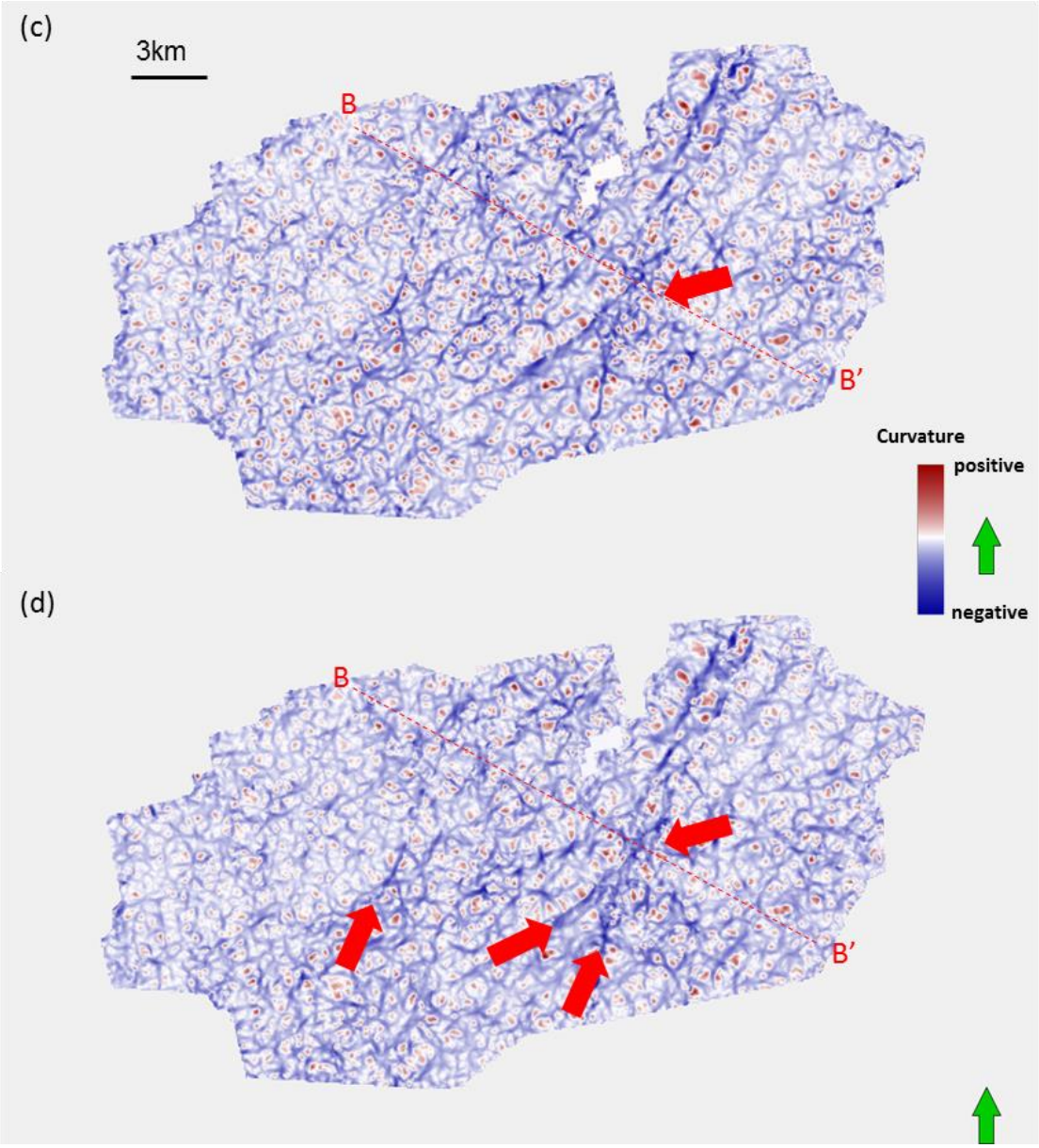

Figure 3.32. Horizon slices along the Ellenburger Limestone through most negative curvature volumes computed from seismic amplitude (a) conventional migration, and after (b) groundroll suppression, and (c) after SOF applied, (d) 5D interpolation through PSLM. Red block arrows indicate faults system.

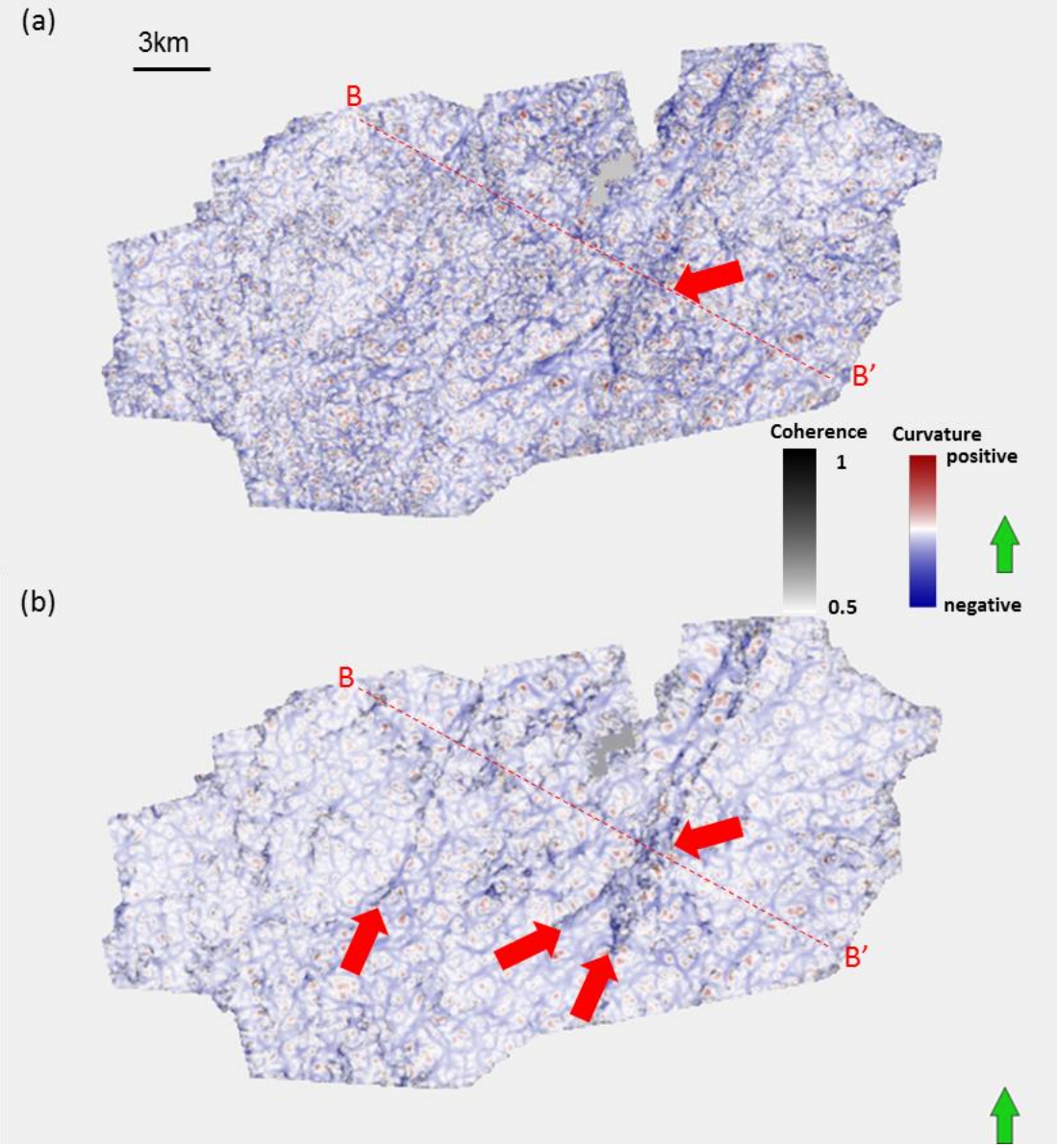

Figure 3.33. Horizon slices along the Ellenburger Limestone through most negative curvature co-rendered with coherence attribute computed from stacked seismic volume from (a) conventional migration, and after (b) groundroll suppression and 5D interpolation through PSLM. Red block arrows indicate faults system.

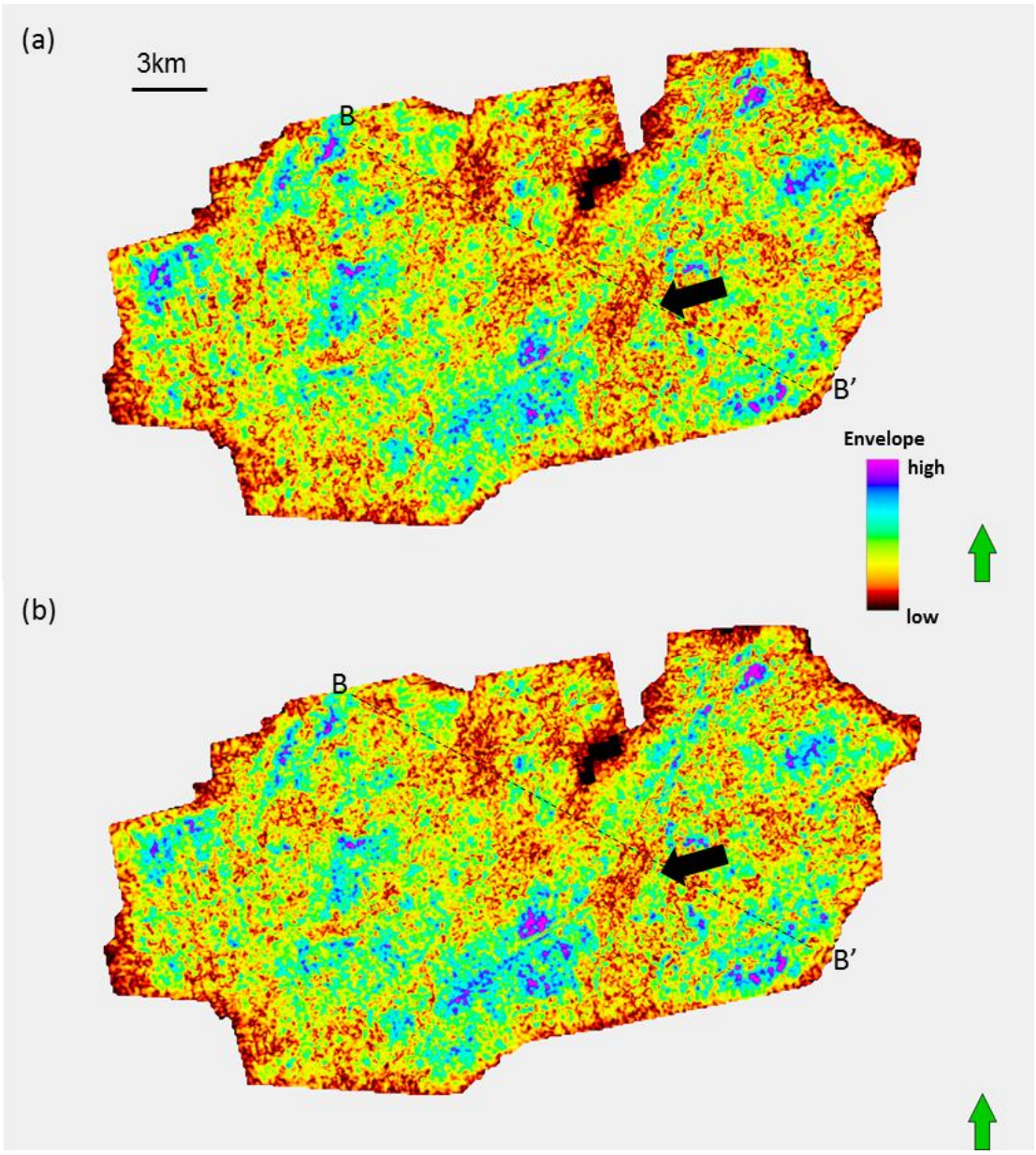
(a)
3km
B
B'
Envelope
high
low
(b)
B
B'

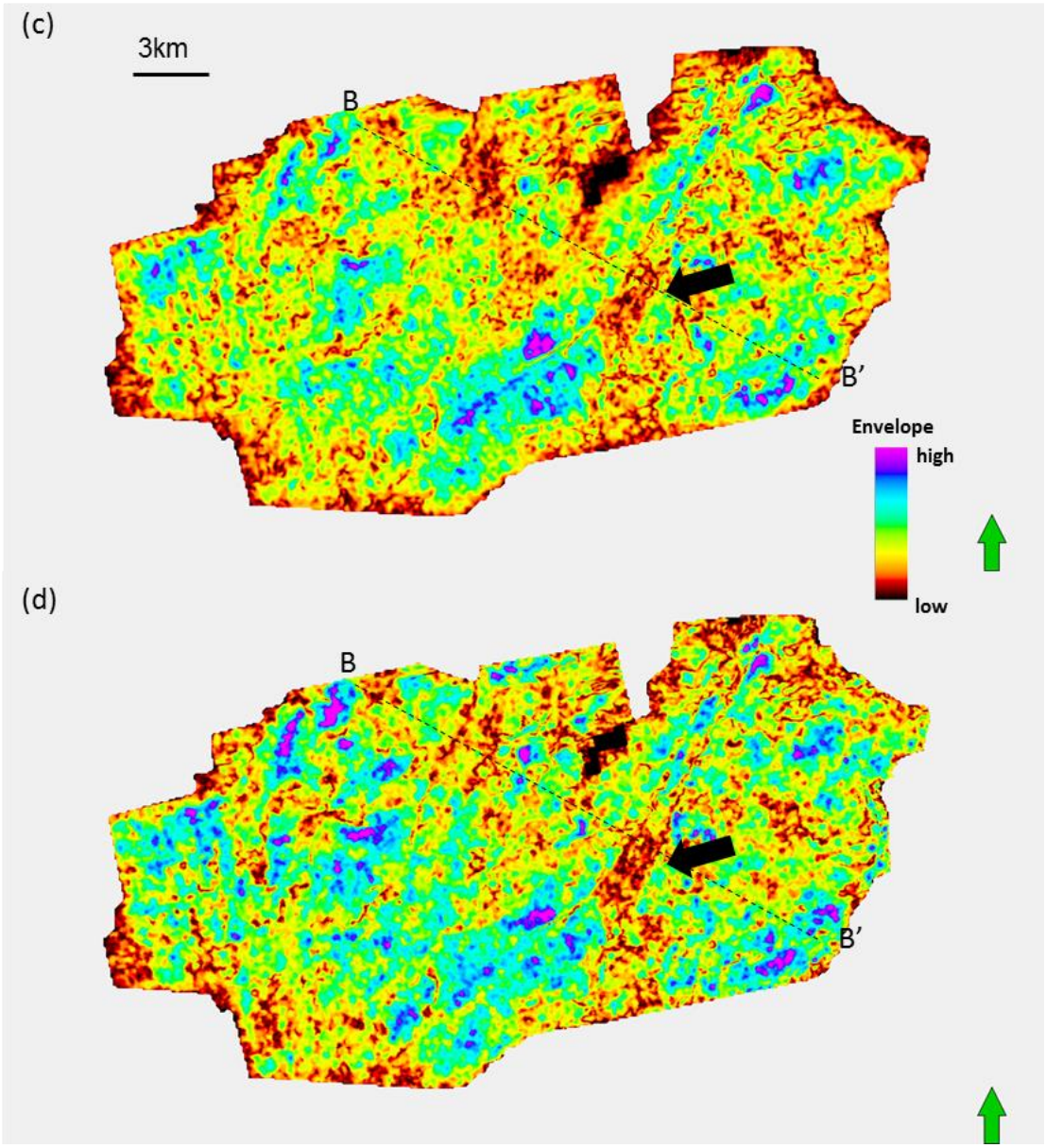

Figure 3.34. Horizon slices along the Ellenburger Limestone through envelope computed from stacked seismic volume from (a) conventional migration, and after (b) groundroll suppression and 5D interpolation through PSLM. Red block arrows indicate faults system.

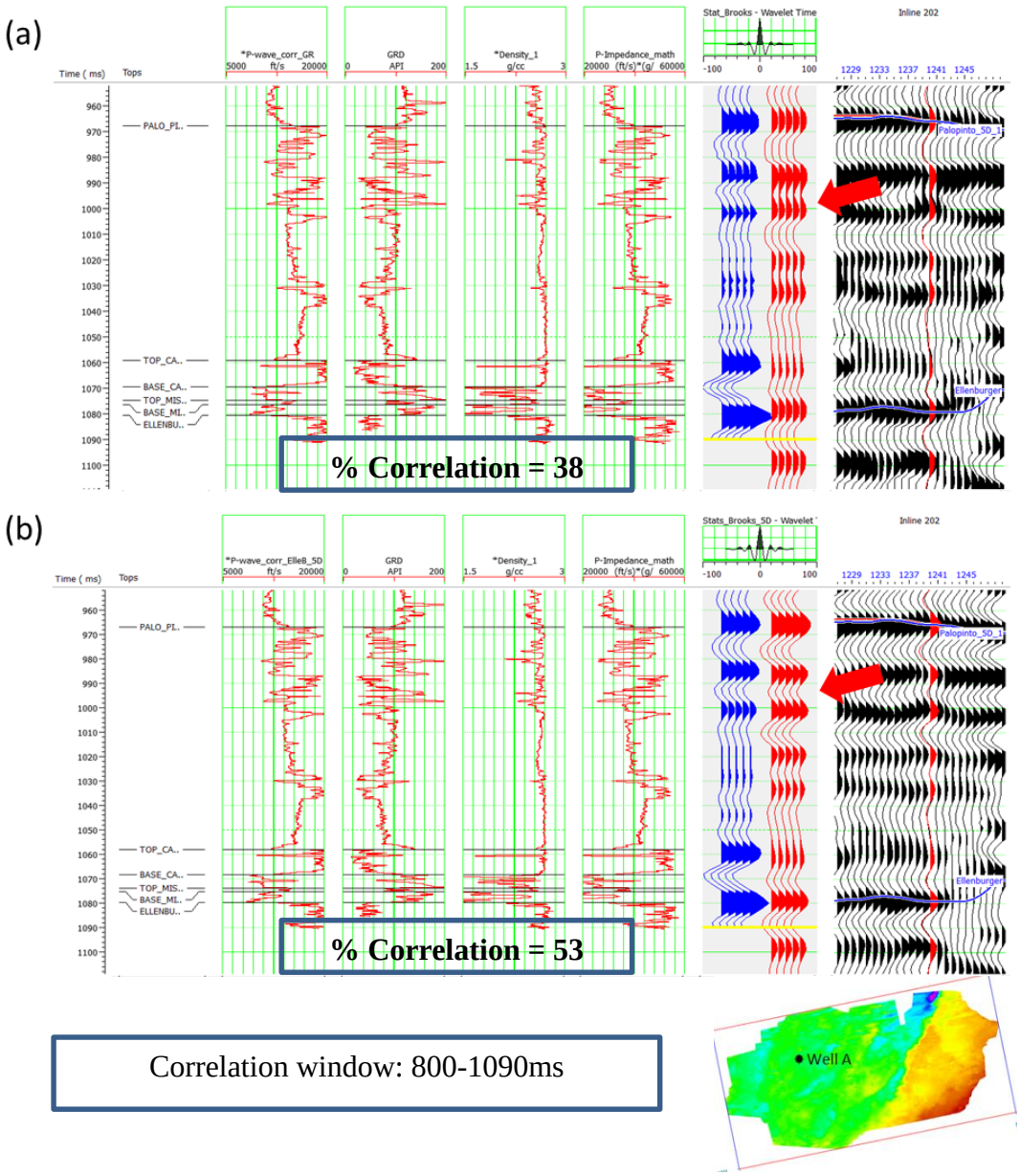

Figure 3.35. Well to seismic tie on well indicated illustrated in the map, (a) before 5D interpolation, and (b) after 5D interpolation. You can observe the red arrow, the well synthetic shows two reflectors and the seismic after 5D interpolation has better resolved the two reflectors.

REFERENCES

Abma, R., and N. Kabir, 2006, 3D interpolation of irregular data with a POCS algorithm: Geophysics, **71**, E91–E97.

Cansler, J. R., 2000, Paleogeomorphology of the sub-Pennsylvanian unconformity on the Arbuckle Group (Cambrian-Lower Ordovician): Master's thesis, University of Kansas, Lawrence, 123.

Chopra, S., and K.J., Marfurt, 2013, Preconditioning seismic data with 5D interpolation for computing geometric attributes, SEG Houston 2013 Annual Meeting, 1368-1373.

Guo, S., B., Zhang, A., Vargas, K. J., Marfurt, 2012, Noise suppression using preconditioned least-squares prestack time migration: Application to the Mississippian Limestone, SEG Las Vegas 2012 Annual Meeting, 3831-3836.

Liu, B. and M.D., Sacchi, 2004, Minimum weighted norm interpolation of seismic records, Geophysics, **69**, 1560–1568.

Stein, J. S., S. Boyer, K. Hellman, and J. Weigant, 2010, Application of POCS interpolation to exploration: 80th Annual International Meeting, SEG, Expanded Abstracts, 2013–2016.

Nissen, S. E., Carr, T. R., K.J., Marfurt,, and Sullivan, E. C., 2009, Using 3-D seismic volumetric curvature attributes to identify fracture trends in a depleted Mississippian carbonate reservoir: Implications for assessing candidates for CO2 sequestration: AAPG Studies in Geology, **59**, 297–319.

Wojslaw, R., J. A. Stein, and T. Langston, 2012, 5D semblance-based interpolator in exploration-theory and practice: 74th EAGE Conference and Exhibition,

Extended Abstracts, B024.

Verma, S., S. Guo, and K.J., Marfurt., 2014, Prestack suppression of high frequency groundroll using a 3D multiwindow KL filter: Application to a legacy Mississippi Lime survey: 80th Annual International Meeting, SEG, Expanded abstract.

Xu, S., Y. Zhang, and G. Lambare, 2005, Recovering densely and regularly sampled 5D seismic data for current land acquisition: 67th EAGE Conference and Exhibition, Extended Abstracts, W024.

Chapter 4: Vector correlation of AVAz anisotropy and curvature for prediction of natural fractures in Barnett Shale survey

Shiguang Guo[1], Bo Zhang[1], Tengfei Lin[1] and Kurt J. Marfurt[1]

[1]The University of Oklahoma, ConocoPhillips School of Geology and Geophysics

ABSTRACT

The Barnett Shale of the Fort Worth Basin serves as the source rock for most of the reservoirs in North Texas. Being more accurately called a "mudstone" since it has a very high quartz and calcite content, the Barnett Shale was one of the first economic shale gas plays. Although the high TOC content of the Barnett Shale makes it a good source rock, its permeability is negligible such that hydraulic fracturing is required to provide pathways for fluid flow. Successful well placement and completion require an accurate estimate of the orientation and magnitude of horizontal stress (and natural fractures, if any). In our study, the main objective is to predicate the azimuth and density of natural fractures of the Barnett Shale. We migrate our seismic data by a new binning approach that sort the data by azimuth. By comparing the azimuthal seismic amplitude variation, we compute the AVAz anisotropy for prediction of natural fractures. Strike-slip faults are known to modify the subsurface stress regime. I map faults using both the strike and magnitude of the most-positive and most-negative principal curvatures and visually correlate them to AVAz. There is high correlation between positive curvature and the AVAz magnitude anisotropy density. A vector correlation between AVAz and the two curvatures show that a perpendicular relationship between the most negative curvature and AVAz vectors.

INTRODUCTION

The Fort Worth is the first modern shale gas play. Although the high TOC property of Barnett Shale makes it a good source rock, it is also characterized by low permeability. Hydraulic fracturing is required to provide pathways for fluid flow and increase the permeability. Optimal well placement and orientation requires mapping the density and azimuth of natural fractures and stress field can be essential for the production and horizontal hydraulic fracture choice.

Significant research has been devoted to the seismic response of fractures. Direct measures of fractures include Amplitude vs. Azimuth (AVAz) (Rueger, 1998; Goodway et al., 2007b) and Velocity vs. Azimuth (VVAz) (Sicking et al., 2007; Roende et al., 2008; Jenner, 2001; Hunt et al., 2011). For P-waves, the reflectivity response parallel to fracture strike is close to that of the unfractured rock matrix (Rueger and Tsvankin, 1995; Rueger, 1997). Lynn et al. (1999) found that AVO gradients measured normal to fractures at known water wet zones were near zero or negative.

Geometric attributes such as coherence and curvature have also been used for fracture prediction (Chopra et al., 2007; Thompson et al. 2010, Guo, 2010). Hunt et al. (2011) found a combination of AVAz and curvature best correlated to fractures estimated by horizontal image logs and microseismic measurements. Guo et al. (2010) visually correlated VVAz to the strike of the most negative curvature and found a strong rotation between the two across the strike-slip Mineral Wells fault at the Ellenburger dolomite level beneath the Barnett Shale.

In this study, we extend the work by Guo et al. (2010) through the use of AVAz and a more quantitative correlation. I migrate our seismic data into different azimuths

using a binning approach described by Perez and Marfurt (2008). This binning allows us to identify the image contribution from out-of-the-plane steeply dipping reflectors, fractures, and faults. Next we compute the amplitude variance for a suite of azimuthally limited prestack gathers, followed by fitting sinusoids to the eight azimuthally limited volumes and an AVAz analysis. I then compute the vector correlation between AVAz anisotropy and geometric curvature calculated from the fully stacked volumes.

METHODOLOGY

Perez and Marfurt (2008) proposed a new azimuthal binning approach to Kirchhoff prestack migration that sorts output by the azimuth of the average travel path from surface midpoint to subsurface image point, rather than the azimuth between source and receiver (Figure 4.1). This new binning allows us to identify the image contribution from out-of-the-plane steeply dipping reflectors, fractures, and faults. Then we migrate our gathers for 8 azimuths as Figure 4.2 shown.

Rueger's (1995) equation for AVAz can be written as

$$R(\theta,\varphi) = A + [B^{iso} + B^{ani}cos^2(\varphi - \varphi_0)]sin^2\theta \quad (4\text{-}1)$$

where $R(\theta,\varphi)$ is the reflectivity at angle of incidence θ and azimuth φ,

$$B^{iso} = \frac{1}{2}\frac{\Delta V_p}{V_p} - 2\left(\frac{V_s}{V_p}\right)^2\left(\frac{\Delta\rho}{\rho}\right) - 4\left(\frac{V_s}{V_p}\right)\frac{V_s}{V_s}^2, \text{ and} \quad (4\text{-}2)$$

$$B^{ani} = \frac{1}{2}[\Delta\partial^{(v)} + 2\left(\frac{2V_s}{V_p}\right)\Delta\gamma^{(v)}] \quad (4\text{-}3)$$

In the absence of anisotropy, $B_{aniso}=0$, equation (4-1) reverts to the well-known AVO equations in terms of slope B_{iso}, and intercept A. Note the azimuthal anisotropy plays an

increasingly stronger role at larger angles of incidence, as indicated by the $\sin^2\theta$ coefficient.

I improve slightly upon the robustness of normal AVAz analysis by computing the principal component of $R(\theta,\varphi)$ within a 20 ms window, which is equivalent to Karhunen-Loeve filtering the azimuthal gathers. Otherwise, we follow Zhang et al. (2011), and fit equation (4-1) to the azimuthally limited seismic amplitude, resulting in the magnitude of the minimum and maximum anisotropy and their strike, as well as an estimate of the fit quality (Figure 4.3).

Correlation of vectors

AVAz has a magnitude, B_{aniso}, and an azimuth, φ. The maximum curvature has a value k_{max}, and a strike, ψ_{max}. Both attributes are thus vectors. Outcrop work by White (2012) and others shows a strong correlation between curvature and natural fractures. We also know that natural fractures give rise to anisotropy. Guo et al. (2009) found correlations between curvature and velocity anisotropy, with anisotropy south and north of the Mineral Wells strike slip fault to be parallel and perpendicular to the fault, consistent with outcrop analogues and finite element models. Such an explicitly relationship suggest the use of vector correlation, between anisotropy, **a**, and curvature **c,** as shown in Figure 4.4.

Using vector arithmetic, we can compute the colinear component

$$\mathbf{a} \cdot \mathbf{c} = a_x c_x + a_y c_y \,, \tag{4-4}$$

and the orthogonal component of correlation:

$$\mathbf{a} \times \mathbf{c} = a_x c_y - a_y c_x \,. \tag{4-5}$$

to construct components of a vector correlation, we define a J-trace analysis window (Figure 4.4) and compute

$$r_{\text{colinear}} = \frac{\sum_{j=1}^{J}(a_x^j c_x^j + a_y^j c_y^j)}{\left[\sum_{j=1}^{J}(a_x^j a_x^j + a_y^j a_y^j)\right]^{1/2}\left[\sum_{j=1}^{J}(c_x^j c_x^j + c_y^j c_y^j)\right]^{1/2}} \quad , \tag{4-6}$$

and

$$r_{\text{orthogonal}} = \frac{\sum_{j=1}^{J}(a_x^j c_y^j - a_y^j c_x^j)}{\left[\sum_{j=1}^{J}(a_x^j a_x^j + a_y^j a_y^j)\right]^{1/2}\left[\sum_{j=1}^{J}(c_x^j c_x^j + c_y^j c_y^j)\right]^{1/2}} \quad , \tag{4-7}$$

where

$$\|\mathbf{r}\| = (\mathrm{r}_{\text{colinear}}^2 + \mathrm{r}_{\text{orthogonal}}^2)^{1/2} \, , \tag{4-8}$$

And

$$\varphi = \arg(r) = ATAN(\mathrm{r}_{\text{orthogonal}}, \mathrm{r}_{\text{colinear}}) \, . \tag{4-9}$$

is referenced to the average curvature vector c

$$\underline{c}_{avg} = \frac{1}{j}\sum_{j=1}^{J} \underline{c}_j \tag{4-10}$$

APPLICATION

The Fort Worth Basin (FWB) is a shallow foreland basin, located in north Texas (Figure 4.6). The mostly dolomitic Ellenburger Group exhibits high porosity, joints, and karst features, is often a water-bearing formation that can destroy shallower gas production in the overlying Barnett shale reservoir through connectivity of either natural or induced fractures.

In the area of study, the Mississippian Barnett Shale was deposited directly over the eroded Viola limestone strata as shown in Figure 4.7, on a shelf or in a basin area marginal to the Ouachita geosyncline. The Barnett Shale sequence consists of alternating shallow marine limestone and black, organic rich shale. In the eastern side of the FWB,

the Barnett Shale can be subdivided into an upper and a lower interval interbedded by a dark limestone interval, known as the Forestburg Limestone. The Forestburg is absent to the south and west of this survey and is not an exploration target. However, it forms an effective fracture barrier to contain the induced hydraulic fractures in the gas wells. The presence of glauconite and phosphate material indicates slow deposition under reducing conditions (Aktepe, 2007).

A representative log through the Barnett shale in Figure 4.8a show that the lower Barnett shale is characterized by high gamma ray, low density and high P-wave velocity. Figure 4.8b shows a time structure map of the lower Barnett Shale. Red arrows denote two faults system. Figure 4.9 shows representative azimuthally limited prestack gathers of different azimuths, note the change in amplitude at different azimuths caused by anisotropy.

Figure 4.10 shows eight azimuthally limited stacked volumes. Note the stacked volumes at 112.5^o and 135^o show higher resolution than those at 22.5^o and 45^o around the fault zone. The azimuths 22.5^o and 45^o are approximately parallel to the strike of the fault, while azimuths 112.5^o and 135^o are perpendicular to the strike of the faults. More energy from the fault planes is measured at these two azimuths. In addition, the signal-to-noise ratio is better in stacked volume from 90^o and 135^o. Figure 4.11 shows time structure maps of top of the Lower Barnett Shale. Note the difference of structural pattern of top of lower Barnett Shale for different azimuths.

Figure 4.12 shows phantom horizon slices along the top of the lower Barnett Shale through coherence volumes for the different azimuths. Note faults systems are shown more clearly (red arrows) for azimuths 112.5^o and 135^o. There faults are poorly illuminated at shown from 45^o, 67.5 ^{o} and 90^o. Figure 4.13 shows horizon slices along the

top of the Lower Barnett Shale through most negative curvature k_2 about different azimuths. Faults lineaments are better focused at 112.5^o and 135^o, and smearing at 45^o, 67.5 ^{o} directions.

Figure 4.14 shows horizon slice through B_{aniso}, coherence and the most negative curvature k_2 on the top of the Lower Barnett Shale from the full stacked volume. Note the visual correlation between the most negative curvature and the B_{aniso}. In addition, it shows strong correlation between coherence and curvature through the corresponding horizon slice, suggesting there is structure associated fractures and faults.

Figure 4.15a shows a horizon slice along the top of the Lower Barnett Shale through k_2 curvature co-rendered with coherence. Red arrows denote faults lineaments. Note there is high correlation between most negative curvature and high coherence from faults zone. Figure 4.15b shows the corresponding horizon slice though B_{aniso} co-rendered with most negative curvature k_2. There is a strong visual correlation between fault and high anisotropy intensity, which suggests structural fractures may give rise to anisotropy. Figure 4.15c shows the corresponding horizon slice though anisotropy intensity B_{aniso} co-rendered with coherence, strong visual correlation between high coherence and high anisotropy intensity along the faults.

Figure 4.16a shows a horizon slice along the top of the Lower Barnett Shale through normalized EUR co-rendered with coherence, Figure 4.16b shows normalized EUR co-rendered with most negative curvature. Note the high gas production from Barnett Shale is correlated to high fracture density which is characterized by most negative curvature and high coherence.

Figure 4.17a displays strike of most negative curvature modulated by its value. Note the fault is most characterized by purple and red colors, which indicate a NE strike. Figure 4.17b shows a corresponding horizon slice through strike of AVAz, anisotropy ψ_{aniso} modulated by its value B_{aniso}, note that structural faults zone is highlighted by high anisotropy intensity and yellow and light blue color, indicating NW direction as red arrows shown. Figure 4.17c shows same horizon through strike of correlation of new vector attributes modulated by its value. Note that the faults is characterized by purple color as shown by red arrows around fault zone in figure 4.17c, which is new vector attribute, so perpendicular relationship between the most negative curvature and AVAz vector is found.

CONCLUSIONS

The azimuthal anisotropy can be used as a powerful tool to map azimuth and density of fractures in Barnett Shale, different imaging of structural faults lineaments show different focusing for different azimuth directions which caused by anisotropy. High correlation between AVAz anisotropy high and most negative curvature highlight structural faults lineaments. AVAz anisotropy azimuth shows EW and SE orientation of maximum stress field.

In addition, perpendicular relationship between the most negative curvature and AVAz vector is found. We demonstrate that high gas production from mainly Barnett Shale is correlated to high fracture density related to anisotropy high. We can conclude that natural fractures associated with faults is characterized by anisotropy high, which can provide us reliable insight for the fracturing choice along horizontal well.

ACKONWLEDGEMENTS

The authors would like to thank Devon Energy for funding, encouragement, and the authorization to publish this work, and sponsors of Attribute-Assisted Seismic Processing and Interpretation Consortium (AASPI) for their guidance and financial support.

LIST OF FIGURES

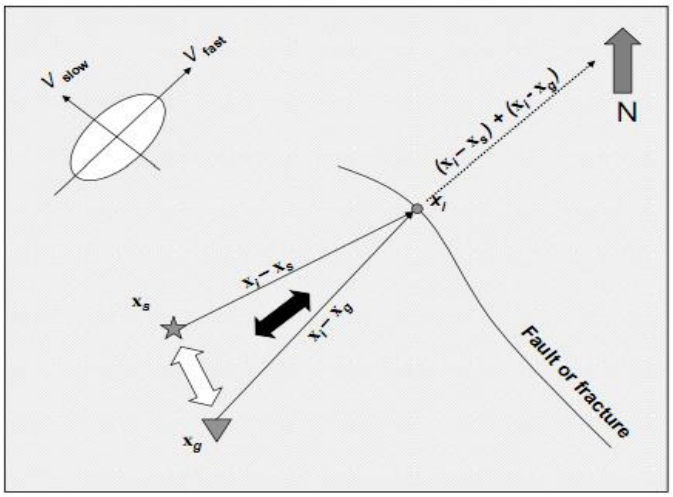

Figure 4.1. New azimuthal binning (after Perez and Marfurt, 2008).

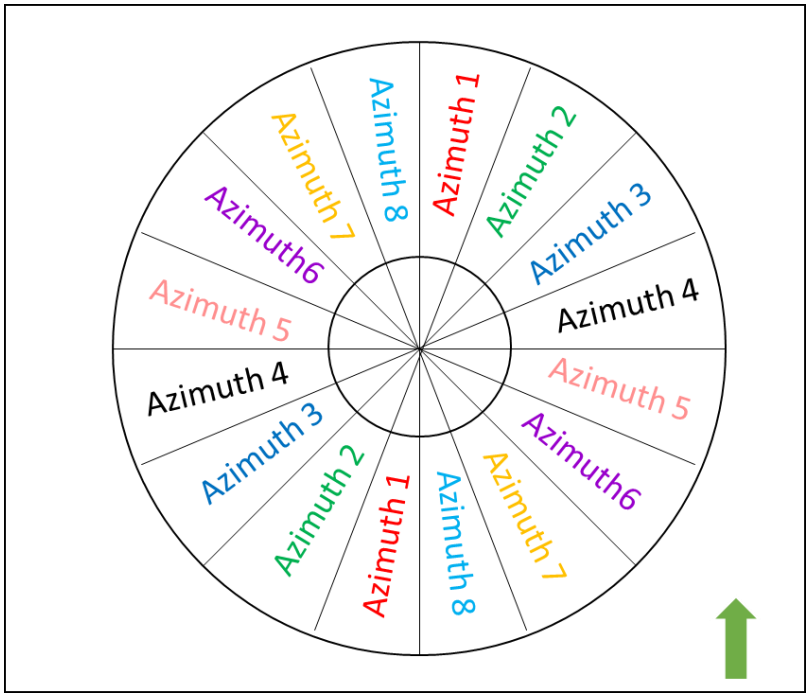

Figure 4.2. Azimuthal bin number for anisotropy analysis.

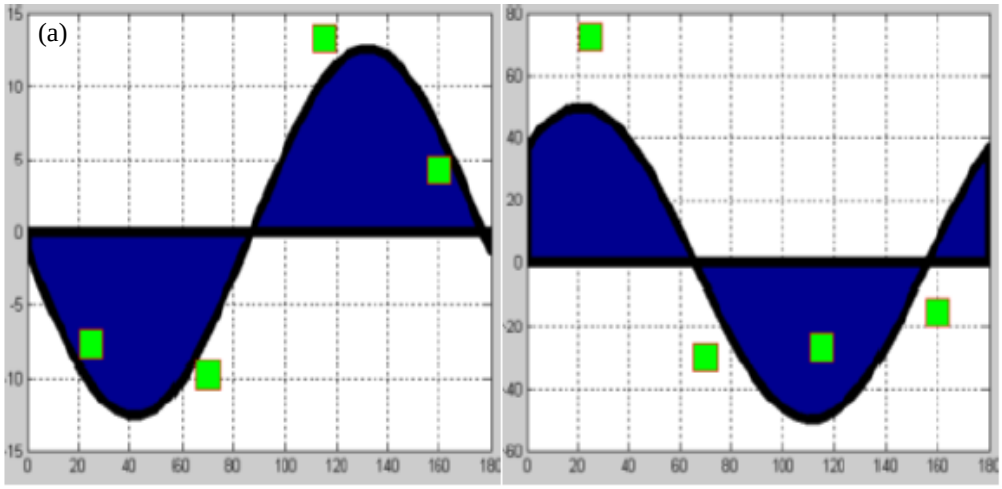

Figure 4.3. Example of (a) good and (b) bad sinusoidal fits to four azimuthal gradient measurements. (after Zhang et al. 2011).

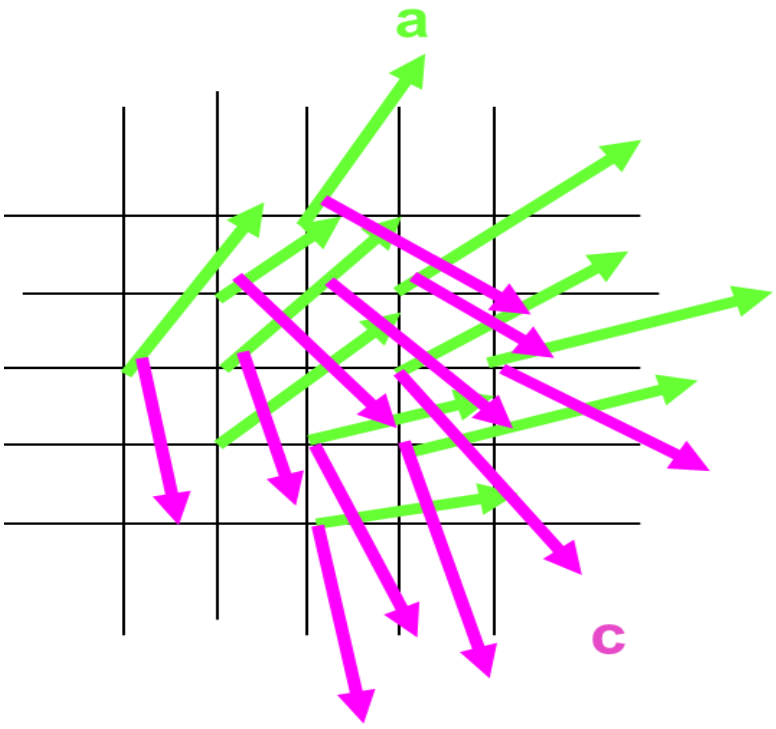

Figure 4.4. Correlation of anisotropy vector a with curvature vector c.

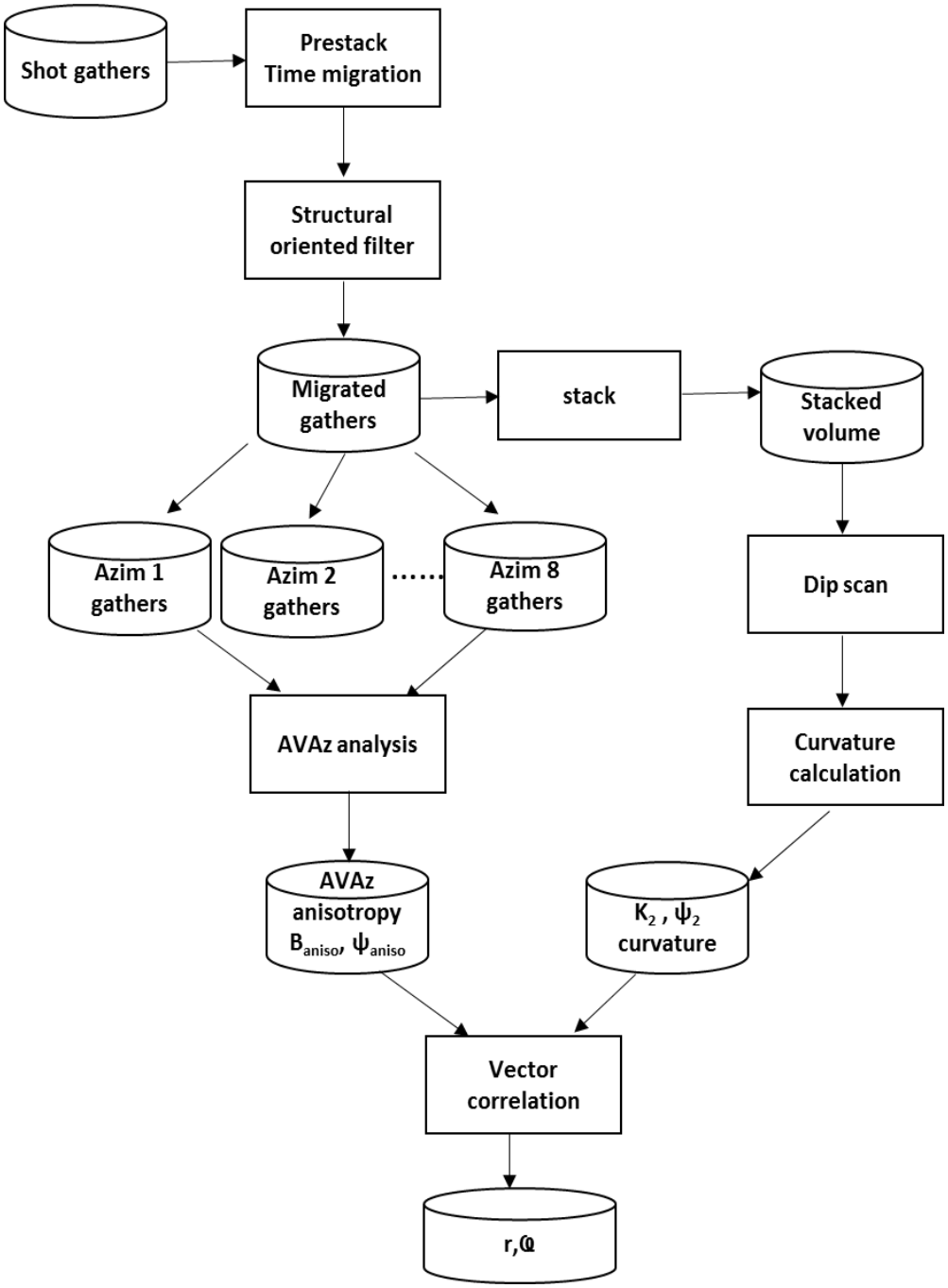

Figure 4.5. Workflow of vector correlation of anisotropy vector a (B_{aniso}, ψ_{aniso}) with curvature c=(K_2, $Ø_2$) vector.

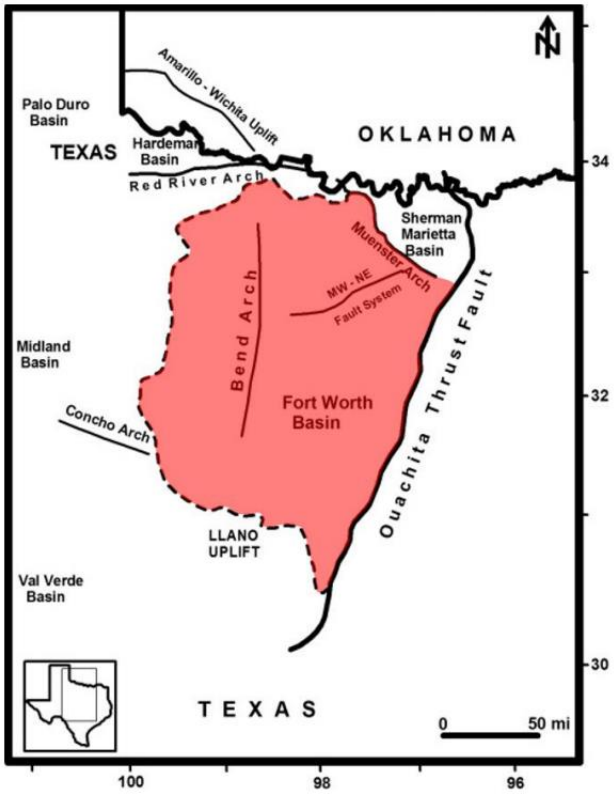

Figure 4.6. Location and aerial extent of the FWB. The boundaries of the FWB, are the Bend arch on the west, the Llano uplift on the south, the Red River and Muenster Arches on the north, and the Pennsylvanian Ouachita overthrust on the east (Modified from Pollastro et al., 2007).

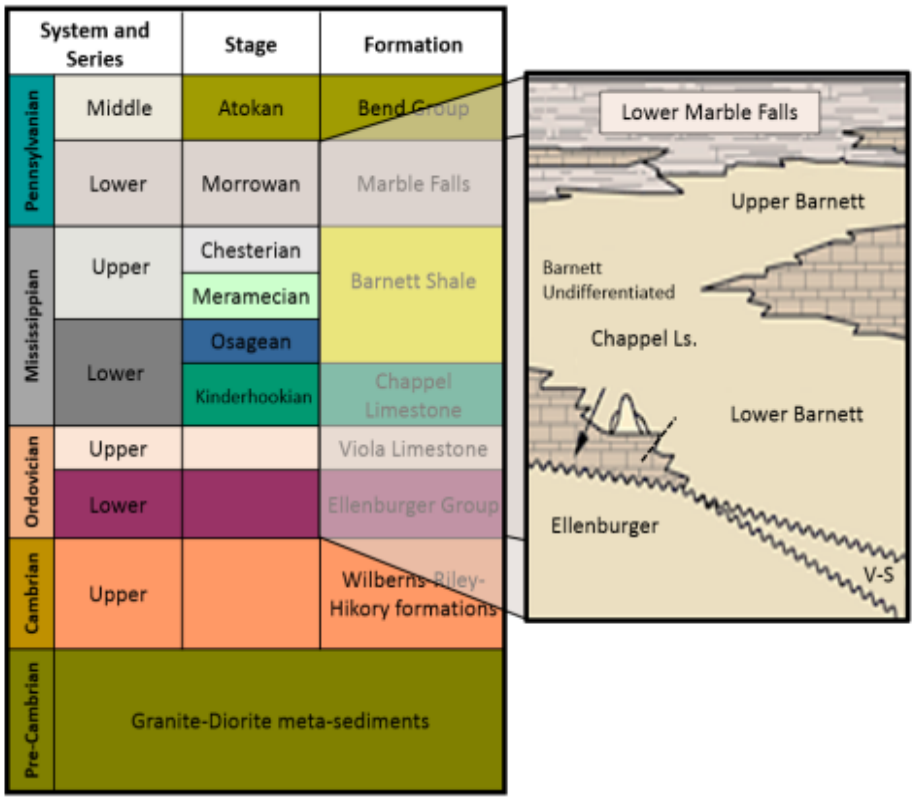

Figure 4.7. Simplified stratigraphic column of the Fort Worth Basin in Wise County, TX. Stratigraphically, the relatively brittle Barnett Shale lies between the more ductile Mable Falls and Viola which form hydraulic fracture limestone units (modified from Montgomery et al., 2005).

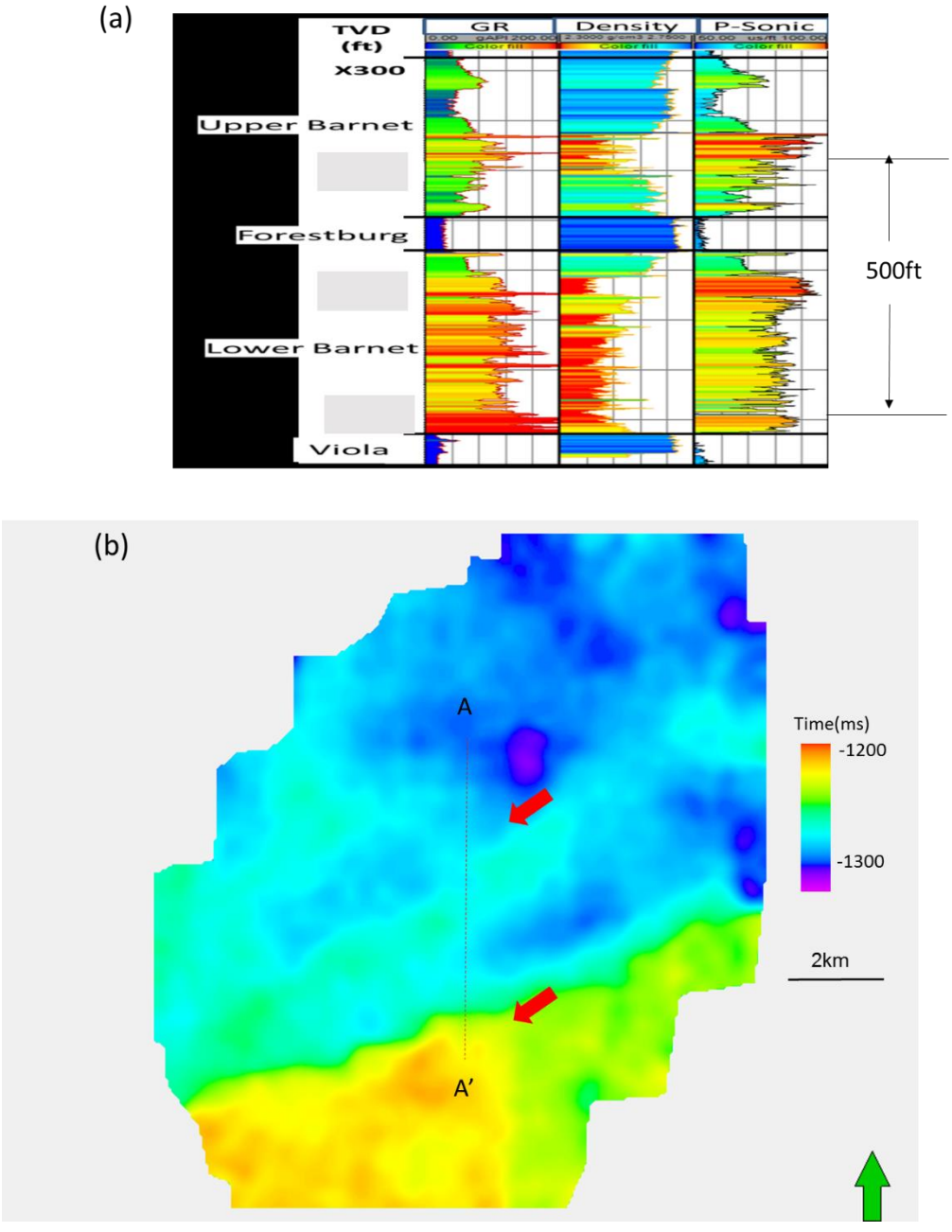

Figure 4.8. (a) A representative log through the Barnett Shale within the survey. (b) Time structure map of the top of Lower Barnett Shale from full stacked volume.

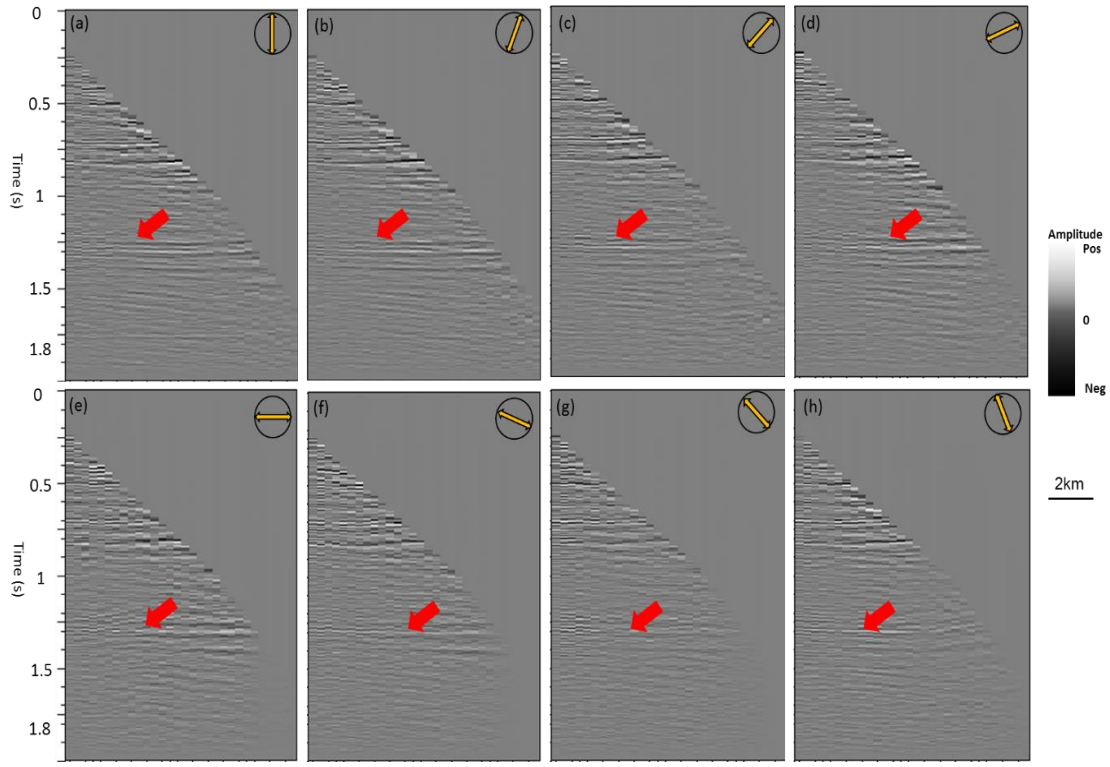

Figure 4.9. A same representative azimuthally limited prestack gathers about (a) 0º, (b) 22.5º, (c) 45º, (d) 67.5º, (e) 90º, (f) 112.5º, (g) 135º, (h) 157.5º. Red arrows denote the lower Barnett shale. Note the difference in amplitude through different azimuths.

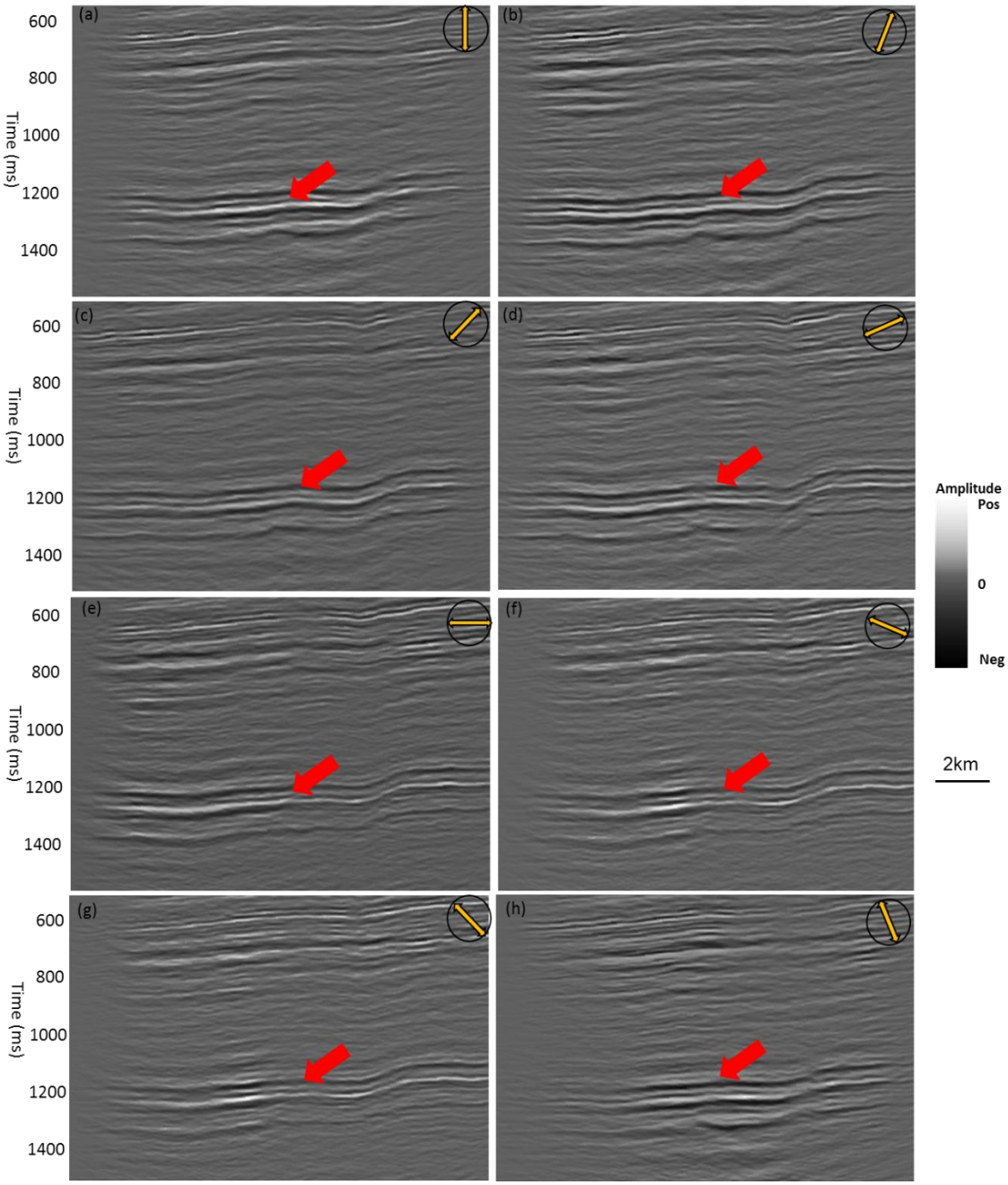

Figure 4.10. Vertical slices through azimuthally limited stacked volumes along profile AA' shown in Figure 3.8b corresponding about (a) 0º, (b) 22.5º, (c) 45º, (d) 67.5º, (e) 90º, (f) 112.5º, (g) 135º, (h) 157.5º. Red arrows denote faults, red arrow denotes the lower Barnett shale. Note the difference in fault illumination at different azimuths.

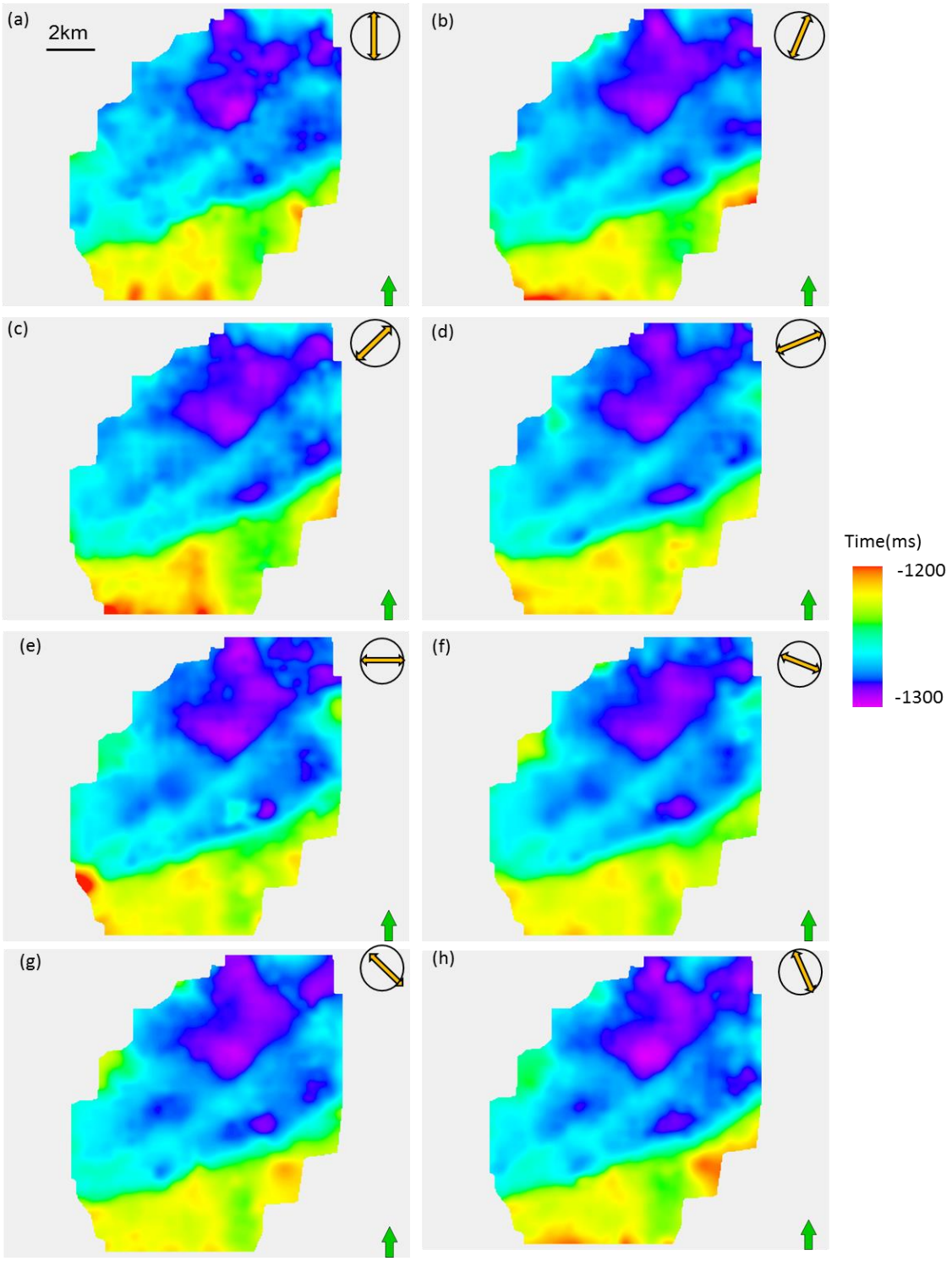

Figure 4.11. Time structure map of top of Lower Barnett Shale about (a) 0º, (b) 22.5º, (c) 45º, (d) 67.5º, (e) 90º, (f) 112.5º, (g) 135º, (h) 157.5º.

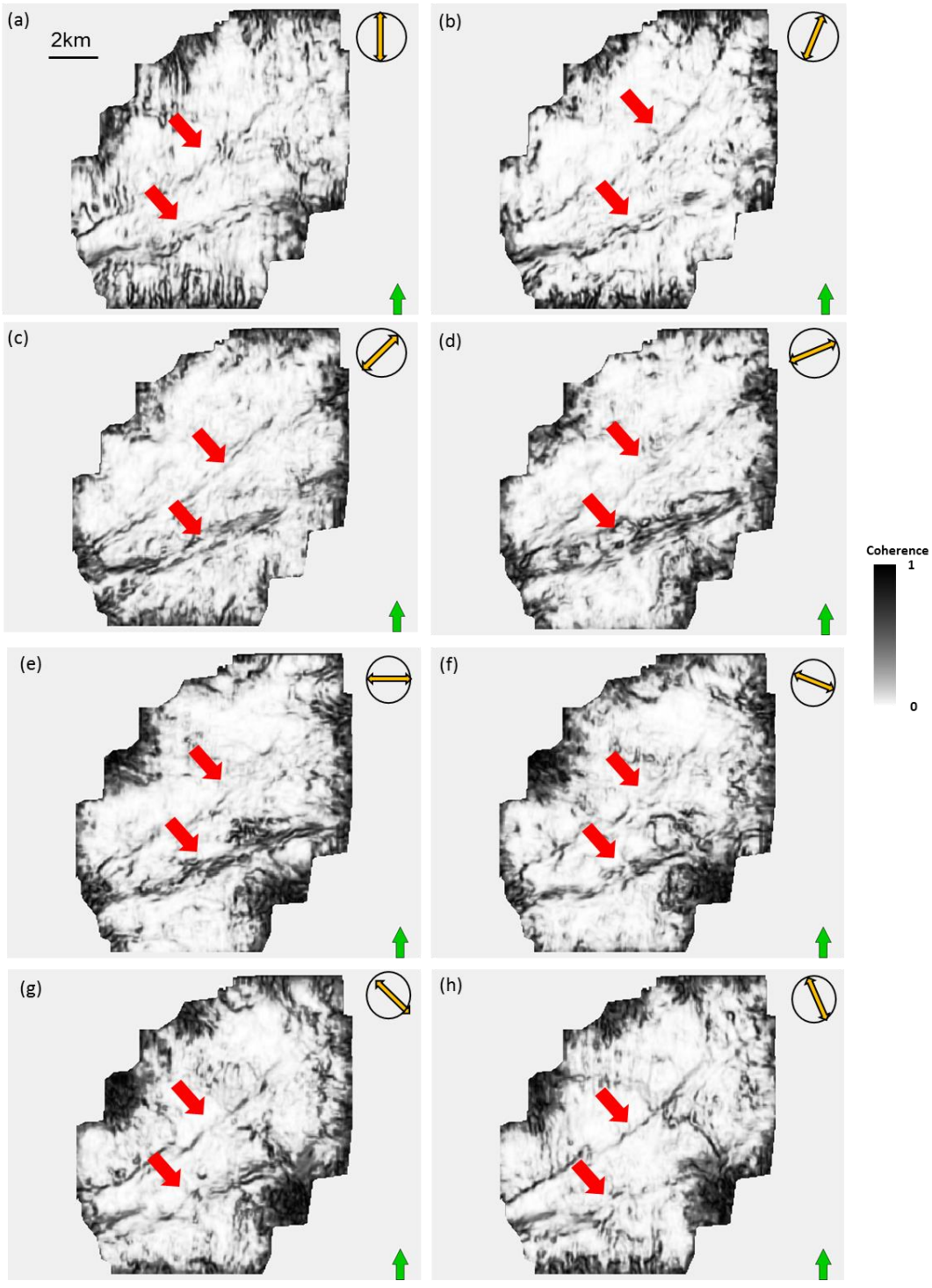

Figure 4.12. Horizon slices on the top of the Lower Barnett Shale through coherence attribute about (a) 0º, (b) 22.5º, (c) 45º, (d) 67.5º, (e) 90º, (f) 112.5º, (g) 135º, (h) 157.5º respectively.

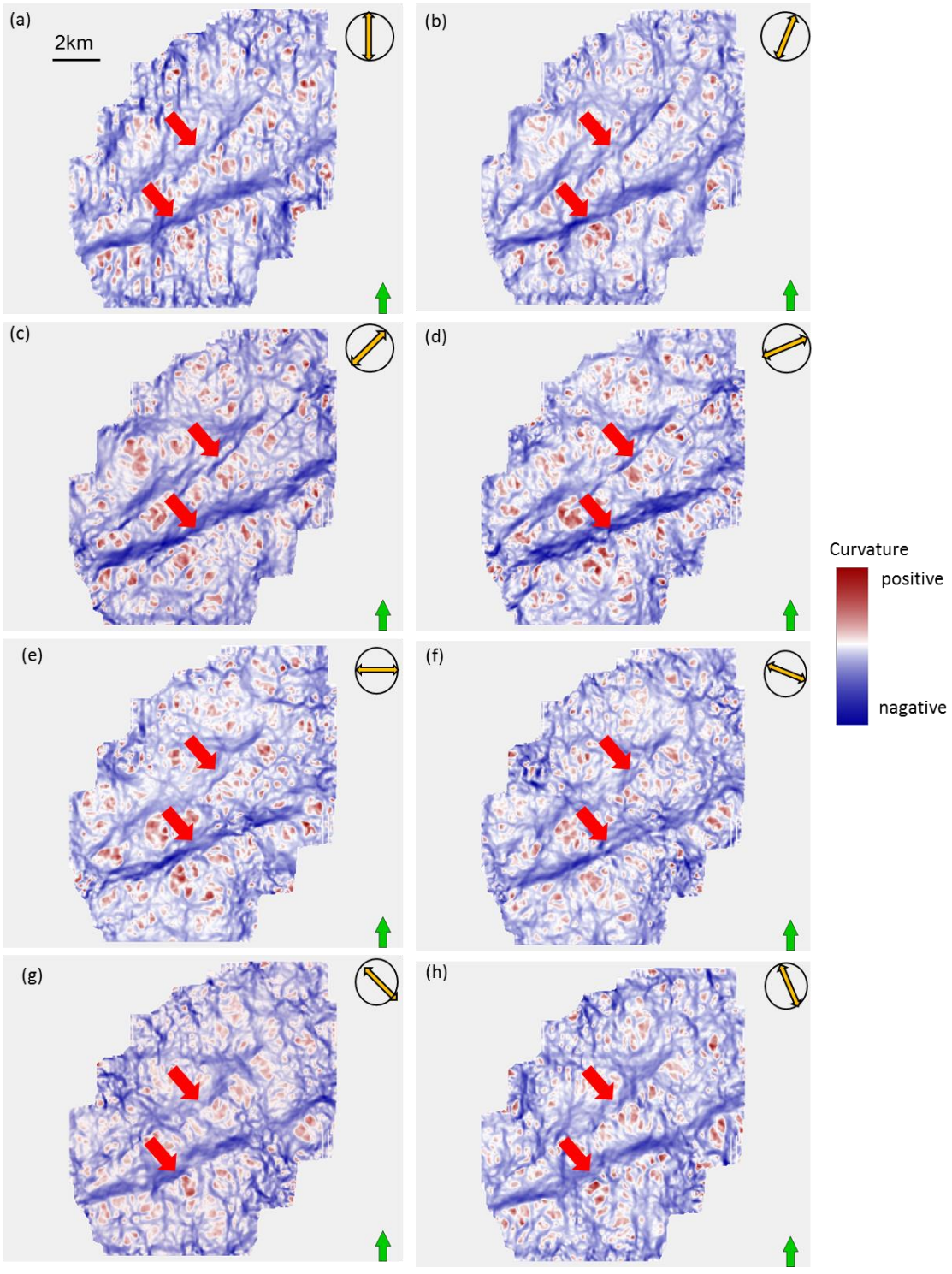

Figure 4.13. Horizon slices along the top of the Lower Barnett Shale through most negative curvature k_2 computed from azimuthally limited stack along (a) 0º, (b) 22.5º, (c) 45º, (d) 67.5º, (e) 90º, (f) 112.5º, (g) 135º, (h) 157.5º respectively. Red arrows donate faults system.

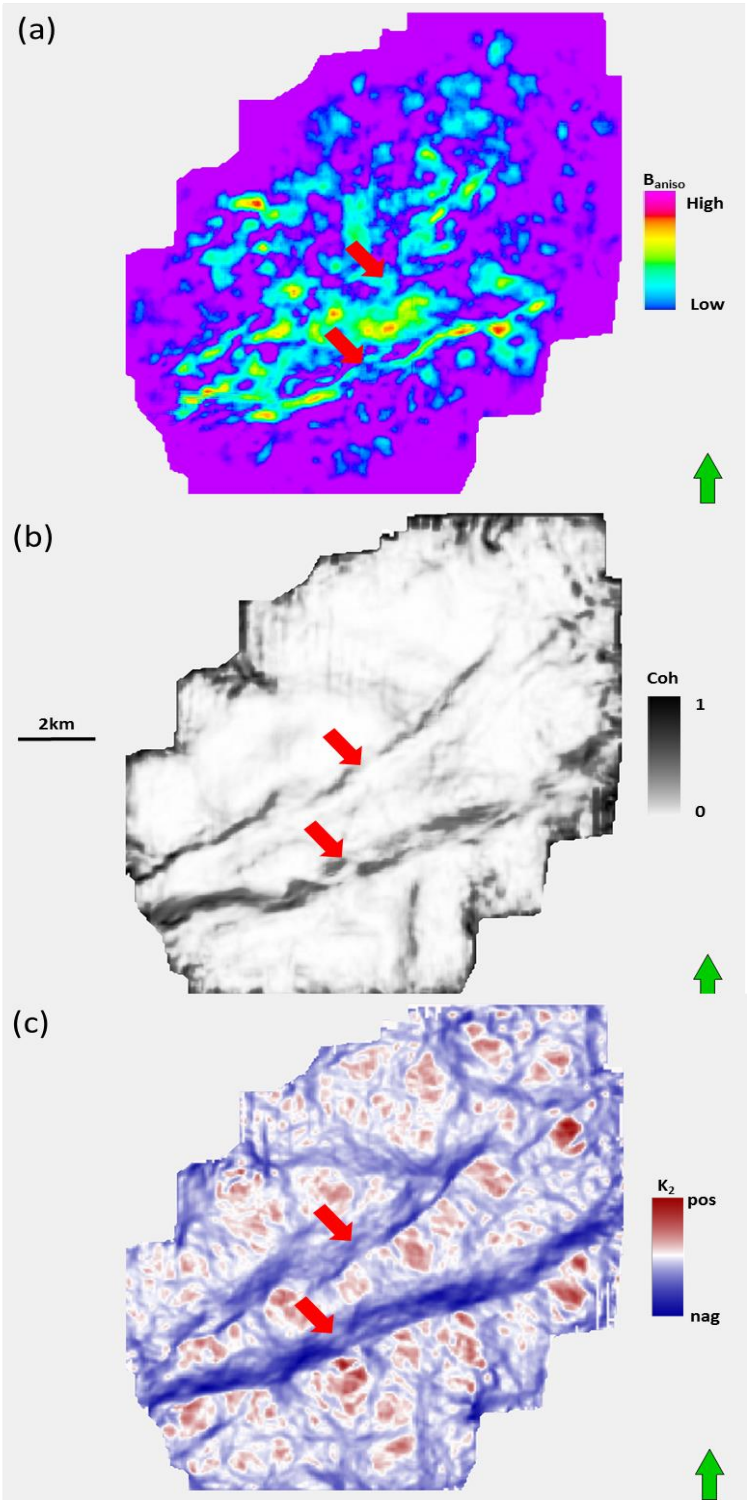

Figure4.14. Horizon slices along the top of the Lower Barnett Shale through (a) B_{aniso}, and (b) coherence, and (c) most negative curvature k_2 compute from full stacked volume.

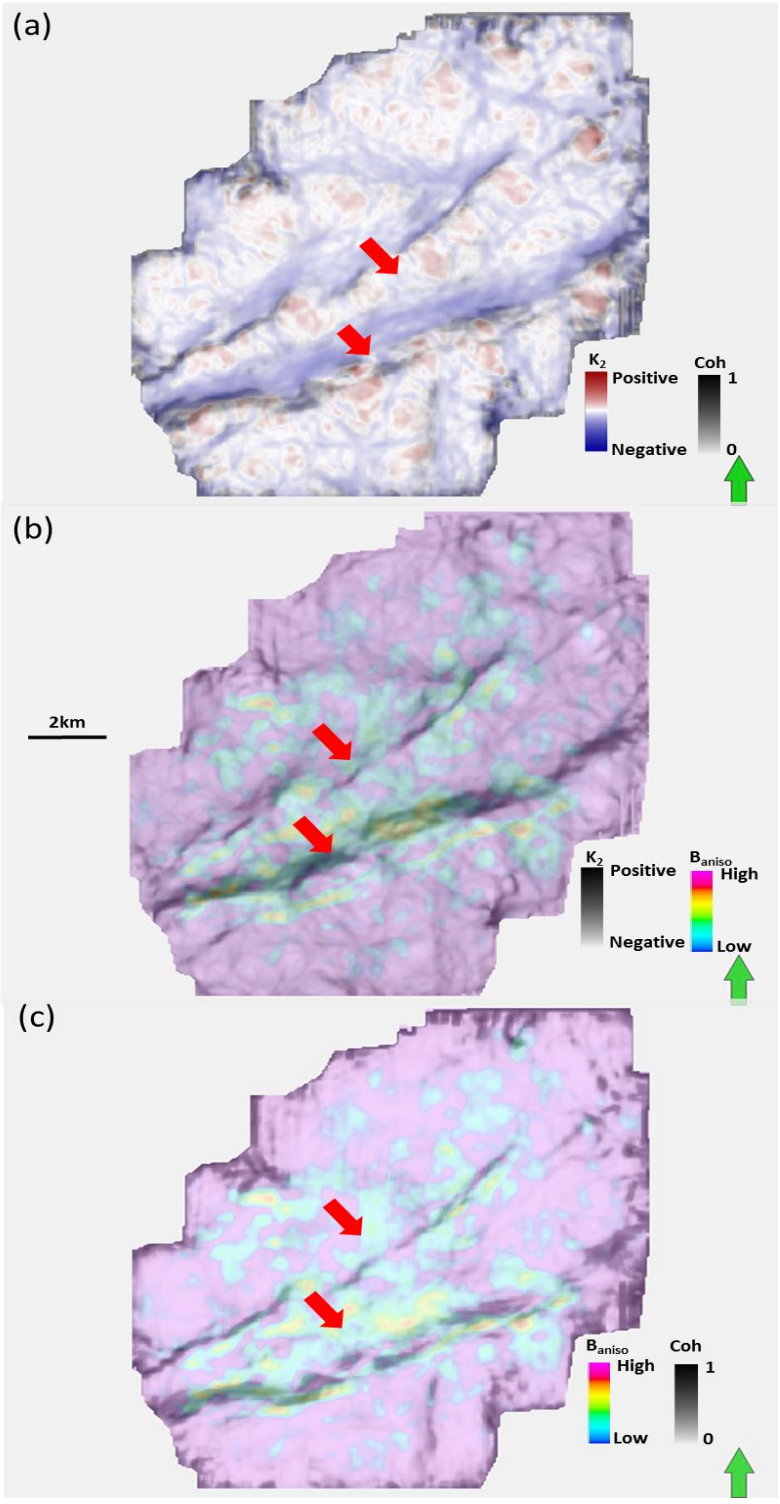

Figure 4.15. Horizon slices along the top of the Lower Barnett Shale through (a) most negative curvature co-rendered with coherence, (b) anisotropy intensity B_{aniso} co-rendered with most negative curvature, (c) anisotropy intensity co-rendered with coherence from full stacked volume. Red arrows denote faults lineanments.

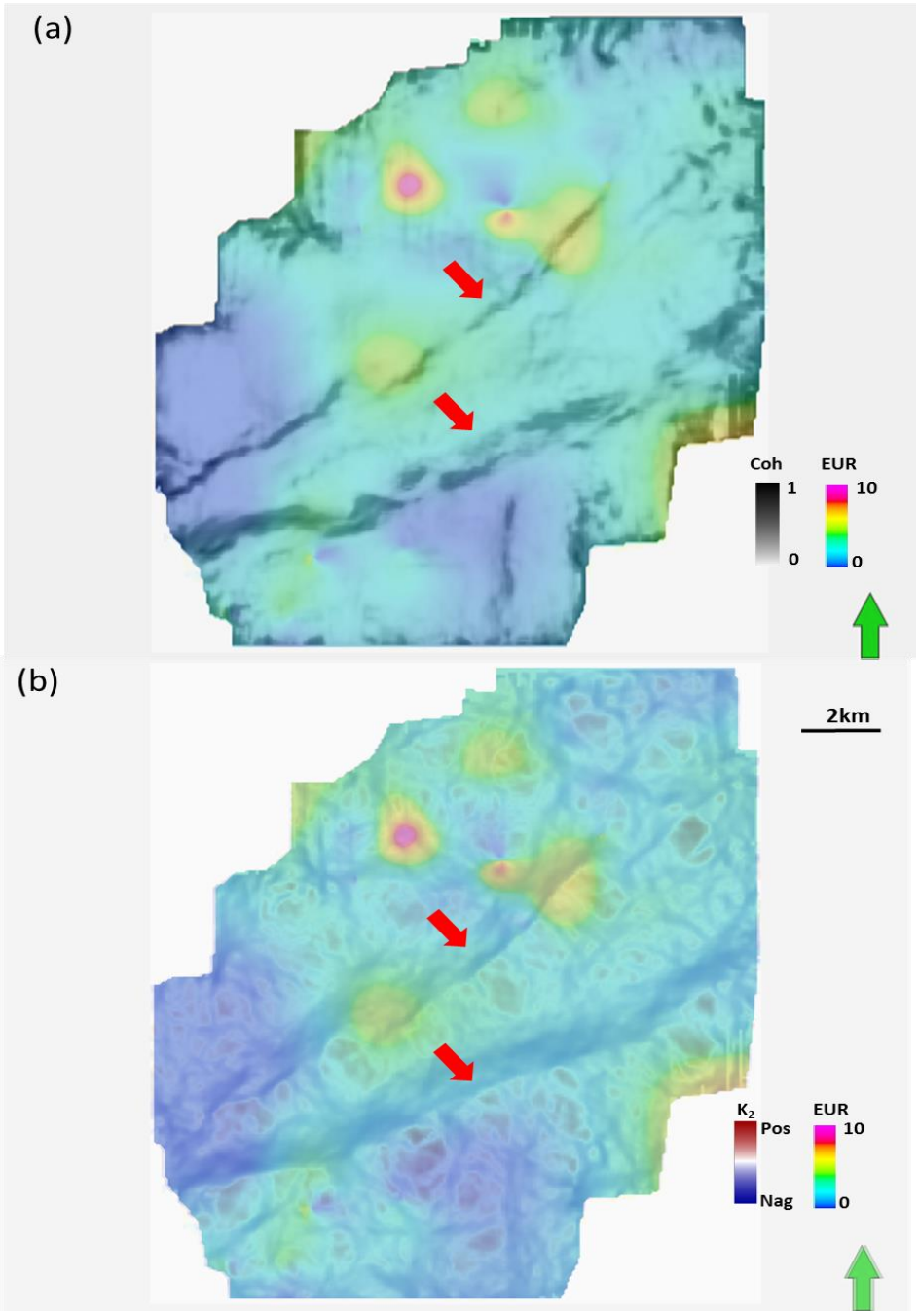

Figure 4.16. Horizon slices along the top of the Lower Barnett Shale through (a) normalized EUR co-rendered with coherence, (b) normalized EUR co-rendered with most negative curvature.

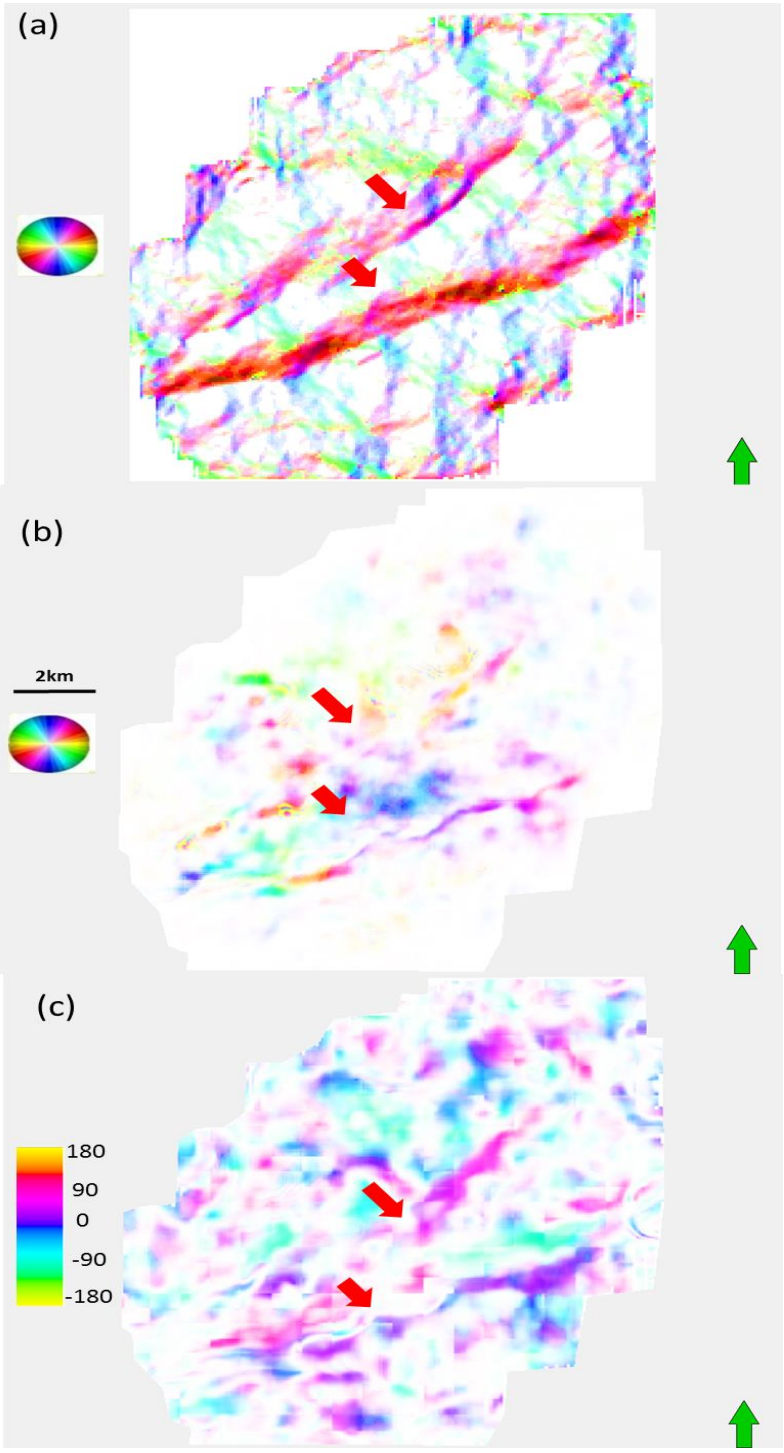

Figure 4.17. Phantom horizon slices on the top of the Lower Barnett Shale through (a) strike of the most negative curvature modulated by its value, (b) strike of AVAz anisotropy modulated by its value, (c) strike of correlation of new vector attributes modulated by its value. Red arrows denote strong visual correlation.

REFERENCES

Akepe, S., 2007, Depth imaging of basement control of shallow deformation; Application to Fort Worth Basin and Teapot Dome data sets: M.Sc. Thesis, University of Houston.

Chopra, S., and K. J. Marfurt, 2007, Seismic attributes for prospect identification and reservoir characterization: Society of Exploration Geophysicists, Tulsa, OK, 456.

Guo, Y., 2010, Seismic attribute illumination of the Woodford Shale, Arkoma Basin. Oklahoma: M.Sc. Thesis, University of Oklahoma.

Guo, H., K. J. Marfurt, S. E. Nissen, and E. C. Sullivan,2010, Visualization and characterization of structural deformation fabric and velocity anisotropy: The leading Edge, **29**, 654-660.

Goodway W., J. Varsek, and C. Abaco, 2006, Practical applications of P-waveAVO for unconventional gas Resource Plays-1 Seismic petrophysics and isotropic AVO: CSEG Recorder Special Edition 2006.

Hunt, L., S. Reynolds, T. Brown, S. Hadley, H. James, J.Downton, and S. Chopra, 2010, Quantitative estimate offracture density variations in the Nordegg with azimuthalAVO and curvature: a case study: The Leading Edge, **29**,1122-1137.

Lynn, H. et al. 1999, P-wave and S-wave azimuthal anisotropy at a naturally fractured gas reservoir, Bluebell-Altamont Field, Utah: Geophysics, **64**, 1312-1328.

Montgomery, S.L., D.M. Jarvie, K.A. Bowker, and R.M. Pollastro, 2005, Mississippian Barnett shale, Fort Worth basin, north-central Texas: Gas-shale play with multitrillion cubic foot potential: AAPG Bulletin, **89**, 155-175.

Jenner, E., 2001, Azimuthal anisotropy of 3-D compressional wave seismic data, Weyburn field, Saskatchewan, Canada: Ph.D. dissertation, Colorado School of Mines.

Perez, G. and K. J. Marfurt, 2008, New azimuthal binning for improved delineation of faults and fractures: Geophysics, **73**, S7-S15.

Pollastro, R.M., D. M. Jarvie, R. J. Hill, and C.W. Adams, 2007, Geological framework of the Mississippian Barnett Shale, Barnett-Paleozoic total petroleum system, BendArch, Fort Worth Basin, Texas: AAPG Bulletin, **91**, 405-436.

Roende, H., C. Meeder, J. Allen, S. Peterson, and D. Eubanks, 2008, Estimating subsurface stress direction and intensity from subsurface full azimuth land data: 78th Annual International Meeting, SEG, Expanded Abstracts, 217-220.

Rueger, A., and I. Tsvankin, 1995, Azimuthal variation of AVO response for fractured reservoirs: 65th Ann. International Meeting, SEG, Expanded Abstracts, 1103-1106.

Rueger, A., 1997, P-wave reflection coefficients for transversely isotropic models with vertical and horizontal axis of symmetry: Geophysics, **62**, 713-722.

Rueger, A., 1998, Variation of P-wave reflectivity with offset and azimuth in anisotropic media: Geophysics, **63**, 935-947.

Sicking, C., S. Nelan and W. Mclain, 2007, 3D azimuthal imaging: 77th Annual International Meeting, SEG Expanded Abstracts, 2364-2367.

Thompson, A., J. Rich, and M. Ammerman, 2010, Fracture characterization through the use of azimuthally sectored attribute volumes: 80th Annual International Meeting, SEG, Expanded Abstracts, 1433-1436.

White, H., B., Dowdell, K. J., Marfurt, Z., Reches, 2012, Calibration of surface seismic attributes to natural fractures using horizontal image logs, Mississippian Lime, Osage County, Oklahoma, 82th Annual International Meeting of the SEG, Expanded Abstracts.

Zhang, K., B. Zhang, J. T. Kwiatkowski, and K. Marfurt, 2010, Seismic azimuthal impedance anisotropy in the Barnett Shale: 80th Annual International Meeting of the SEG, Expanded Abstracts, 273-277.

Chapter 5: Evaluation of AVAz and curvature in a post hydraulically fracture Barnett Shale survey

Shiguang Guo[1], Sumit Verma[1], Bo Zhang[1], and Kurt J. Marfurt[1],

[1]The University of Oklahoma, ConocoPhillips School of Geology and Geophysics

ABSTRACT

Azimuthal anisotropy can be caused by natural fractures, hydraulically induced fractures, and azimuthal variation of the horizontal stress. Induced hydraulic fractures are essential to hydrocarbon production from unconventional reservoirs as these fractures can provide a pathway for hydrocarbon flow. Knowledge of induced fractures can help to evaluate the success of reservoir stimulation. Seismic P-waves through fracturing media can exhibit azimuthal variation in travel time, amplitude, and thin bed tuning, so the AVAz can be used to evaluate the hydraulic fracturing caused anisotropy. The Barnett Shale of Fort Worth Basin was the first large scale commercial shale gas play. We analyze two adjacent Barnett Shale seismic surveys, one acquired before hydraulic fracturing and the other acquired after hydraulic fracturing by over 400 wells. While not a rigorous time-lapse experiment, comparison of the AVAz anisotropy of these two surveys provides valuable insight into the possible effects of hydraulic fracturing. We find that in the survey acquired prior to hydraulic fracturing that AVAz anomalies are both stronger and highly correlated to major structural lineaments measured by curvature. In contrast, AVAz anomalies in the acquired after hydraulic fracturing are weaker and compartmentalized by rather than correlated to most-positive curvature lineaments. Five microseismic experiments within the survey show that these ridge lineaments form

fracture barriers. These findings suggest that future time-lapse experiments may be valuable in mapping the modified horizontal stress field to guide future drilling and in recognizing zones of by-passed pay.

INTRODUCTION

Significant effort has been devoted to predict and map the seismic responses due to fracturing. Direct measures of fractures include Amplitude vs. Azimuth (AVAZ) (Ruger, 1998; Goodway et al., 2007b) and Velocity vs. Azimuth (VVAz) (Sicking et al., 2007; Jenner, 2001). Geometric attributes computed from post-stack data such as coherence and curvature have also been used for indirect fracture prediction (Chopra and Marfurt, 2007; Thompson et al. 2010, Guo et al., 2010).

The Barnett Shale in the Fort Worth Basin was the first large scale commercial shale gas play and is characterized by low permeability and cemented natural fractures. In our area of study, Devon Energy hydraulically fractured the subsurface to increase permeability by injecting high pressure fluid and proppant using an average of 10 injection wells per square mile. In the first survey, wide-azimuth seismic data were acquired after hydraulic fracturing. In this survey, our objective is to map the orientation and intensity of induced rather than natural fractures, attempt to identify reservoir compartmentalization, and identify potential by-passed pay zones. In the second survey, the seismic data were acquired before hydraulic fracturing and thus serves as a base line.

Zhang (2010) and Thompson (2010) found correlations between compartmentalized variations in anisotropy measured by AVAz and structural deformation measured by curvature. Microseismic experiments showed that measured events avoided structural ridges and occurred most often in bowl shaped regions. They

then hypothesized that ridge fracture barriers compartmentalized the subsequent anisotropic behavior, however, in the absence of a true time-lapse experiment, it was unclear how much of this anisotropy existed prior to completion. In this study, we apply the same AVAz workflow to the two adjacent seismic surveys, one acquired before and the other acquired after hydraulic fracturing. We begin our paper with a summary of the processing and AVAz analysis workflow. Then we use seismic attributes to map fault and fracture trends. Next, we evaluate the hypothesis that horizontal well stimulation and hydraulic fracturing modify the reservoir anisotropy by comparing the AVAz anisotropy and curvature analysis of the two surveys. We conclude with a hypothesis that explains these differences and suggest follow-up time-lapse experiments to more quantitatively measure the impact of hydraulic fracturing on seismic response.

APPLICATION

The Fort Worth Basin is a shallow N-S elongated foreland basin that encompasses roughly 15,000 mi^2 in North Texas and formed during the late Paleozoic Ouachita Orogeny (Walper, 1982). A result of the collision of North and South America, the Fort Worth Basin is delineated to the East by the Ouachita Thrust Front, to the North by the Red River Arch, to the N-NE by the Muenster Arch, to the West by the Bend Arch, Eastern Shelf, and Concho Arch, and to the South by the Llano Uplift (Perez, 2013). The Barnett Shale is the primary source rock for oil and gas produced from the Paleozoic reservoir rocks in the basin (Jarvie et al., 2007). In less than a decade, the Barnett Shale play became the largest natural gas play in the state of Texas with an estimated mean volume production of about 26 TCF of recoverable gas (Pollastro et al., 2007).

The Barnett Shale sequence consists of alternating shallow marine limestone and black, organic-rich shale. On the eastern side of the FWB, the Barnett Shale can be subdivided into an upper and lower interval interbedded by a dark limestone interval, known as the Forestburg Limestone. The vertical section of our study survey is 1,300 ft on average and consists of five units of limestone and shale formations, listed from top to bottom with their average thicknesses: the Marble Falls Limestone (160 ft), the Upper Barnett Shale (365 ft), the Forestburg Limestone (45 ft), the Lower Barnett Shale (510 ft), and the upper section of the Viola Limestone (225 ft).

The Viola, Forestburg, and Marble Falls Limestones are hydraulic fracture barriers and are not considered production targets because they are water-bearing. The Viola Formation deposited on top of the karsted Ellenburger Formation (Loucks, 2008) and in other parts of the Fort Worth Basin presents a potential risk of water production. In our area of study, the Forestburg Limestone divides the Upper Barnett and the Lower Barnett shales into two members, which must be treated and fractured separately. The Barnett Shale is organic-rich and mainly dominated by clay, quartz and carbonate minerals as shown in Figure 5.1 (Perez, 2013). We analyze two slightly overlapping surveys (Figure 5.2). Survey B was acquired before hydraulic fracturing, and has been previously discussed by Akepe et al. (2007) and Perez and Marfurt (2008). Survey A was acquired after hydraulic fracturing with about 308 vertical or directional wells and 127 horizontal wells and has been previously discussed by Zhang et al (2013), Trumbo and Rich (2013), and Perez et al. (2013).

Figure 5.3a shows a time structure map of the Viola Limestone while Figure 5.3b shows a representative vertical slice AA’ through the data. Figure 5.3c shows the RMS

amplitude within a 20 ms window centered along the Viola Limestone surface for the two surveys. Note the similarity of the RMS amplitude for two surveys. Figure 5.4 shows a representative suite of azimuthally limited prestack gathers. Note the change in amplitude at different azimuths caused by anisotropy.

Figure 5.5 shows eight azimuthally limited stacked volumes. Note the stacked volumes at 112.5^{o} and 135^{o} show higher resolution than those at 22.5^{o} and 45^{o} around the fault zone. The azimuths 22.5^{o} and 45^{o} are approximately parallel to the strike of the faults, while azimuths 112.5^{o} and 135^{o} are perpendicular to the strike of the faults. More energy from the fault planes is measured at these later two azimuths. Figure 5.6 shows the corresponding time structure maps of the top of the Viola Limestone. Note the subtle differences in the structural patterns of the Viola Limestone for different azimuths, representing velocity vs. anisotropy (VVAz) effects. Afterwards, I will flatten these stacked volumes along the Viola Limestone to remove VVAz effects before AVAz analysis.

Figures 5.7a-c show phantom horizon slices 20 ms above the top of the Viola Limestone through variance, the most negative curvature k_2, and the most positive curvature k_1. Red arrows denote faults KK', HH', GG' and FF'. Figures 5.7d co-renders all of these images. Note that the visually high correlation between the two curvatures and variance shows the faults in the two surveys.

Figure 5.8a shows phantom horizon slices 20 ms above the top of the Viola Limestone through the strike of the most positive curvature k_1 modulated by its value co-rendered with variance. Figure 5.8b shows the same phantom horizon through the strike of the most negative curvature k_2 modulated by its value co-rendered with variance. Red

arrows indicate the KK', HH', GG' and FF' faults, which are characterized by NE-SW azimuth of curvature.

Figure 5.9a and b from Bourne et al. (2000) show the elastic stress field calculated for a three dimensional network of right-lateral strike-slip faults. The resulting stress field is expected to govern the distribution of fault-related, small-scale tensile and shear fractures. Figure 5.10a and b show the distribution of tensile fractures around the tip of a strike-slip fault at Nash Point, Wales and the associated sketch of the stress distribution. It implies that fractures propagate at high angles to the fault plane as rocks on that side of the fault have been stretched parallel to the fault by displacements away from the fault tip. Note the different pattern of stress and fracture distribution on different sides of the fault plane.

Figures 5.11 shows a phantom horizon slice 20 ms above the Viola Limestone through anisotropy strike Ψ_{azim} modulated by its value B_{aniso} co-rendered with variance (Figure 5.11a) and the most positive curvature (Figure 5.11b). For survey B note the high correlation between structural faults and high anisotropy intensity. The strike of anisotropy on the north side of fault GG' appears as purple, denoting N- NE direction parallel to the faults. To the south, it appears as yellow green, E-SE trending more perpendicular to the faults. This kind of pattern indicates that the natural fractures on different side of strike-slip faults show different direction, which is consistent with the pattern found by Bourne, et al. (2000) shown in Figures 5.9 and 5.10. Away from the faults, the anisotropy is weak er and appears as green and cyan, denoting a NW-SE direction. For survey B, the anisotropy is relatively high and is concentrated near the faults. In contrast, for survey A, high anisotropy intensity zone is no longer located around

the faults, suggesting the hydraulic fracturing has somehow changed the anisotropy. Examining Figure 5.11b, note that the most positive curvature appears to form the boundary of different reservoir compartments each with a distinct azimuth (Zhang et al. 2013).

Figures 5.12a and b show phantom horizon slices 20 ms above the Viola Limestone through normalized EUR co-rendered with variance and most positive curvature. Note Note that most-positive curvature ridges appear to form boundaries to production for both surveys A and B. This observation is consistent with that of Trumbo and Rich (2013) who use microseismic data to show such ridges form fracture barriers.

Figures 5.13a and b show phantom horizon slices 20 ms above the Viola Limestone through vector correlation between anisotropy and most negative curvature co-rendered with variance and most positive curvature. The correlation is relatively high (blue, green and magenta colors) along faults F and G, suggesting structural control of AVAz. In contrast, the correlation is quite low (more gray colors) along and between faults KK' and HH' suggesting that hydraulic fracturing has modified the initial stress field.

Figures 5.14a and b show microseismic events, horizontal well paths and production plotted on top of phantom horizon slices 20 ms above the Viola Limestone through normalized EUR co-rendered with most positive curvature and AVAz vector. Two hundreds horizontal wells have been drilled in the NW-SE direction, which is perpendicular to the regional maximum horizontal stress. Five of these two hundreds wells were monitored using microseismic technology along completion. Anecdotally, these events (white scales) fall on areas of low anisotropy, consistent with our hypothesis that hydraulic fracturing results in a more isotropic (or perhaps orthotropic) seismic

behaviors. The stronger anisotropy occurs in areas completed using vertical wells, which were drilled earlier using older completion technology and did not penetrate as much of the reservoirs.

CONCLUSIONS

Comparing the anisotropy analysis of two adjacent surveys, one with seismic data acquired before hydraulic fracturing and the second after, we see that hydraulically induced fracturing modifies seismic P-wave anisotropy. Even though completion takes place across ridges, the resulting microseismic events avoid these ridges and concentrate in the intervening faults (Trumbo and Rich, 2013). EUR also appears to be compartmentalized by these ridges.

The vector correlation between most positive curvature and AVAz anisotropy for the survey acquired before hydraulic fracturing indicates complicated patterns consistent with strike-slip faulting. This correlation is diminished after hydraulic fracturing.

Though encouraging, this experiment does not prove my hypothesis that hydraulic fracturing decreases seismic anisotropy. To do so, a wide-azimuth time-lapse survey that covers, as accurately as possible, the same subsurface area is required. Equally important, I do not know whether the reduction in anisotropy is due to rubblizing of the reservoirs (making them more isotropic) or due to the creation of orthogonal fractures (making is more orthotropic). Such understanding may be critical in future restimulation, determining the direction of new wells, and to mapping zones of by-passed pay.

ACKONWLEDGEMENTS

The authors would like to thank Devon Energy for funding, encouragement, and the authorization to publish this work. I would also like to thank the sponsors of Attribute-Assisted Seismic Processing and Interpretation Consortium (AASPI) for their guidance and financial support.

LIST OF FIGURES

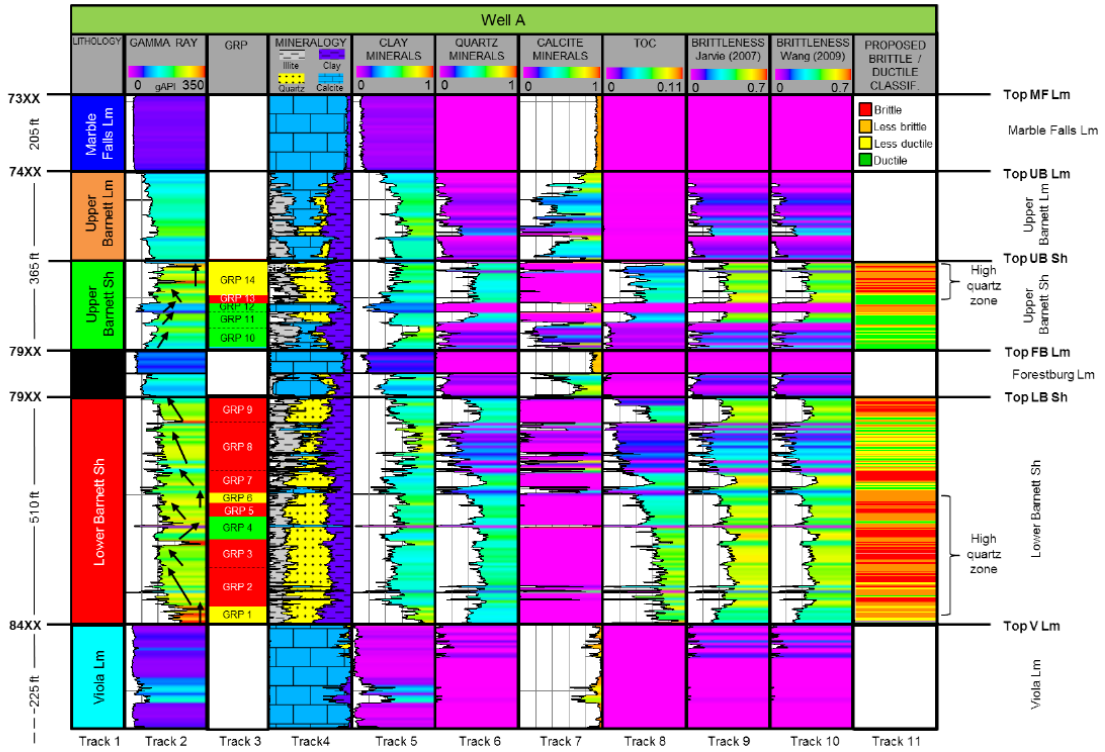

Figure 5.1. Gamma ray parasequences, and mineralogy logs corresponding to Well A. (Perez, 2013)

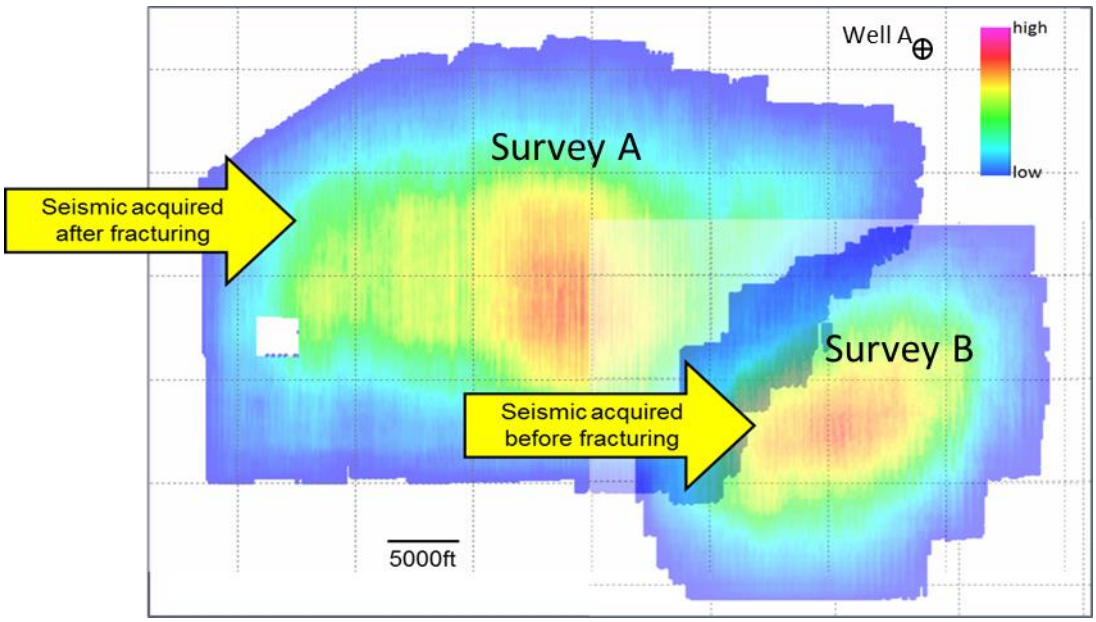

Figure 5.2. Fold map of two slightly overlapping surveys acquired over the Fort Worth Basin. The smaller survey B was acquired before hydraulic fracturing as shown by yellow arrow, while the larger survey was acquired after 400 wells were hydraulically fractured.

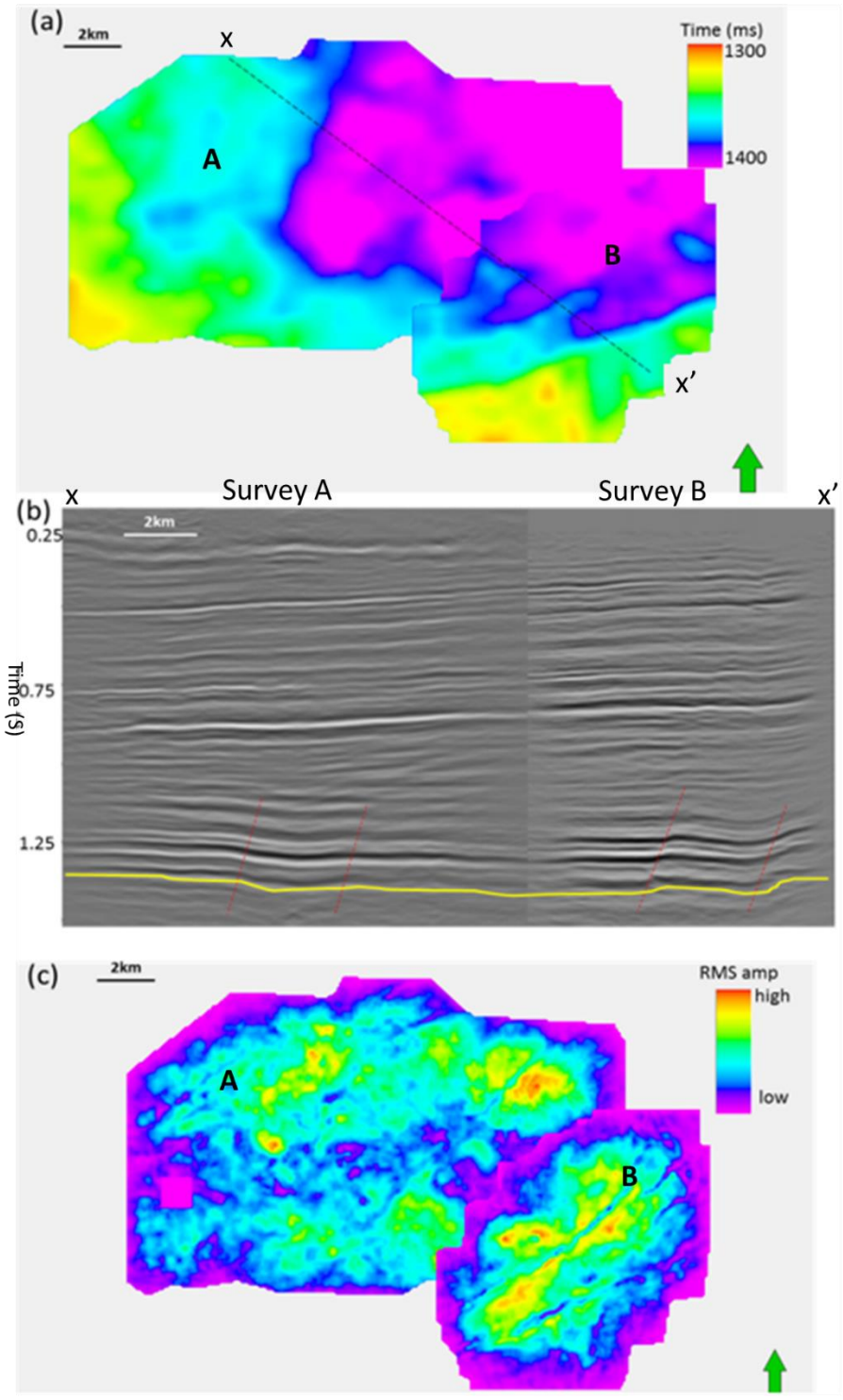

Figure 5.3. (a) Time structure map of the Viola Limestone from full stacked volume in Fairview survey. (b) Vertical slice through AA'. Yellow line denotes top of Viola Limestone. Red dash lines denote main faults. (c) RMS amplitude on 20 ms window centered at Viola Limestone surface for two surveys.

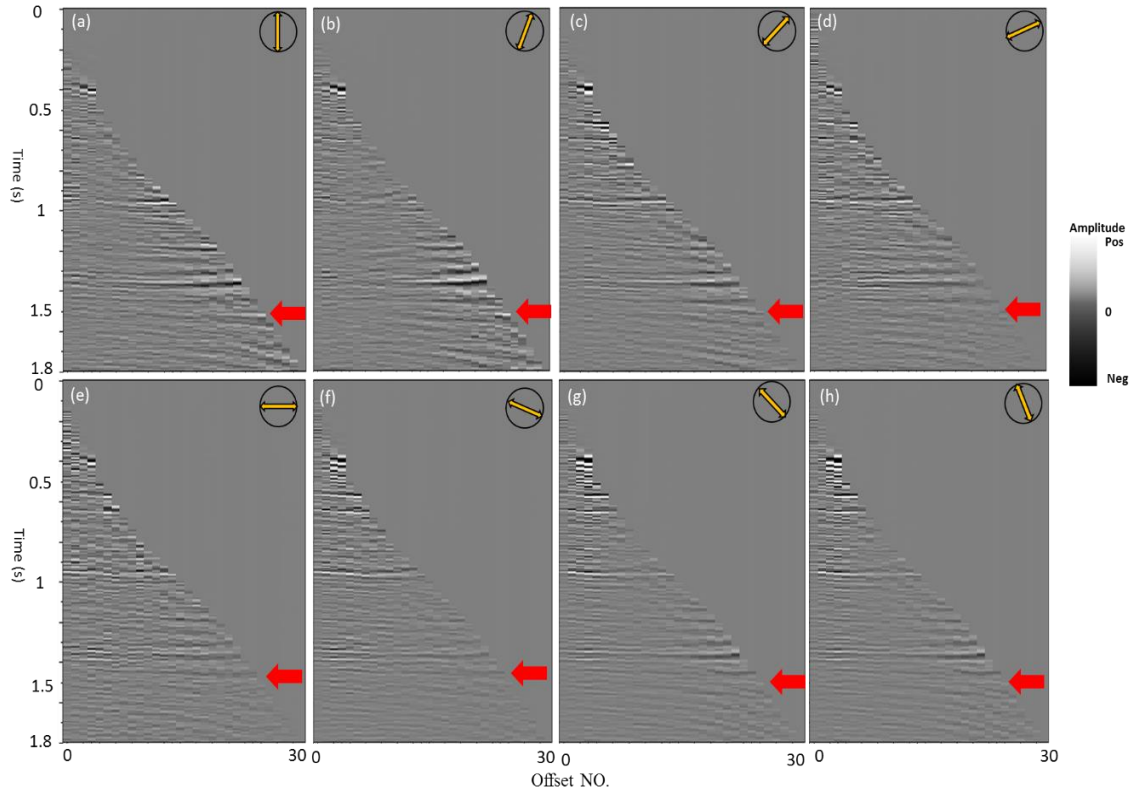

Figure 5.4. A representative azimuthally limited prestack gathers from survey A about (a) 0º, (b) 22.5º, (c) 45º, (d) 67.5º, (e) 90º, (f) 112.5º, (g) 135º, and (h) 157.5º. Note the subtle difference in amplitude through different azimuths along the top Viola (red arrows).

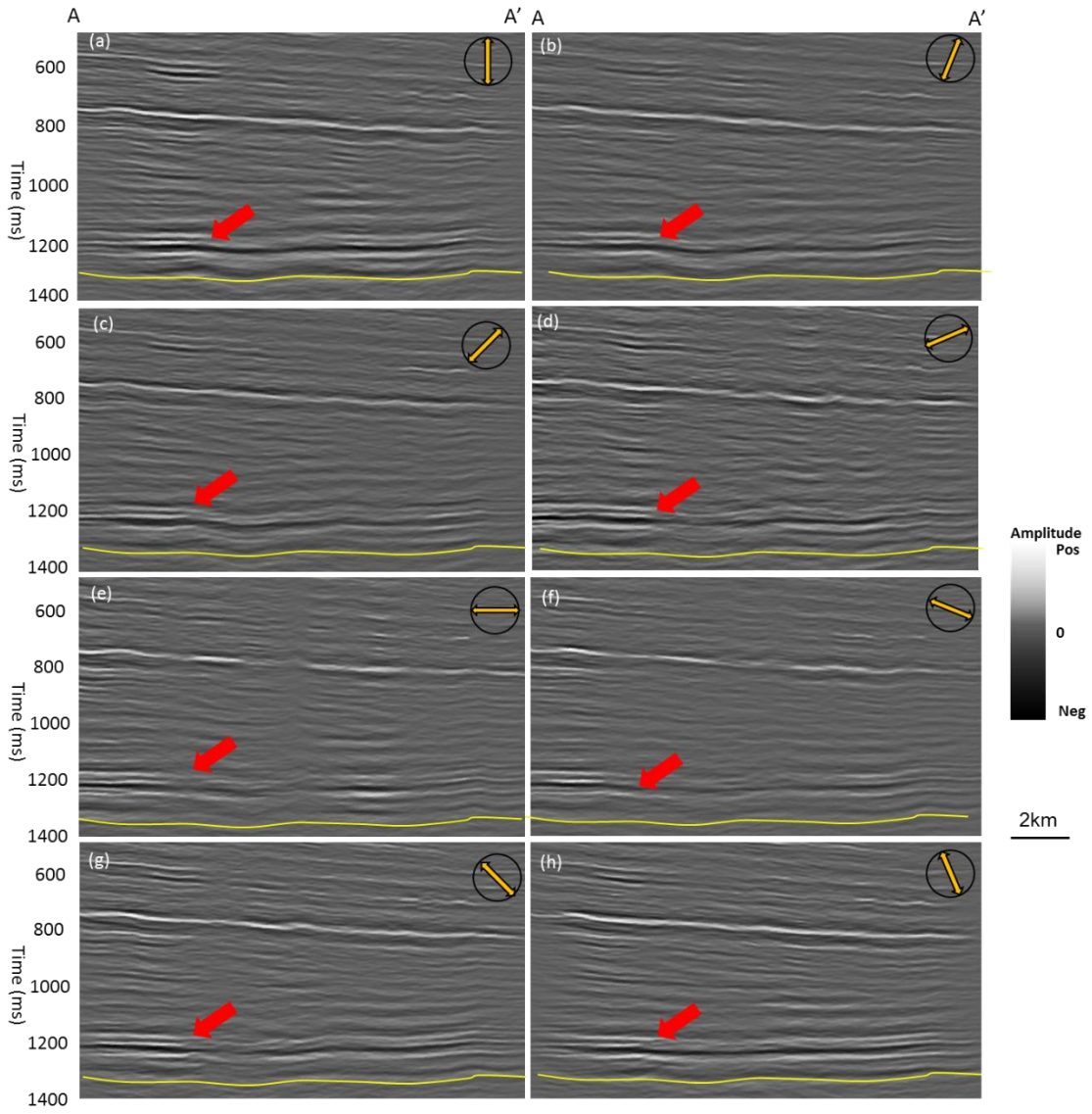

Figure 5.5. Vertical slices through azimuthally limited stacked volumes along profile AA' corresponding to (a) 0º, (b) 22.5º, (c) 45º, (d) 67.5º, (e) 90º, (f) 112.5º, (g) 135º, and (h) 157.5º. Yellow lines denote the top Viola Limestone. Note the difference of amplitude at different azimuths. Red arrows show faults.

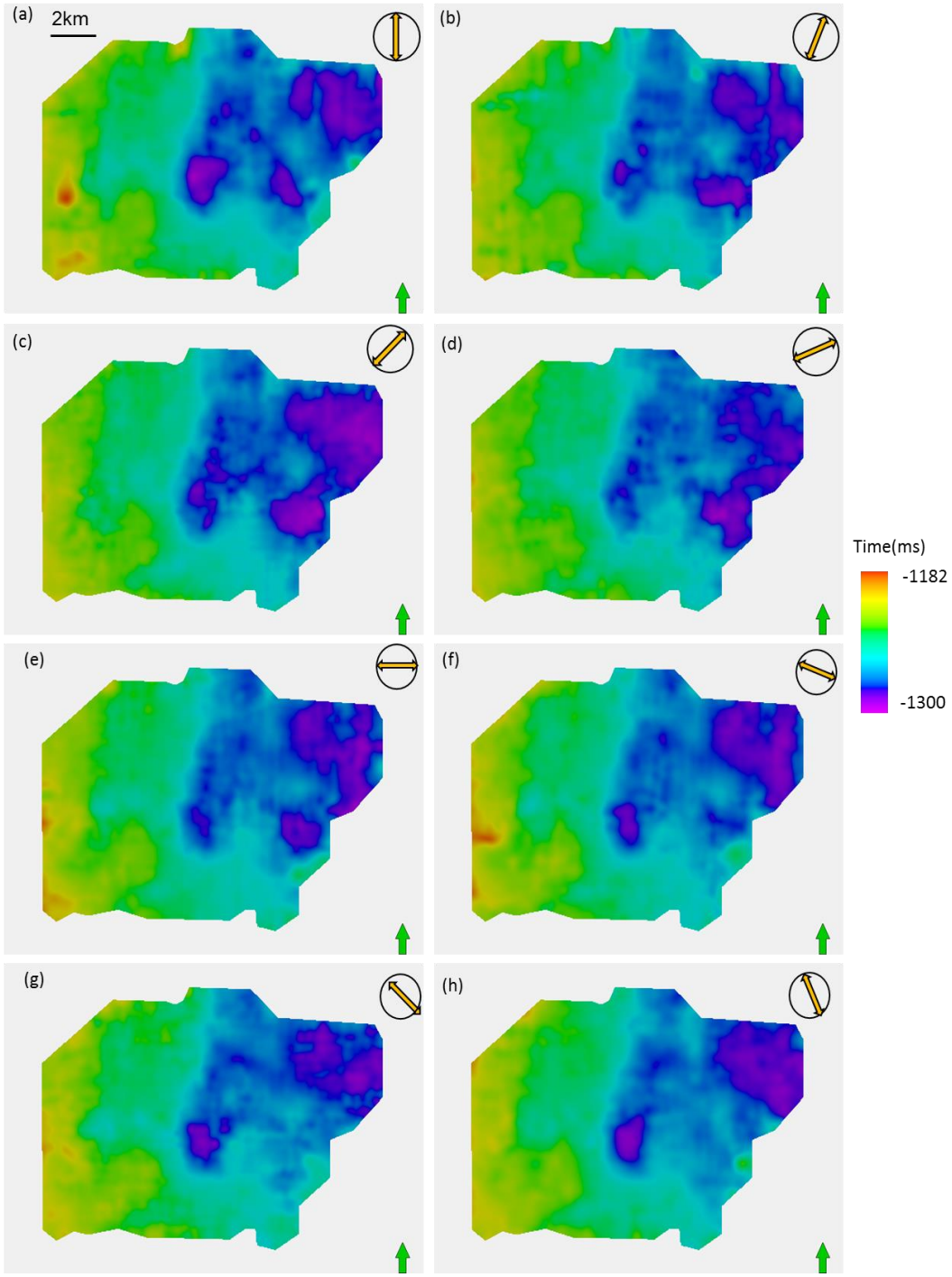

Figure 5.6. Time-structure maps of Viola Limestone about (a) 0º, (b) 22.5º, (c) 45º, (d) 67.5º, (e) 90º, (f) 112.5º, (g) 135º, and (h) 157.5º. The differences in these maps are due to velocity vs. azimuth (VVAz) changes in two-way travel time.

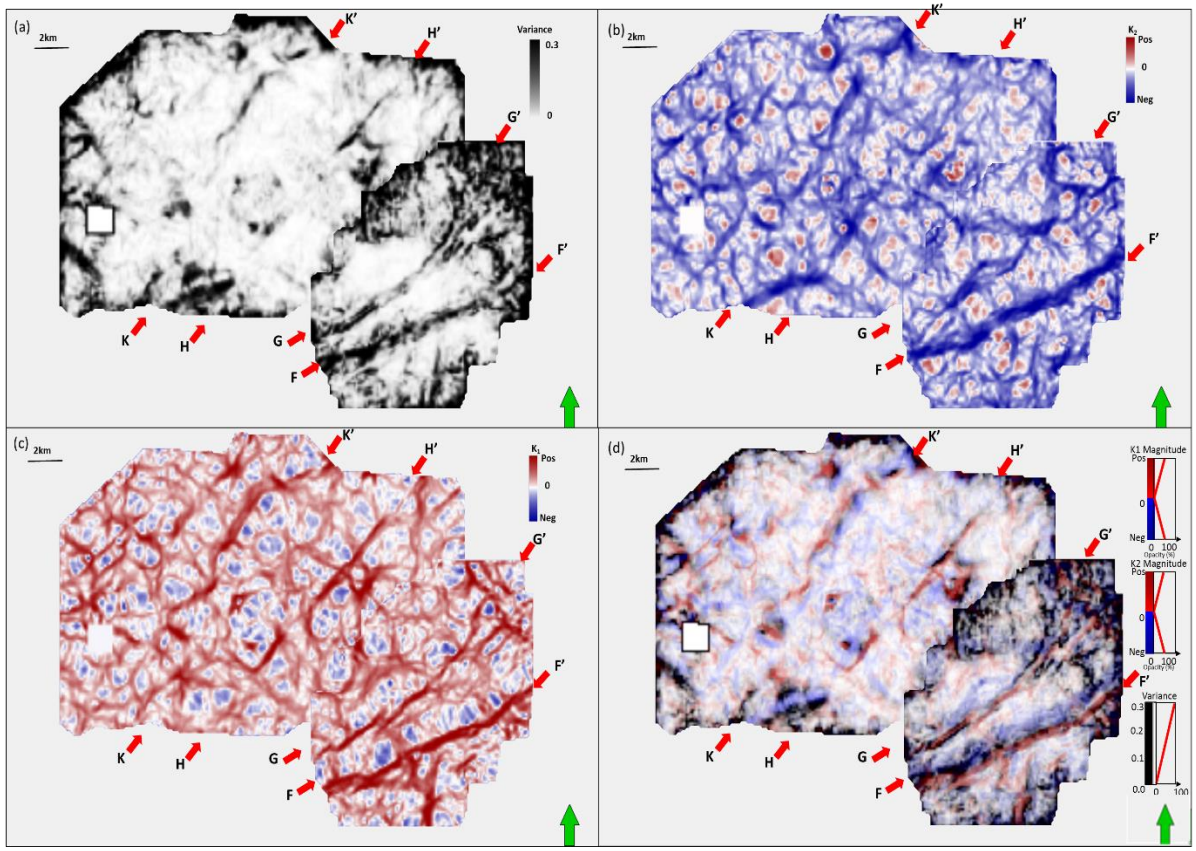

Figure 5.7. Phantom horizon slices 20 ms above the top Viola limestone through (a) variance, (b) most negative curvature k_2, and (c) most positive curvature k_1, and (d) Variance co-rendered with most positive curvature k_1 and most negative curvature k_2. Red arrows donate faults system KK', HH', GG' and FF'.

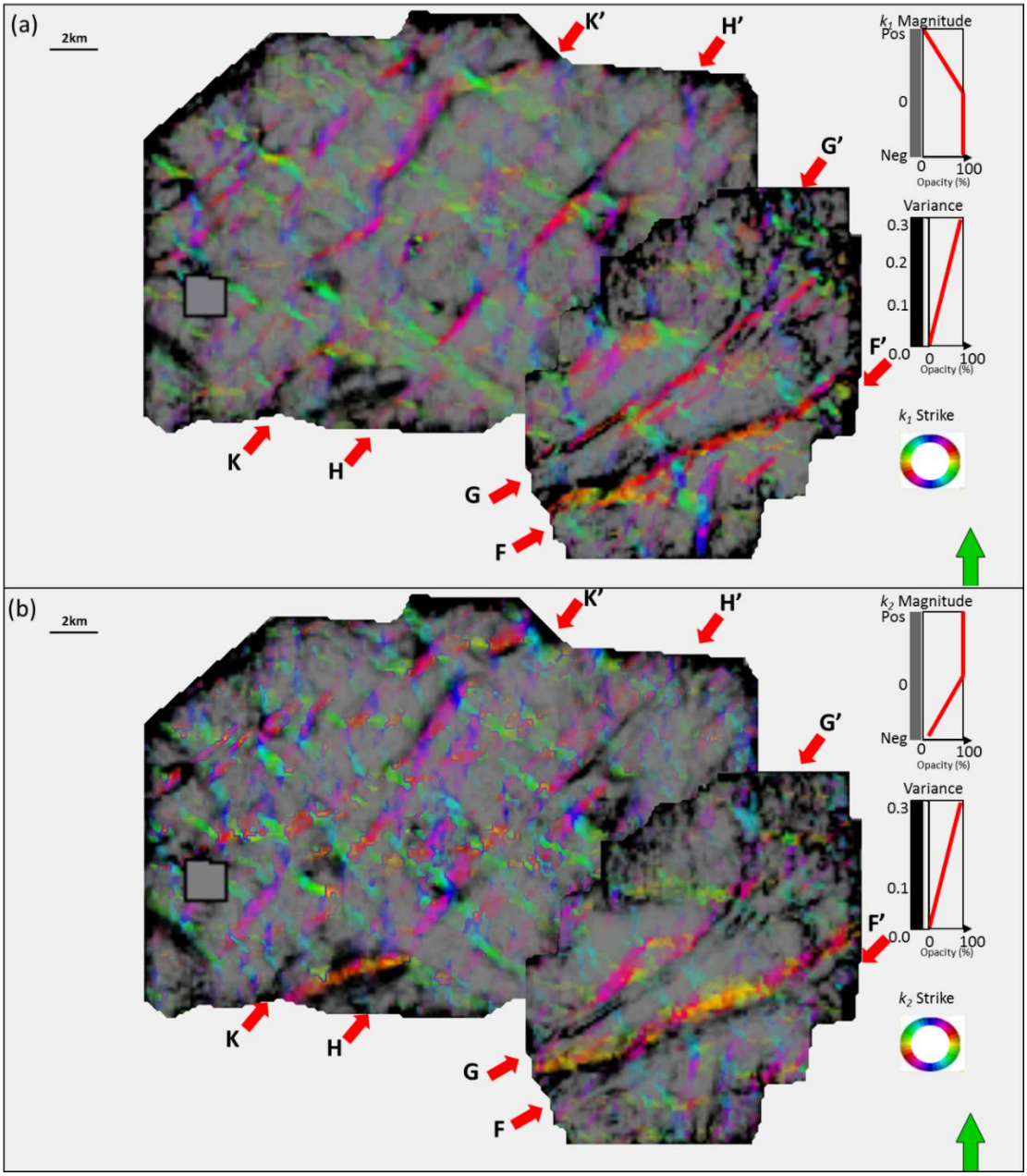

Figure 5.8. Phantom horizon slices 20 ms above the top of theViola limestone through (a) strike of most positive curvature k_1 modulated by its value co-rendered with variance, (b) strike of most negative curvature k_2 modulated by its value co-rendered with variance. Red arrows denote faults.

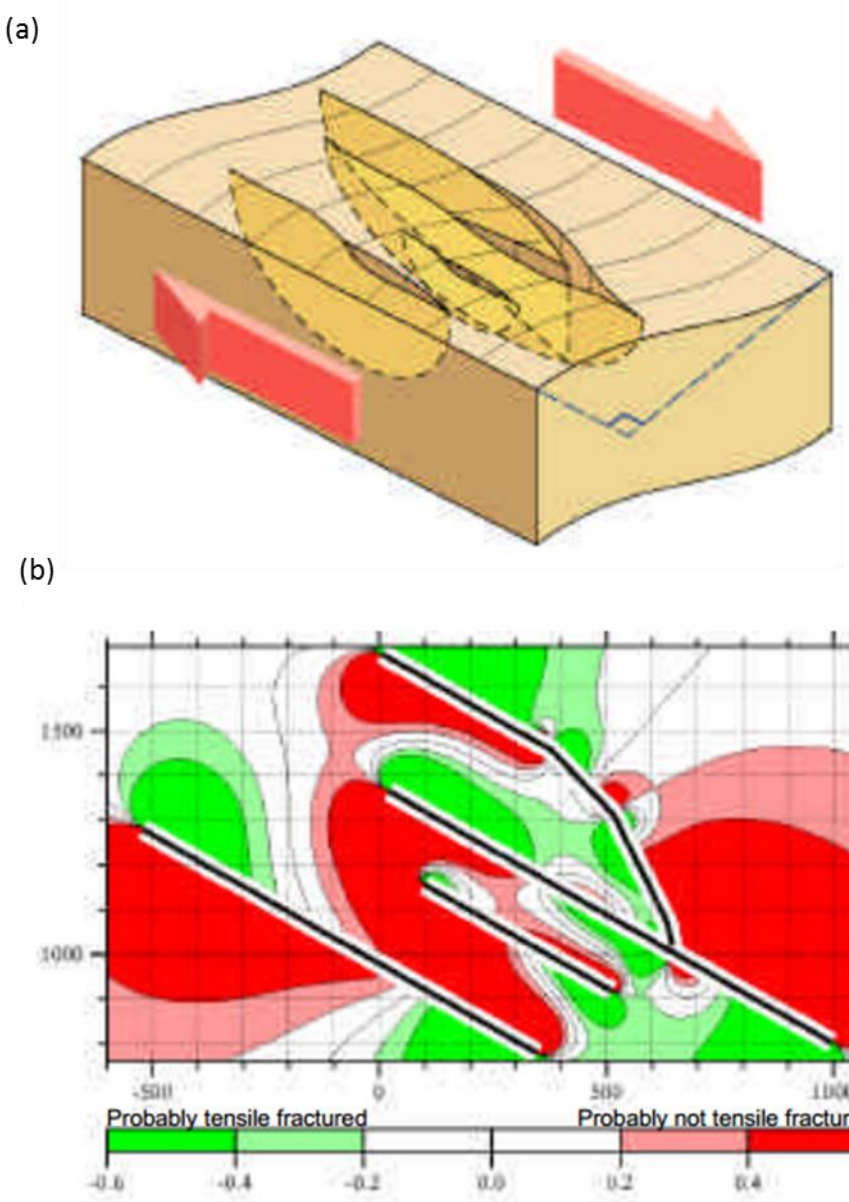

Figure 5.9. Example of an elastic stress field calculated for a three dimensional network of right-lateral strike-slip faults. (a)The faults are triangulated and represented as surfaces of mechanical weakness. These are embedded in a linear elastic, isotropic, homogeneous rock body which is subject to a remote stress. (b)The resulting stress field is expected to govern the distribution of fault-related, small-scale tensile and shear fractures. Numerical solutions for the three-dimensional stress field were obtained using a boundary element method. (After Bourne et al., 2000).

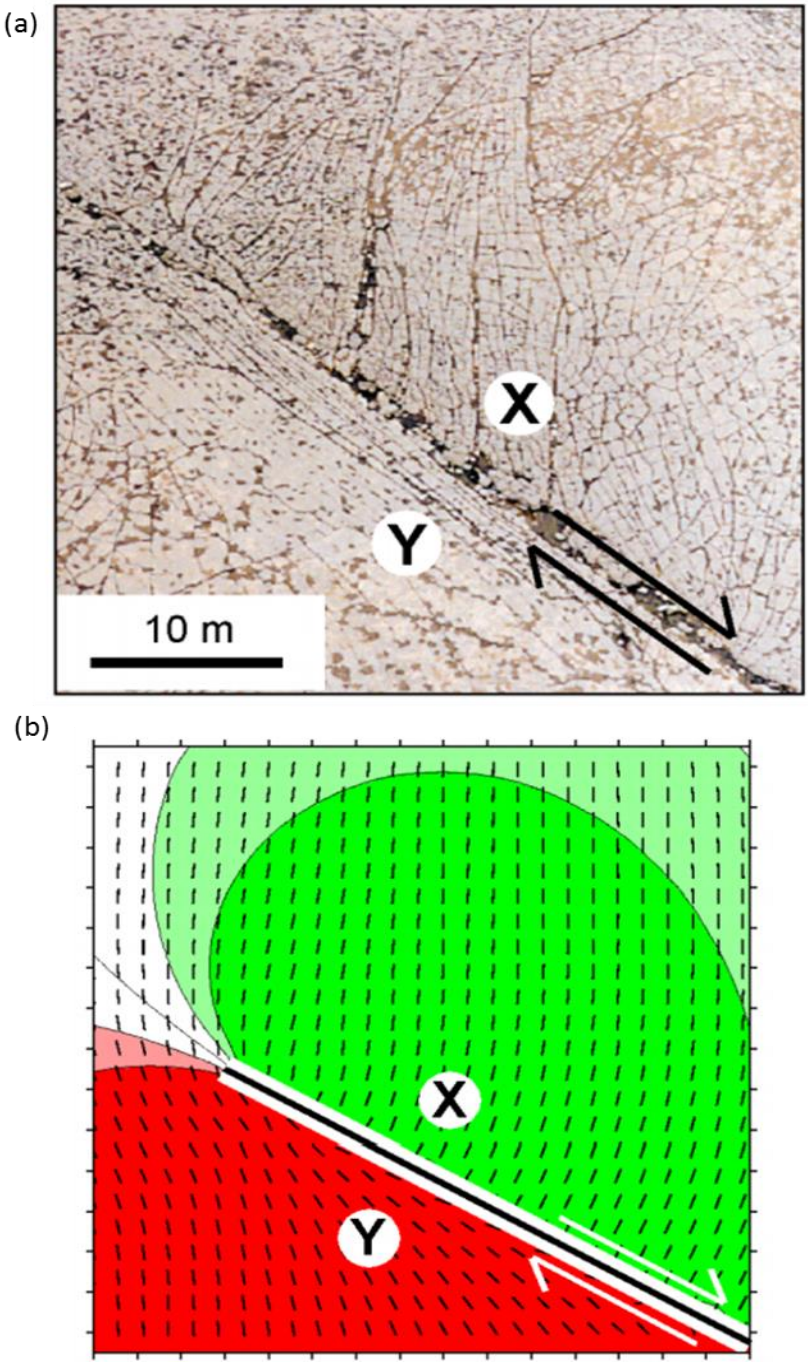

Figure 5.10. (a) Distribution of tensile fractures around the tip of a strike-slip fault at Nash Point, Wales. (b) Sketch of the stress distribution based on (a). Tensile fractures propagate in the direction of greatest compressive stress. At point X, fractures propagate at high angles to the fault plane as rocks on that side of the fault have been stretched parallel to the fault by displacements away from the fault tip. Conversely, at point Y, rocks were displaced toward the fault tip increasing compression parallel to the fault and causing tensile fractures to propagate parallel to the fault. (After Bourne et al., 2000).

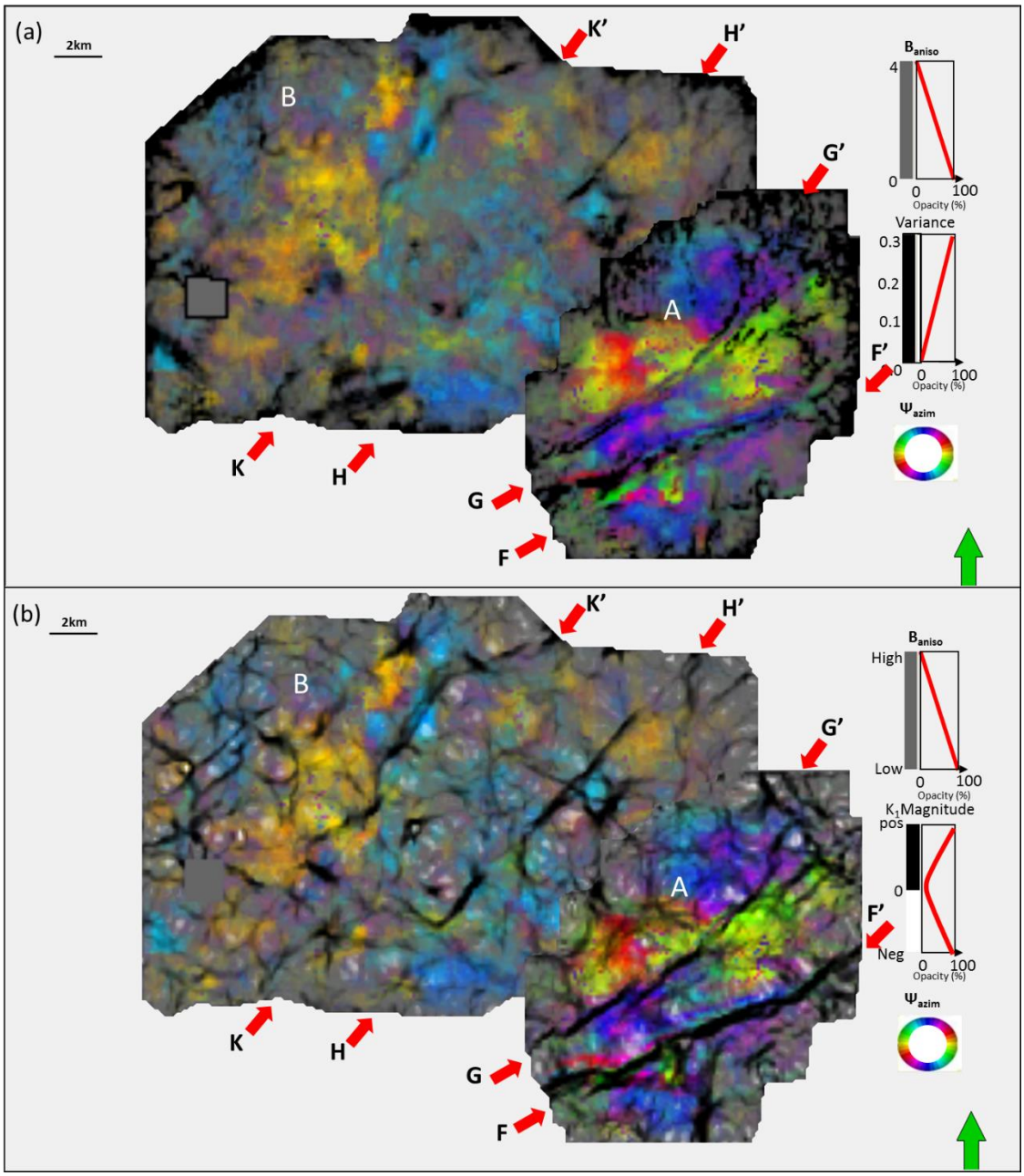

Figure 5.11. Phantom horizon slices 20 ms above the top Viola limestone through anisotropy strike Ψ_{azim} modulated by its value B_{aniso} co-rendered by (a) variance, (b) most positive curvature. Red arrows denote faults.

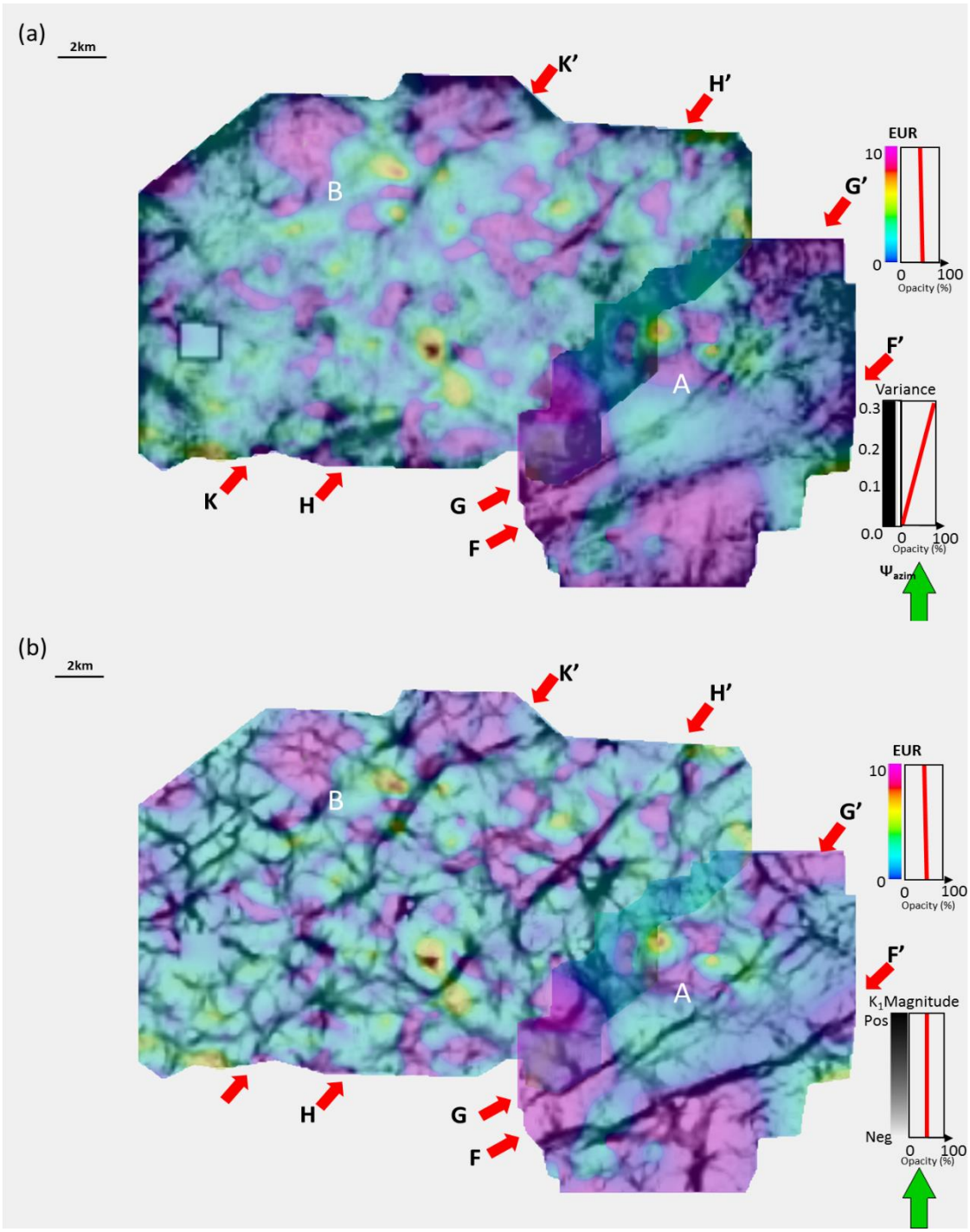

Figure 5.12. Horizon slices 20ms above along Viola limestone through normalized EUR co-rendered with (a) variance, (b) most positive curvature k_1. Red arrows denote faults system.

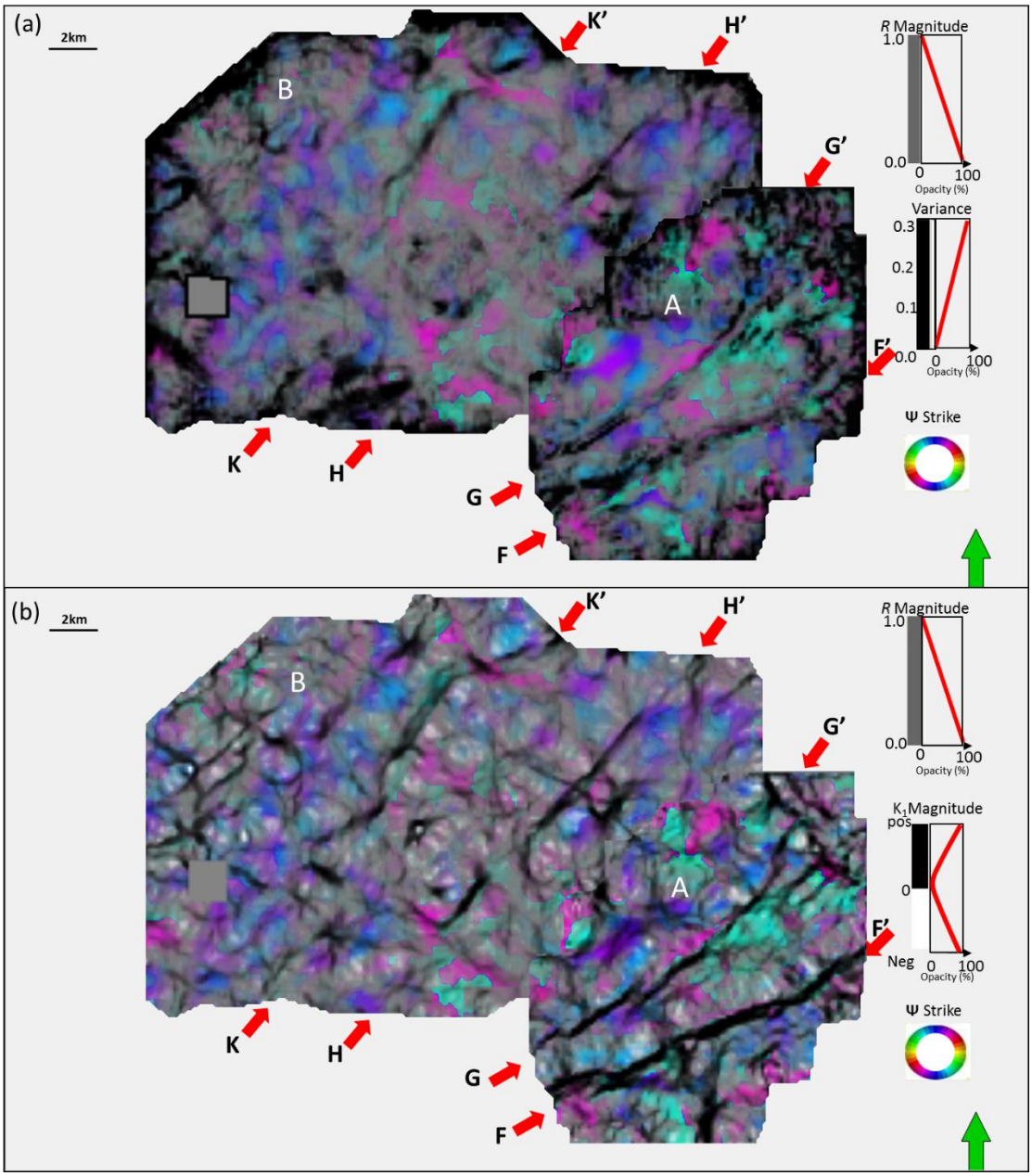

Figure 5.13. Phantom horizon slices 20 ms above the top o the Viola Limestone through strike of new vector correlation (AVAz and k_2) modulated by its value co-rendered by (a) variance and (b) most positive curvature. Red arrows denote faults.

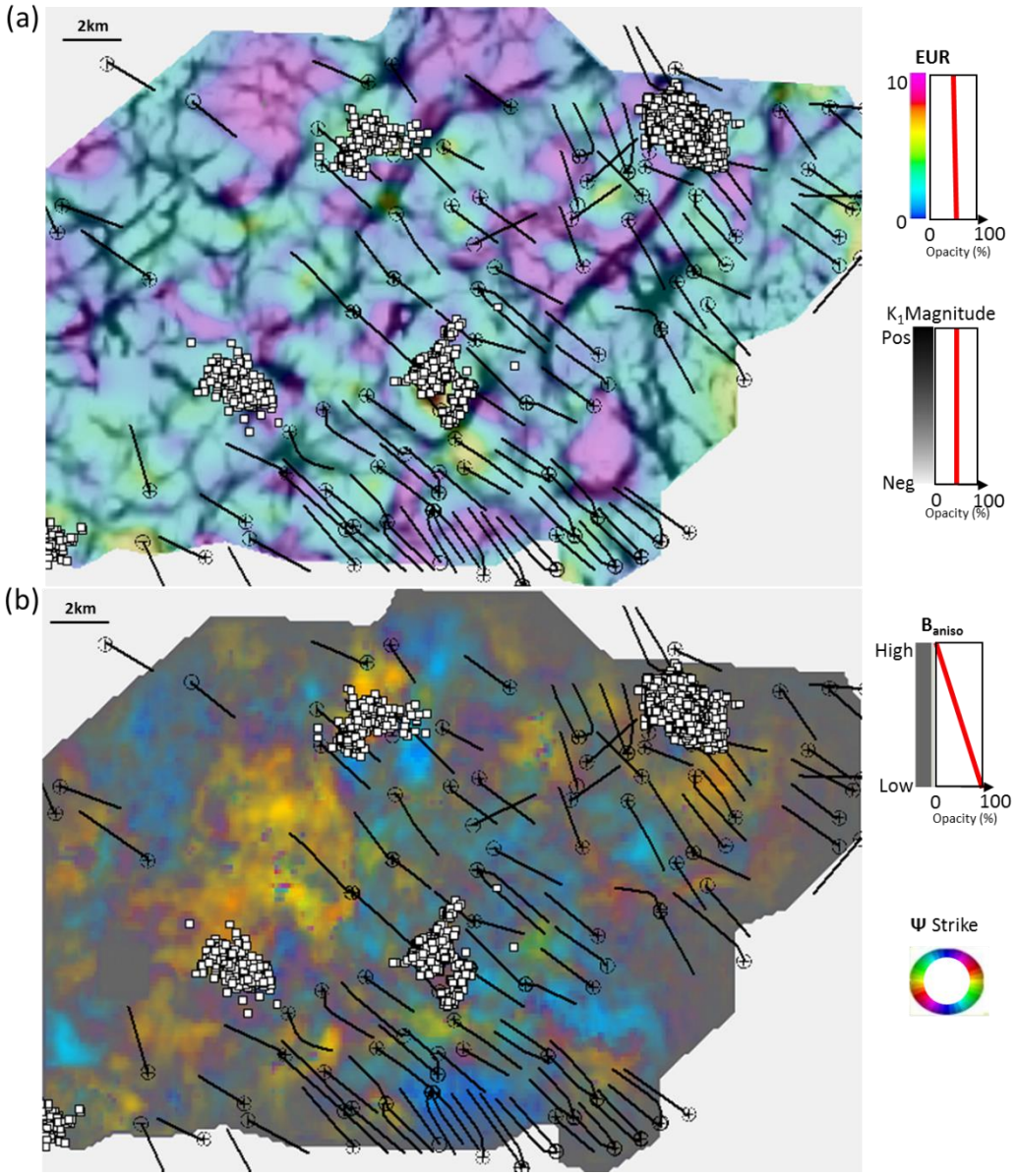

Figure 5.14. Micro-seismic events indicated by white circles, horizontal well paths and relative production indicated by red cycles displayed on phantom horizon slices 20 ms above the top of the Viola limestone through (a) EUR co-rendered with most positive curvature k_1 (b) anisotropy strike Ψ_{azim} modulated by its value B_{aniso} .

REFERENCES

Akepe, S., 2007, Depth imaging of basement control of shallow deformation; Application to Fort Worth Basin and Teapot Dome data sets: M.Sc. Thesis, University of Houston.

Bourne, S., F. Braukmann, L. Rijkels, B. Stephenson, A. Webber, and J. M. Emanuel, 2000, Predictive modeling of natural fractured reservoirs using geomechanics and flow simulation: Presented at 9th Abu Dhabi International Petroleum Exhibition and Conference, ADIPEC 0911.

Chopra, S., and K. J. Marfurt, 2007, Seismic attributes for prospect identification and reservoir characterization: Society of Exploration Geophysicists, Tulsa, OK, 456.

Feazel, C. T., Mylroie, J. E., Palmer, A. N., and Palmer, M. V., Karst from recent to reservoirs: Karst Waters Institute, Special Publication, **14**, 130 -135.

Guo, H., K.J. Marufurt, S. E. Nissen, and E. C. Sullivan, 2010, Visualization and characterization of structural deformation fabric and velocity anisotropy: The Leading Edge, **29**, 654-660.

Guo, Y., 2010, Seismic attribute illumination of the Woodford Shale, Arkoma Basin. Oklahoma: M.Sc. Thesis, University of Oklahoma.

Goodway W., J. Varsek, and C. Abaco, 2006, Practical applications of P-wave AVO for unconventional gas Resource Plays-1 Seismic petrophysics and isotropic AVO: CSEG Recorder Special Edition 2006.

Jarvie, D. M., 2003, Evaluation of unconventional natural gas prospects: The Barnett Shale fractured shale gas model: 21st International Meeting on Organic Geochemistry.

Jenner, E., 2001, Azimuthal anisotropy of 3-D compressional wave seismic data, Weyburn field, Saskatchewan, Canada: Ph.D. dissertation, Colorado School of Mines.

Loucks, R. G., 2008, Origin and modification of Lower Ordovician Ellenburger Group paleokarst breccias and fractures in Central and West Texas, in Sasowsky, I. D., Feazel, C. T., Mylroie, J. E., Palmer, A. N., and Palmer, M. V., Karst from recent to reservoirs: Karst Waters Institute, Special Publication, **14**, 130 -135.

Perez, G., and K. J. Marfurt, 2008, New azimuthal binning for improved delineation of faults and fractures: Geophysics, **73**, S7–S15.

Perez, R., 2013, Brittleness estimation from seismic measurements in unconventional reservoirs: Application to the Barnett Shale: ph.D. dissertation, University of Oklahoma.

Pollastro, R., D. M. Jarvie, R. J. Hill, and C. W. Adams, 2007, Geologic framework of the Mississippian Barnett Shale, Barnett-Paleozoic total petroleum system, Bend arch Fort Worth Basin, Texas: AAPG Bulletin, **91**, 405 - 436.

Rueger, A., 1998, Variation of P-wave reflectivity with offset and azimuth in anisotropic media: Geophysics, **63**, 935-947.

Sicking, C., S. Nelan and W. Mclain, 2007, 3D azimuthal imaging: 77th Annual International Meeting, SEG Expanded Abstracts, 2364-2367.

Thompson, A., J. Rich, and M. Ammerman, 2010, Fracture characterization through the use of azimuthally sectored attribute volumes: 80th Annual International Meeting, SEG, Expanded Abstracts, 1433-1436.

Trumbo, A., and J.P. Rich, 2013, Azimuthal variations in attributes for induced fracture

detection in the Barnett Shale: Interpretation, **1**, no. 2, SB51-SB5.

Zhang, K., B. Zhang, J. T. Kwiatkowski, and K. Marfurt, 2010, Seismic azimuthal impedance anisotropy in the Barnett Shale: 80th Annual International Meeting of the SEG, Expanded Abstracts, 273-277.

Zhang, K., Y. Guo, B. Zhang, A. M. Trumbo, and K. J. Marfurt, 2013, 2014, Seismic azimuthal anisotropy analysis after hydraulic fracturing: Interpretation, **1**, no. 2. SB27-SB36.

Walper, J. L., 1982, Plate tectonic evolution of the Forth Worth Basin, Dallas Geological Society.

Chapter 6: Conclusions

PLSM worked effectively for removing aliasing artifacts arise from decimated Dickman survey from west Kansas. By comparing with the residual convergence rate of LSM, the structure-oriented median filter served as constraint in PLSM.

Application of PLSM to the undecimated Dickman dataset from west Kansas showed rapid improvement of signal-to-noise ratio for CRP gathers and significant attenuation of footprint and random noise, which impeded interpretation from conventional migration. Moreover, PLSM brought significant improvement for seismic attributes illumination. PLSM made multiple attributes better illuminate karst collapse features on Gilmore City horizon. In addition, PLSM worked well for eliminating the random noise in prestack gathers, and the outcome of constrained least-squares migration better represents the seismic amplitudes of earth reflectivity. At last, PLSM allowed better prediction of the original gathers while enhance coherent events.

5D interpolation through PLSM has been proved to be an effective tool for recovering the seismic reflection due to low fold coverage, balance the seismic amplitude, and suppress the footprint noise, while retain lateral resolution associated with diffractions caused by faults.

The successful application of 5D interpolation through PSLM on Dickman survey shows that 5D interpolation can help to balance the fold coverage, interpolate reflections and improve amplitude balancing. In addition, it increases the lateral resolution for karst features imaging and seismic attribute illumination.

The legacy survey is suffered by groundroll noise, the first attempt of merely 5D interpolation through demigration didn't improve seismic image quality and attribute interpretation. Afterward, the application of 5D interpolation through PLSM to groundroll noise suppression gathers allow us to eliminate the footprint noise, increase signal to noise ratio and further better seismic attribute illumination.

The azimuthal anisotropy can be used as a powerful tool to map azimuth and density of fractures in Barnett Shale, different imaging of structural faults lineaments show different focusing for different azimuth directions which caused by anisotropy. High correlation between AVAz anisotropy high and most negative curvature highlight structural faults lineaments. AVAz anisotropy azimuth shows EW and SE orientation of maximum stress field.

In addition, perpendicular relationship between the most negative curvature and AVAz vector is found. We demonstrate that high gas production from mainly Barnett Shale is correlated to high fracture density related to anisotropy high. We can conclude that natural fractures associated with faults is characterized by anisotropy high, which can provide us reliable insight for the fracturing choice along horizontal well.

Comparing the anisotropy analysis of two adjacent surveys, one with seismic data acquired before hydraulic fracturing and the second after, we see that hydraulically induced fracturing modifies seismic P-wave anisotropy. Even though completion takes place across ridges, the resulting microseismic events avoid these ridges and concentrate in the intervening faults (Trumbo and Rich, 2013). EUR also appears to be compartmentalized by these ridges.

The vector correlation between most positive curvature and AVAz anisotropy for the survey acquired before hydraulic fracturing indicates complicated patterns consistent with strike-slip faulting. This correlation is diminished after hydraulic fracturing.

Though encouraging, this experiment does not prove my hypothesis that hydraulic fracturing decreases seismic anisotropy. To do so, a wide-azimuth time-lapse survey that covers, as accurately as possible, the same subsurface area is required. Equally important, I do not know whether the reduction in anisotropy is due to rubblizing of the reservoirs (making them more isotropic) or due to the creation of orthogonal fractures (making is more orthotropic). Such understanding may be critical in future restimulation, determining the direction of new wells, and to mapping zones of by-passed pay.

Appendix B: List of Symbols

Symbols	meaning
m	migrated CRP gathers
q	midpoint vector between source and receiver
t	two way travel time
w	migration weight
o	offset vector
d	seismic data vector
Ω	migration aperture
Q	demigration aperture
ξ	The (x,y,z) coordinate information
L	forward modeling operator (prestack Kirchhoff time demigration)
$\mathbf{L}^{\mathrm{T}}$	adjoint operator (prestack Kirchhoff time migration)
ε	misfit function
r	residual vector
g	gradient vector
h	conjugate direction vector
α	weighting coefficient
β	weighting coefficient
$\boldsymbol{u}$	a specific trace within the migration analysis window
$\mathbf{XY}_{\xi}$	the horizontal projection of the image-coordinates vector

$\mathbf{B_{aniso}}$	Anisotropy intensity
$\boldsymbol{\psi_{aniso}}$	Anisotropy strike
K_2	most negative curvature
$\boldsymbol{\phi_2}$	Strike of most negative curvature
r_{colinear}	Correlation coefficient

Appendix C: AVAz and VVAz

Shale with vertical fractures can be viewed as horizontal transverse isotropy (HTI) medium. As the elastic properties of HTI medium are different at different azimuths, the PP reflection coefficients varies from different incident angle on a boundary of an HTI medium. Rüger (1998, 2002) derived an approximate equation of PP reflection coefficient at an arbitrary azimuth for an HTI medium over another HTI medium with the axis of symmetry in the same direction (the direction normal to the fracture strike).

When the incident angle is smaller than 30^0, Rueger's (1996) equation for AVAz can be written as

$$R(\theta,\varphi) = A + (B^{iso} + B^{ani}cos^2(\varphi - \varphi_0))sin^2\theta \qquad (1)$$

where $R(\theta,\varphi)$ is the reflectivity at angle of incidence θ and azimuth φ

$$B^{iso} = \frac{1}{2}\frac{\Delta V_p}{V_p} - 2\left(\frac{V_s}{V_p}\right)^2\left(\frac{\Delta\rho}{\rho}\right) - 4\left(\frac{V_s}{V_p}\right)\frac{V_s}{V_s}^2 \qquad (2)$$

$$B^{ani} = \frac{1}{2}[\Delta\partial^{(v)} + 2\left(\frac{2V_s}{V_p}\right)\Delta\gamma^{(v)}] \qquad (3)$$

In the absence of anisotropy, $B_{aniso}=0$, and equation (1) reverts to the well-known AVO equations in terms of slope, B_{iso}, and AVO intercept A. Note the azimuthal anisotropy plays an increasingly stronger role larger angles of incidence, as indicated by the $\sin^2\theta$ coefficient.

VVAz

Formation with vertical fractures can be treated HTI medium, P wave travelling velocity varies at different azimuth angles to the fractures, horizontal P wave velocity is higher for seismic waves traveling parallel to the fractures than traveling perpendicular to the fractures. It is assumed that the direction of the fast NMO velocity is parallel to the direction of the fracture strike. The difference of the fast and slow NMO velocities can be an indicator of the fracture density.

The velocity of seismic waves is function of the elastic moduli and bulk density of the medium. The seismic phase velocities for different modes of waves for weak anisotropy can be expressed as (Thomsen, 1986)

$$V_p(\theta) = V_{p0}(1 + \delta sin^2\theta cos^2\theta + \varepsilon sin^4\theta)$$

Where V_{p0} is p wave velocity along the vertical axis, δ and ε are Thomsen's parameters, and θ is the angle between vertical axis and the normal to the wavefront.

Tsvankin (1997) derived the P wave NMO velocity at an arbitrary azimuth for an HTI medium:

$$V_{nmo}^2 = V_0^2(1 + 2\delta^{(v)}cos^2(\varphi - \varphi_0))$$

Where V_{nmo} is the P wave NMO velocity for small offsets, V_0 is the P wave velocity when seismic wave traveling vertically downward, φ_0 is the azimuth direction normal to the fractures, φ is the azimuth direction of the seismic ray path. $\delta^{(v)}$is a Thomsen's parameter for HTI media.

References

Rueger, A., and I. Tsvankin, 1995, Azimuthal variation of AVO response for fractured reservoirs: 65th Ann. International Meeting, SEG, Expanded Abstracts, 1103-1106.

Rueger, A., 1997, P-wave reflection coefficients for transversely isotropic models with vertical and horizontal axis of symmetry: Geophysics, **62**, 713-722.

Rueger, A., 1998, Variation of P-wave reflectivity with offset and azimuth in anisotropic media: Geophysics, **63**, 935-947.

Thomsen, L.A., 1988, Reflection seismology over azimuthally anisotropic media: Geophysics, **53**, 304 – 313.

Thompson, A., J. Rich, and M. Ammerman, 2010, Fracture characterization through the use of azimuthally sectored attribute volumes: 80th Annual International Meeting, SEG, Expanded Abstracts, 1433-1436.

Tsvankin, I., 1997, Reflection moveout and parameter estimation for horizontal transverse isotropy: Geophysics, **62,** 614-629.